ISTANBUL TECHNICAL UNIVERSITY ★ GRADUATE SCHOOL OF SCIENCE ENGINEERING AND TECHNOLOGY

DEPOSITION OF NANOCRYSTALLIZED AMORPHOUS SILICON THIN FILMS BY MAGNETRON SPUTTERING

M.Sc. THESIS

Elif Ceylan CENGİZ

Department of Nanoscience and Nanoengineering

Nanoscience and Nanoengineering Programme

AUGUST 2013

ISTANBUL TECHNICAL UNIVERSITY ★ GRADUATE SCHOOL OF SCIENCE
ENGINEERING AND TECHNOLOGY

DEPOSITION OF NANOCRYSTALLIZED AMORPHOUS SILICON THIN FILMS BY MAGNETRON SPUTTERING

M.Sc. THESIS

Elif Ceylan CENGİZ

513101028

Department of Nanoscience and Nanoengineering

Nanoscience and Nanoengineering Programme

Thesis Advisor: Prof. Dr. Eyüp Sabri KAYALI
Thesis Co-advisor: Assoc. Prof. Dr. Osman ÖZTÜRK

AUGUST 2013

İSTANBUL TEKNİK ÜNİVERSİTESİ ★ FEN BİLİMLERİ ENSTİTÜSÜ

NANOKRİSTALİZE EDİLMİŞ AMORF SİLİSYUM İNCE FİLMLERİN MAGNETRON SAÇTIRMA YÖNTEMİ İLE BÜYÜTÜLMESİ

YÜKSEK LİSANS TEZİ

Elif Ceylan CENGİZ

513101028

Nanobilim ve Nanomühendislik Anabilim Dalı

Nanobilim ve Nanomühendislik Programı

Danışmanı: Prof. Dr. Eyüp Sabri KAYALI
Eş-Danışmanı: Doç. Dr. Osman ÖZTÜRK

AĞUSTOS 2013

Elif Ceylan Cengiz, a M.Sc. student of ITU Institute of Science student ID 513101028 successfully defended the thesis entitled “Deposition of Nanocrystallized Amorphous Silicon Thin Films by Magnetron Sputtering”, which she prepared after fulfilling the requirements specified in the associated legislations, before the jury whose signatures are below.

Thesis Advisor : **Prof. Dr. Eyüp Sabri KAYALI** ....
Istanbul Technical University

Co-advisor : **Assoc. Prof. Dr. Osman ÖZTÜRK** ....
Gebze Institute of Technology

Jury Members : **Assoc. Prof. Dr. Hüseyin KIZIL** ....
Istanbul Technical University

Assoc. Prof. Dr. Özkan GÜLSOY ....
Marmara University

Assoc. Prof. Dr. Mehmet TARAKÇI ....
Gebze Institute of Technology

Date of Submission : 02 September 2013
Date of Defense : 16 August 2013

FOREWORD

Firstly, I would like to express my deepest appreciation for the technical guidance and support given by my advisor Prof. Dr. Eyüp Sabri Kayalı. His advices will always be a guide for me.

I would like to say special thanks my co-advisor Assoc. Prof. Dr. Osman Öztürk. His thorough understanding of the many issues, his attention to detail and the technical guidance will always be remembered. By the help of his close interest in me and sharing his valuable experience with me, this work became possible.

I would like to say special thanks to my dear friend and workmate Specialist Melek Türksoy Öcal, because she always helps me at this work tirelessly and tries to make me smile and strong.

Thanks go to my other workmates Baha Sakar, Research Assistant Ali Şems Ahsen and Büşra Ünsel for their help in experimental procedure. I would like to say thank Assist. Prof. Dr. Mustafa Erkovan.

I would like to say thank Assoc. Prof. Dr. Mehmet Tarakçı who always shares his knowledge and experience with me during experimental procedure.

Thanks go to also Specialist Adem Şen, Technician Emrah Anigi and Specialist Ahmet Nazım for characterization procedure to my samples.

I would like to say a special thank Dr. Meltem Sezen for her help in characterization section.

I would like to say thanks Assist. Prof. Dr. Sibel Tokdemir Öztürk for her help during writing of thesis.

I would like to express my deepest feelings to my valuable parents, my brother and his family for supporting me all the time. I would like to say thank them.

And I would like to say final thank my dear husband Sezgin Cengiz for supporting me all the time and his endless patience.

August 2013 **Elif Ceylan Cengiz**

TABLE OF CONTENTS

Page

FOREWORD .... **vii**
TABLE OF CONTENTS .... **ix**
ABBREVIATIONS .... **xi**
LIST OF TABLES .... **xiii**
LIST OF FIGURES .... **xv**
LIST OF SYMBOLS .... **xxi**
SUMMARY .... **xxiii**
ÖZET .... **xxv**
1. INTRODUCTION **1**
2. ELECTRONIC STRUCTURE OF MATERIALS **5**
  2.1. Band Structure of Solids **5**
  2.2. Semiconductors **7**
  2.3. Doping of Semiconductors **7**
    2.3.1. N-Type **7**
    2.3.2. P-Type **8**
  2.4. P-N Junctions **8**
3. SOLAR CELLS **11**
  3.1. Solar Energy **11**
  3.2. Solar Cells **12**
    3.2.1. Working Principle of Solar Cells **12**
    3.2.2. Light Absorption **13**
    3.2.3. Types of Solar Cells **14**
      3.2.3.1. First Generation **14**
      3.2.3.2. Second Generation **15**
      3.2.3.3. Third Generation **16**
  3.3. Silicon Thin Film Solar Cells **16**
    3.3.1 Amorphous Silicon **16**
      3.3.1.1. Staebler-Wronski Effect **19**
    3.3.2. Nanocrystalline Silicon **20**
4. MAGNETRON SPUTTERING **23**
5. X-RAY PHOTOELECTRON SPECTROSCOPY **25**
6. EXPERIMENTAL STUDY **27**
  6.1 Thin Film Deposition by Magnetron Sputtering **28**
    6.1.1. Deposition of Amorphous Silicon by DC Power Supply **28**
      6.1.1.1. Deposition of Substrate with Titanium **29**
      6.1.1.2. Deposition of Amorphous Silicon **29**

6.1.2. Deposition of Amorphous Silicon by RF Power Supply.......... **32**
6.1.2.1. Depositions by Powder Target.......... **32**
6.1.2.2. Depositions by Substrate Target.......... **33**
6.1.3. Formation of Nanocrystalline Silicon.......... **33**
6.2. Characterization of Thin Films.......... **34**
6.2.1. X-Ray Photoelectron Spectrscopy (XPS) Analysis.......... **34**
6.2.2. Raman Spectroscopy Analysis.......... **35**
6.2.3. X-Ray Diffraction (XRD) Analysis.......... **35**
6.2.4. Atomic Force Microscopy (AFM) Analysis.......... **36**
6.2.5. Scanning Electron Microscopy (SEM) Analysis.......... **36**
7. RESULTS 37
7.1. X-Ray Photoelectron Spectroscopy.......... **37**
7.2. Raman Spectroscopy.......... **44**
7.3. Atomic Force Microscopy.......... **47**
7.4. X-Ray Diffraction.......... **61**
7.5. Scanning Electron Microscopy.......... **74**
8. DISCUSSION.......... 77
9. CONCLUSIONS.......... 79
REFERENCES.......... 81
CURRICULUM VITAE.......... 85

ABBREVIATIONS

AFM : Atomic Force Microscopy

ASF : Atomic Sensitivity Factor

a-Si:H : Hydrogenated Amorphous Silicon

DC : Direct Current

HWCVD : Hot Wire Chemical Vapor Deposition

nc-Si:H : Hydrogenated Nanocrystallized Silicon

PDC : Pulsed Direct Current

PECVD : Plasma Enhanced Chemical Vapor Deposition

PVD : Physical Vapor Deposition

QCM : Quasi Crystal Microbalance

RF : Radiofrequency

RMS : Reactive Magnetron Sputtering
SEM : Scanning Electron Microscopy

XPS : X-Ray Photoelectron Spectroscopy

XRD : X-Ray Diffraction

UPS : Ultraviolet Photoelectron Spectroscopy

LIST OF TABLES

Page No

Table 6.1 : Deposition conditions of films which were prepared with different power values.. 29

Table 6.2 : Calculated deposition rates for all samples......................... 30

Table 6.3 : Total time required for deposition...................................... 30

Table 6.4 : The lowest and the highest power and argon flow rates....... 31

Table 6.5 : Calculated deposition rates and deposition time for the lowest and the highest power and argon flow rate............... 31

Table 6.6 : Deposition on glass... 31

Table 6.7 : Parameters of deposition of titanium................................. 32

Table 6.8 : Parameters of deposition of samples with powder target..... 32

Table 6.9 : Parameters of deposition of samples with substrate target... 33

Table 6.10 : Deposition parameters of annealed substrates..................... 34

Table 7.1 : Chemical proportion of native oxidized single crystalline silicon substrate.. 38

Table 7.2 : The chemical proportion of silicon thin films..................... 40

Table 7.3 : Argon content in silicon thin films.................................... 41

Table 7.4 : Argon and oxygen content of silicon thin films.................. 42

Table 7.5 : The oxygen content in silicon thin films............................ 43

LIST OF FIGURES

Page No

Figure 2.1 : Allowed and forbidden energy regions for electrons in a solid... 6

Figure 2.2 : T= 0 ^{o}K, conduction and valence band conditions, (a) metal, (b) semiconductor, (c) insulator................................ 6

Figure 2.3 : For a p–n rectifying junction, representations of electron and hole distributions for (a) no electrical potential, (b) forward bias and (c) reverse bias.. 9

Figure 2.4 : Electromagnetic Spectrum.. 10

Figure 3.1 : Approximately the E-k diagram at the bottom of the conductance band and at the top of the valence band of Si and GaAs by parabolas... 13

Figure 3.2 : a) Crystalline Si, b) Amorphous Silicon, c) Hydrogenated Amorphous Silicon atomic arrangement and band structure.. 16

Figure 3.3 : Schematic drawing of the atomic structure and microstructure of hydrogenated amorphous silicon............. 17

Figure 3.4 : Schematic densities of states for (a) crystalline silicon and (b) hydrogenated amorphous silicon.................................... 18

Figure 3.5 : The absorption as a function of wavelength of thin film nanocrystalline silicon compared to that of a-Si:H. The band gaps, Eg, of the two materials are shown.................... 19

Figure 3.6 : Structure of nanocrystalline silicon thin film showing the crystallites and voids embedded in amorphous matrix.......... 20

Figure 4.1 : Circular magnetic field... 22

Figure 6.1 : Magnetron sputtering and XPS integrated system............... 25

Figure 6.2 : The main components of XPS.. 34

Figure 6.3 : The appearance of sample in XPS analysis chamber........... 35

Figure 7.1 : XPS spectrum of native oxidized (111) oriented single crystalline silicon substrate.. 37

Figure 7.2 : XPS spectrum of titanium deposited silicon substrate.......... 38

Figure 7.3 : XPS spectrum of samples deposited at 1 W, 4 W, 10 W and 15 W.. 39

Figure 7.4 : XPS spectrum of silicon deposited sample at 1 Watt & 15 Watt and with lowest and highest argon flow rates.............. 40

Figure 7.5 : XPS spectrum of silicon deposited sample at 10 Watt, 15 Watt, 150 Watt and 2.7 argon flow rate............................... 41

Figure 7.6 : XPS spectrum of silicon deposited sample at 10 Watt, 15 Watt, 150 Watt and 2.7 sccm argon flow rate...................... 42

Figure 7.7 : XPS spectrum of annealed samples deposited by powder and substrate target... 43

Figure 7.8 : The Raman spectra of native oxidized silicon substrate....... 44

Figure 7.9 : The Raman spectra of the sample deposited by substrate target at 15 Watt and 2.7 sccm argon flow rate.................... 45

Figure 7.10 : The Raman spectra of quartz substrate................................. 45

Figure 7.11 : The Raman spectra of the annealed samples deposited by a) powder target b) substrate target at 15 Watt and 2.7 sccm argon flow rate.. 46

Figure 7.12 : The 10µmx10µm AFM images of samples a) native oxidized single crystalline silicon, b) titanium deposited silicon... 47

Figure 7.13 : The 10µmx10µm lateral AFM image of native oxidized single crystalline silicon substrate....................................... 48

Figure 7.14 : The 10µmx10µm lateral AFM image of titanium deposited silicon substrate.. 48

Figure 7.15 : The 10µmx10µm AFM images of the samples a) 1 Watt, b) 4 Watt, c) 10 Watt and d)15 Watt... 49

Figure 7.16 : The 10µmx10µm AFM images of the samples a) 1 Watt and 2 sccm, b) 1 Watt and 20 sccm...................................... 50

Figure 7.17 : The 10µmx10µm lateral AFM images of the sample deposited at 1 Watt and 2 sccm argon flow rate................... 51

Figure 7.18 : The 10µmx10µm lateral AFM images of the sample deposited at 1 Watt and 20 sccm argon flow rate................. 52

Figure 7.19 : The 2µmx2µm AFM images of the samples a) 15 Watt and 0.8 sccm, b) 15 Watt and 20 sccm argon flow rate.............. 52

Figure 7.20 : The 10µmx10µm lateral AFM image of sample deposited at 15 Watt and 0.8 sccm argon flow rate.............................. 53

Figure 7.21 : The 10µmx10µm lateral AFM image of sample deposited at 15 Watt and 20 sccm argon flow rate............................... 53

Figure 7.22 : The 10µmx10µm AFM images of samples a) 10 Watt and 2.7 sccm, b) 15 Watt and 2.7 sccm, c) 150 Watt and 2.7 sccm.. 54

Figure 7.23 : The 2µmx2µm lateral AFM image of sample deposited at 10 Watt and 2.7 sccm argon flow rate................................. 55

Figure 7.24 : The 2µmx2µm lateral AFM image of sample deposited at 15 Watt and 2.7 sccm argon flow rate................................. 56

Figure 7.25 : The 2µmx2µm lateral AFM image of sample deposited at 150 Watt and 2.7 sccm argon flow rate............................... 56

Figure 7.26 : The 5µmx5µm AFM image of sample deposited at a) 10 Watt and 2.7 argon flow rate b) 15 Watt and 2.7 sccm argon flow rate (c) 150 Watt and 2.7 sccm argon flow rate.. 57

Figure 7.27 : The 5µmx5µm lateral AFM image of sample deposited at 10 Watt and 2.7 sccm argon flow rate................................. 58

Figure 7.28 : The 5µmx5µm lateral AFM image of sample deposited at 15 Watt and 2.7 sccm argon flow rate................................. 58

Figure 7.29 : The 5µmx5µm lateral AFM image of sample deposited at 150 Watt and 2.7 sccm argon flow rate............................... 59

Figure 7.30 : The 10µmx10µm AFM image of sample deposited by a) substrate target b) powder target... 59

Figure 7.31 : The 10µmx10µm AFM image of sample deposited by substrate target.. 60

Figure 7.32 : The 10µmx10µm lateral AFM image of sample deposited by powder target.. 61

Figure 7.33 : X-Ray Diffraction pattern of native oxidized silicon substrate.. 62

Figure 7.34 : X-Ray Diffraction pattern of titanium deposited silicon substrate.. 63

Figure 7.35 : The X-Ray diffraction pattern of silicon deposited substrate at 1 W.. 64

Figure 7.36 : The X-Ray Diffraction pattern of silicon deposited substrate at 4 W.. 64

Figure 7.37 : The X-Ray Diffraction pattern of silicon deposited substrate at 10 W... 65

Figure 7.38 : The X-Ray diffraction pattern of silicon deposited substrate at 15 W.. 65

Figure 7.39 : The X-Ray diffraction pattern of silicon deposited glass substrate.. 66

Figure 7.40 : The X-Ray diffraction pattern of silicon deposited sample at 1 Watt and 2 sccm argon flow rate.................................. 67

Figure 7.41 : The X-Ray diffraction pattern of silicon deposited sample at 1 Watt and 20 sccm argon flow rate................................ 67

Figure 7.42 : The X-Ray diffraction pattern of silicon deposited sample at 15 Watt and 0.8 sccm argon flow rate............................. 68

Figure 7.43 : The X-Ray diffraction patterns of silicon deposited sample at 15 Watt and 20 sccm argon flow rate. 69

Figure 7.44 : The X-Ray diffraction patterns of silicon deposited sample at 10 Watt and 2.7 sccm argon flow rate.............................. 70

Figure 7.45 : The X-Ray diffraction pattern of silicon deposited sample at 15 Watt and 2.7 sccm argon flow rate.............................. 70

Figure 7.46 : The X-Ray diffraction pattern of silicon deposited sample at 150 Watt and 2.7 sccm argon flow rate............................ 71

Figure 7.47 : The X-Ray diffraction pattern of silicon deposited sample at 10 Watt and 2.7 sccm argon flow rate.............................. 72

Figure 7.48 : The X-Ray diffraction pattern of silicon deposited sample at 15 Watt and 2.7 sccm argon flow rate.............................. 72

Figure 7.49 : The X-Ray diffraction pattern of silicon deposited sample at 150 Watt and 2.7 argon flow rate.................................... 73

Figure 7.50 : The X-Ray diffraction patterns of sample deposited by powder silicon target and annealed at 800 °C for 1 hour...... 74

Figure 7.51 : The cross sectional SEM image of sample which was deposited by RF power and powder target, 4 Watt-2.7 sccm.. 74

Figure 7.52 : The cross sectional SEM image of sample which was deposited by DC power, 150 Watt - 2.7 sccm....................... 75

LIST OF SYMBOLS

E_g : Energy band gap

eV : Electron Volt

E : Energy

h : Planck’s constant

υ : Frequency

c : Speed of light

λ : Wavelength

f **:** Mass fraction

N : North

S : South

B : Magnetic field

E_k : Kinetic energy

E_b : Binding energy

Φ : Working function

I : Final intensity

I_o : Initial intensity

d : Thickness

Å : Angstrom

ϑ : Angle

DEPOSITION OF NANOCRYSTALLIZED AMORPHOUS SILICON THIN FILMS BY MAGNETRON SPUTTERING

SUMMARY

In this work, nanocrystallized amorphous silicon thin films were synthesized and it was aimed to apply this to solar cell applications which are accepted as one of the most important alternative for renewable energy sources. In accordance with this purpose, by using DC Magnetron Sputtering and RF Magnetron Sputtering, observations were made comparatively. Primarily amorphous silicon thin film was obtained and then by the help of X - Ray Photoelectron Spectroscopy (XPS), Raman Spectroscopy, X - Ray Diffraction (XRD), Atomic Force Microscopy (AFM) and Scanning Electron Microscopy (SEM), thin film samples were investigated. Behind this, annealing was performed on samples at fixed temperature and certain times and nanocrystallized silicon particles were obtained.

At first, by using DC Magnetron Sputtering, samples were deposited on titanium deposited silicon substrates under 1 Watt, 4 Watt, 10 Watt and 15 Watt, at 18 ^{o}C temperature. Thickness was 300 Å for all samples. After that thin film depositions were done for 1 Watt at 2 sccm and 20 sccm and for 15 Watt at 0.8 sccm and 20 sccm argon flow rate. Later on, RF power source started to be used and at that time addition to the powder silicon target, single crystalline silicon substrate was started to be used as target. For each target, thin film depositions were done at 10 Watt, 15 Watt and 150 Watt. After all these, two samples were deposited by RF power and annealed at 800 °C for 1 hour. After all deposition procedure, X - Ray Photoelectros Spectroscopy (XPS) characterization was made without taking samples outside. Behind all of these, samples were characterized by Atomic Force Microscopy (AFM), Raman Spectroscopy, X - Ray Diffraction (XRD) and Scanning Electron Microscopy (SEM). As a result of these, by the investigation of characterization results, it is understood that amorphous silicon was obtained at first and then nanocrystalline silicon particles were acquired by annealing.

NANOKRİSTALİZE EDİLMİŞ AMORF SİLİSYUM İNCE FİLMLERİN MAGNETRON SAÇTIRMA YÖNTEMİ İLE BÜYÜTÜLMESİ

ÖZET

Fosil yakıtların tükeniyor oluşu bilim adamlarını alternatif enerji kaynağı bulma konusunda harekete geçirmiştir. Bu amaç ile birçok alternatif enerji kaynağı geliştirilmiştir. Bunların en önemlilerinden ve en çok kullanılanlarından biri güneş pilleridir. Güneş pillerinin kaynağının yeryüzündeki canlılar için tükenmez bir enerji kaynağı olan güneş oluşu, hareketli bir parçası olmaması sebebiyle bakım gerektirmemesi, uzun ömürlü olması ve çevreye zararlı olmaması sebebiyle kullanımı oldukça avantajlıdır.

Güneş pilleri üzerlerine düşen güneş ışığını doğrudan elektrik enerjisine çeviren aygıtlardır. Yapımında yarıiletken malzemeler kullanılmaktadır. Yapısı en basit haliyle p-i-n eklemi şeklindedir. Güneş pilindeki yarıiletken üzerine güneş ışığı düştüğünde eğer gelen ışığın enerjisi kullanılan yarıiletkenin bant aralığına eşit ya da ondan büyük ise yarıiletkenden elektron koparabilir. Kopan bu elektron ardında bir boşluk bırakır. Elektron ve boşluğun bu şekilde birbirine ters hareketi sayesinde dış devrede bir elektrik akımı oluşur. Böylece elektrik enerjisi elde edilmiş olur.

Güneş pilleri, geliştirilme sıralarına göre üçe ayrılabilir: kristal silisyum güneş pilleri, ince film güneş pilleri ve çok katlı (tandem) güneş pilleri. Kristal silisyum ve ince film güneş pilleri tek eklemli, çok katlı güneş pilleri ise çok eklemlidir. Tek eklemliler arasında en yüksek verime sahip olan güneş pili kristal silisyum güneş pilleridir ve verimleri % 25 civarındadır. Ancak kristal silisyumun pahalı oluşu ve güneş pilinin üretimi sırasında kullanılmakta olan kristal silisyumun kaybının çok fazla oluşu kullanımlarını kısıtlamaktadır. Bu sebeple kristal silisyum güneş pillerine alternatif olarak ince film güneş pilleri geliştirilmiştir. İnce olmaları ve üretimlerinin ucuz olması sebepleriyle ince film güneş pilleri son zamanlarda oldukça öne çıkmaktadır. İnce film güneş pilleri arasında en ilgi çekeni amorf silisyum güneş pilleridir. Verimleri % 13 civarındadır, yani pek yüksek değildir. Ancak üretimlerinin çok ucuz olması sebebiyle amorf silisyum güneş pilleri en çok tercih edilen ince film güneş pili olmaktadır. Çok katlı güneş pillerinde ise birden fazla yarıiletken kullanılarak absorbe edilebilen foton sayısı arttırılarak, güneş pilinin veriminin arttırılması amaçlanmıştır. Bu güneş pillerinin verimi % 44' lere ulaşmaktadır.

Bu çalışmada ince film güneş pili uygulamalarında çokça kullanılan amorf silisyum ve nanokristal silisyum güneş pillerinin verimlerini arttırmaya yönelik çalışmalar yapılmıştır. Amorf silisyum güneş pilleri daha çok Plazma Destekli Kimyasal Buhar Biriktirme (Plasma Enhanced Chemical Vapor Deposition - PECVD) yöntemi ile üretilmektedir. Ancak PECVD yönteminde kullanılan silan gazının (SiH_4) oldukça zararlı olması ve bu yöntemde hidrojen gazının yapıya kontrollü verilemiyor oluşu büyük bir dezavantaj teşkil etmektedir. Bu sebeple son yıllarda amorf silisyum ince filmlerini elde etmek için Magnetron Saçtırma yöntemi kullanılmaya başlanmıştır. Bu yöntemde sistemdeki parametrelerin kontrol edilebiliyor oluşu sebebiyle arzu edilen tarzda kaplamalar yapılabilmektedir. Ayrıca sistemin ultra yüksek vakum

şartlarında çalışıyor olması sayesinde çok temiz filmler elde edilebilmektedir. Bunun yanında düşük sıcaklıkta amorf silisyum kaplamalarının yapılabiliyor olması ve sistemde çevreye zararlı gazların kullanılmıyor olması da sistemin bir diğer avantajıdır. Bu yönleriyle Magnetron Saçtırma yönteminin kullanımının PECVD yöntemine göre daha avantajlı olduğu söylenilebilir. Bu nedenle bu çalışmada Magnetron Saçtırma yöntemi kullanılarak öncelikle kontrollü bir şekilde amorf silisyum kaplamasının yapılması ve ardından belirli bir sıcaklıkta, belirli bir süre tavlama işlemi yapılarak amorf silisyum matrisi içerisinde nanokristal silisyum parçacıklarının oluşturulması amaçlanmıştır.

Çalışmalar boyunca Doğru Akım (DC) ve Radyofrekans (RF) olmak üzere iki farklı güç kaynağı kullanılmıştır. Çalışmalara öncelikle DC güç kaynağı kullanılarak başlanmıştır, ardından RF güç kaynağına geçilmiştir. İki tip hedef malzemesi kullanılmıştır, bunlar preslenmiş ve düşük sıcaklıkta sinterlenmiş toz silisyum ve altlık olarak kullanılan (111) yönlenmeli tek kristal silisyumdur. Altlık olarak doğal oksitlenmiş (111) yönünde tek kristal silisyum ve kuvars cam kullanılmıştır. Çalışmalarda hidrojen gazı kullanılmamıştır, saf amorf silisyum eldesi amaçlanmıştır. Amorf silisyum elde etmek için yapılacak olan her bir kaplama öncesinde tek kristal silisyum altlık üzerine 150 Å kalınlığında titanyum kaplama yapılmıştır. Bunun ilk sebebi, silisyum altlık üzerine silisyum kaplama yapılacağı için epitaksiyel oluşum ihtimalinin önüne geçilmek istenmesidir. İkinci sebebi ise titanyumun silisyumu kolay bir şekilde tutmasından dolayı hedef malzemeden gelen silisyum parçacıklarının kolaylıkla silisyum üzerine tutunabilecek olmasıdır.

Yapılan her bir kaplamanın ardından numuneler XPS’ te incelenmiştir. Ayrıca numuneler Atomik Kuvvet Mikroskobu (AFM), Raman Spektroskopisi, X-Işını Difraksiyonu (XRD) ve Taramalı Elektron Mikroskobu (SEM) cihazlarında incelenmiştir.

Deneysel çalışmaya DC gücünde kaplama yapılarak başlanmıştır. DC güç kaynağında sadece toz silisyum hedef malzemesi kullanılmıştır. Öncelikle 1 Watt, 4 Watt, 10 Watt ve 15 Watt güçlerinde, 2.7 sccm argon akış hızında ve 18 ºC sıcaklıkta kaplama yapılması hedeflenmiştir. Başlangıçta kaplama hızları XPS desteği ile atomik hassasiyette hesaplanmış, ardından kaplamalar yapılmıştır. Yapılan hesaplar sonucunda uygulanan gücün artışı ile beraber kaplama hızının arttığı gözlemlenmiştir. Bunun sebebi, güç artışı ile beraber argon gazını oluşturan argon atomlarının kaynak malzeme yüzeyine aktardığı momentumdaki artıştır ve bunun sonucunda hedef malzemenin yüzeyinden daha çok partikül kopmaktadır. Bu numunelerin AFM’ den alınan görüntülerinde yuvarlak şekilde partiküller gözlemlenmiştir. Bunun üzerine bu partiküllerin davranışını incelemek için çalışılan en düşük ve en yüksek güç değerleri olan 1 Watt ve 15 Watt’ ta plazmanın tuttuğu en düşük ve en yüksek argon akış hızları belirlenerek, bu değerlerde kaplama yapılmasına karar verilmiştir. Yapılan çalışmalarda 1 Watt için plazmanın tuttuğu en düşük akış hızı 2 sccm, 15 Watt için ise 0.8 sccm olarak tespit edilmiştir. Diğer yandan sisteme verilebilecek en yüksek argon akış hızı 20 sccm olduğu için bu değer her iki güç için de en yüksek değer olarak belirlenmiştir. Bu sonuçlar ışığında yapılan kaplamalardan elde edilen AFM görüntülerinde en düşük argon akış hızında her iki güç değerinde de önceki çalışmada görülen yuvarlak şekilli partiküller neredeyse hiç gözlenmemiş, en yüksek argon akış hızında ise yuvarlak şekilli partiküllerin yoğunluğunun arttığı görülmüştür. Toz silisyum hedef malzemesi sinterlenme işlemine tabi tutulmadan, sadece preslenmiş olduğu için partiküllerin hedef malzemesinden kolay ayrıldığı düşünülmüştür ve bundan dolayı argon akış hızı arttıkça hedef malzemesinden kopan partikül sayısı artış göstermiştir. Bu çalışmanın sonucunda partiküllerin altlık üzerine düşüş yoğunluğunun argon akış hızının değişimiyle nasıl kontrol edilebileceği belirlenmiştir.

Bu iki çalışmadan elde edilen XRD sonuçlarına göre elde edilen filmlerin amorf olduğu hem düşük açılarda gözlemlenen kamburluktan, hem de yeni bir pikin oluşmayışından anlaşılmıştır. Yine de amorfluğu teyit etmek amacıyla 15 Watt gücünde ve 2.7 sccm argon akış hızında lamel cam altlık üzerine silisyum kaplaması yapılmıştır. Bu numuneden elde edilen XRD sonucunda oluşturulan ince filmin amorfluğu ispatlanmıştır, çünkü sadece altlıktan gelen kambur bir pik haricinde spektrumda yeni bir pik gözlemlenmemiştir.

Daha sonra RF gücüne geçilmiştir. Bu güçte toz silisyum hedef malzemesi haricinde bir de altlık olarak kullanılan (111) yönünde yönlenmiş tek kristal silisyum altlık hedef malzemesi olarak kullanılmıştır. Bu sette 10 Watt, 15 Watt ve 150 Watt güçlerinde, 2.7 sccm akış hızında ve 18 ºC sıcaklıkta kaplamalar yapılmıştır. DC gücü ile karşılaştırma yapılabilmesi açısından 1 Watt ve 4 Watt değerlerinde de kaplama yapılması düşünülmüştür, ancak bu değerlerde 2.7 sccm argon akış hızında plazma tutmadığı için 1 Watt ve 4 Watt kaplamaları yapılmamıştır. Önce toz silisyum hedef malzemesi ile, ardından silisyum altlık hedef malzemesi ile kaplama işlemleri yapılmıştır. AFM' den elde edilen sonuçlarda her iki hedef malzemesi için de, güç arttıkça pürüzlülüğün arttığı gözlemlenmiştir. Görüntülerin her iki hedef malzemesi için karşılaştırması yapıldığında toz silisyum hedef malzemesinde daha fazla yuvarlak partiküllerin görüldüğü, silisyum altlık hedef malzemesinde ise yüzeyin oldukça düzgün olduğu görülmüştür.

DC ve RF gücünde toz hedef malzemesi kullanılarak yapılan kaplamaların karşılaştırılması yapılırsa, RF gücünde yüzeyin daha düzgün ve homojen olduğu görülmektedir. Bu sebeple RF' in silisyum kaplamaları için daha uygun olduğu söylenebilir.

RF gücünde yapılan silisyum kaplamalar için ayrıca Raman Spektroskopisi cihazında ve XRD' de incelenmiştir. Raman spektroskopisinde amorf silisyuma ait olan 470 cm^{-1}' de bir pik oluşumu gözlemlenmiştir, dolayısıyla amorf yapı kanıtlanmıştır.

Bu çalışmaların ardından nanokristal silisyum partiküllerinin elde edilmesi amacıyla öncelikle RF gücünde, toz silisyum hedef malzemesi ve silisyum altlık hedef malzemesi ile kuvars ve tek kristal silisyum altlık üzerine eşzamanlı kaplamalar yapılmıştır. Kuvars altlığın kullanılmasının sebebi hem yüksek sıcaklığa dayanıklı olmasından, hem de kuvarsın amorf olmasından dolayı Raman Spektroskopi cihazında kristal silisyum piklerinin çakışmasının önlenmek istenmesindendir. Her iki hedef malzeme için kaplamalar 15 Watt gücünde, 2.7 sccm argon akış hızında ve 18 ºC sıcaklıkta yapılmıştır. Ardından numuneler 800 ºC' de birer saat tavlanmışlardır. Yapılan Raman Spektroskopi karakterizasyonu sonucunda, her iki hedef malzemesinde elde edilen kaplama için kristal silisyuma ait olan 520 cm^{-1}'deki pik spektrumlarda gözlemlenmiştir. Spektrumlarda ayrıca tek kristale ait olan pikte gözlemlenen kamburluğun amorf silisyuma ait olduğu düşünülmüştür. Dolayısıyla amorf silisyum matrisinde nanokristal silisyum parçacıklarının elde edildiği ispatlanmıştır.

Bütün bu çalışmaların sonucunda amorf silisyum elde etmek için RF gücünün daha uygun olduğu anlaşılmıştır. Ayrıca daha temiz ve düzgün bir yüzey elde etmek için silisyum altlık hedef malzemesinin kullanımının, toz silisyum hedef malzemesinden daha uygun olduğu düşünülmektedir.

Sonuç olarak amorf silisyum üretiminde Magnetron Saçtırma yönteminin PECVD kadar başarılı bir yöntem olduğu bu çalışma ile anlaşılmaktadır.

1. INTRODUCTION

Depletion of fossil fuels makes researchers searching new ways to find alternative sources. One of those alternatives is solar cells. Because solar cells are eco-friendly, not having motion parts, working at low temperatures, having long lifetime and the source is sun which is inexhaustible.

Silicon is the most used material in solar cells, because of their abundance in the world, semiconductor properties, cheapness.. etc. It is the second element in the world that found to be most [36]. In addition to this, because of being good semiconductor, it has common usage area one of which is photovoltaic systems. We can say that silicon is the most used material in photovoltaic industry with 88 % usage [37,3]. Because silicon is a very cheap material, 43 % of this ratio is comprised of monocrystalline silicon, 43 % of this is comprised of polycrystalline silicon and 2 % of this is comprised of amorphous/nanocrystalline silicon.

In fact GaAs is the most suitable one for solar cells with the ratio of % 24 in efficiency, but it is very expensive material. Because of this reason, it can not be used extensively [4]. CdTe can be used for solar cells preparation, but because of the fact that Cd is very toxic, its usage becomes limited too [5]. Based on these reasons, silicon becomes the most suitable material for solar cells.

Among the solar cells which are prepared with silicon, amorphous silicon becomes very attractive for scientists, because of its properties that

- Its cheapness due to producing thin films with large surface easily.
- Being able to keep low angle beams and for this reason efficiency is relatively high.
- Efficiency drop is very low, even at low air temperature.

By reason of the fact that pure silicon has a lot of defects, it is insulator [5]. This situation prevents using amorphous silicon in electronic applications [4]. The main reason of this problem is the dangling bonds in silicon structure. If the dangling bonds in silicon structure are passivated by hydrogen, defects can be eliminated.

Thus, the conductivity of silicon can be enhanced substantially and dopping can be done. In addition, hydrogen can prevent formation of columnar structure.

There are several ways to produce hydrogenated amorphous silicon. These are Plasma Enhanced Chemical Vapor Deposition (PECVD), Hot-Wire Chemical Vapor Deposition (HW-CVD) Very High Frequency Glow Discharge and Reactive Magnetron Sputtering (RMS). Among these, PECVD is the most used one. But because of the disadvantage, such as using of silane (SiH_4) gases which is very toxic, scientists have started to pay attention to Reactive Magnetron Sputtering. In Magnetron Sputtering system $Ar+H_2$ are used instead of silane gases. The other advantages of this system with respect to PECVD are

- Higher production rate.
- Production of higher efficiency amorphous silicon solar panels.
- Synthesis can be done at low temperatures.
- Production cost is relatively low.
- It is more controllable system.

The only one problem in this system comes up because of parameters abundance.

In literature, there is a lot of study handled about nanocrystalline silicon structure formed in amorphous silicon matrix. This formation increases efficiency. This is because of being held photons with low energy [7]. Besides that because of hydrogenated amorphous silicon may degrade due to light, using in electronic applications is limited. So creating nanocrystals in amorphous silicon matrix makes structure more stable and increases efficiency [7]. Formation of nanocrystals occurs with annealing after deposition on sample. The size and number of nanocrystals effect keeping sun beams. Hydrogenated nanocrystalline silicon has high dopping efficiency and mobility capability [8].

There are several parameters that effect formation of nanocrystals. These are annealing temperature, pressure, reactive gases, duration under plasma conditions and bias field.

Annealing temperature is a significant effect on formation of nanocrystals. In unannealed sample, there is no formation of nanocrystal [9]. By increasing of temperature, the number of crystal particles increases.

90 % of ratio of nanocrystalline formation is obtained in literature [10]. This ratio of nanocrystalline is obtained by changing pressure. In a study, for thin film samples deposited at 2, 3 and 4 Pa pressure, the silicon thin film deposited at 2 Pa is totally amorphous, but on the other hand, there is formation of nanocrystals on the samples deposited at 3 and 4 Pa [7, 10]. Again in the same study, 90 % of nanocrystalline formation is achieved at 4 Pa and 100 ^{o}C. Although crystalline formation enhances by increasing of pressure, percentage of pores increases [12]. So, pressure has an important effect on structure.

Another parameter that effects crystalline formation is reactive gas ratio. As is known, in Magnetron Sputtering technique argon and hydrogen gases are used as reactive gases at various ratio. It is the hydrogen that provides hydrogenation of amorphous silicon. Hydrogen has a great effect on crystallization. In a study that investigate this effect, it was found that optimum ratio of Ar/H_2 is %40/%60 [11]. When hydrogen ratio is 100 %, there is not any formation of film observed on substrate. This is because of etching effect of hydrogen [14]. Also at low temperature, experiment done in the environment of 70 % of H_2 and 30 % of Ar gases, it was seen that the highest crystallization degree is achieved. In this serial it is indicated that grains are small [12].

Bias field applied to substrate effects microstructure of films [19]. Increasing of negative bias field decreases holes in film, crystal size and provides formation of a denser structure. Formation of denser structure and decreasing of crystal size is because of ion bombardment. Increasing of negative bias enhances total stress and intrinsic stress in structure. On the other hand, deposition rate decreases and band gap becomes narrower, crystal ratio in structure increases together with that. Because band gap becomes narrower, crystal ratio increases.

In this thesis, obtaining of amorphous silicon without hydrogen dilution and then creating of nanocrystalline silicon in amorphous matrix are aimed. In accordance with this purpose, by using of DC-Magnetron Sputtering and RF-Magnetron Sputtering amorphous silicon thin films were deposited and then some of the samples were annealed for observing nanocrystallization. X-Ray Photoelectron Spectroscopy (XPS) was used for identifying which elements thin film has and its chemical proportion, Atomic Force Microscopy (AFM) was used for scanning surface topography, X-Ray Diffraction (XRD) was used for determining of phases and crystallinity in thin films, Raman Spectroscopy was done for observing amorphousity and crystallinity of thin film and Scanning Electron Microscopy was done for observing thin film laterally.

2. ELECTRONIC STRUCTURE OF MATERIALS

The smallest structure in material is atom. Atom is formed of core and electrons. Electrons determine the electrical and optical properties of materials.

Materials can be classified in terms of their electronic structure as three main groups which are conductors, semiconductors and insulators. Electrons determine which character they will have.

2.1. Band Structure of Solids

If identical atoms are far away from each other that will not affect, their electronic energy levels are the same. When they approach each other, they start to interact. It means that Pauli Exclusion Principle which is used for settlement of electrons in atoms begins to take effect. According to this principle, two electrons having the same quantum number can not be side by side at the same time in solids. This rule is valid, even if solid is too big.

The electrons in atoms occupy fixed and discrete energy levels. Electrons are settled beginning from the bottom of band, while keeping two electrons at each energy levels. Internal bands are completely full, but valence band may not be completely filled depending on solid. For example, a solid which composed of silicon atoms (Si), valence band is completely filled. Allowed and forbidden energy regions for electrons in a solid can be seen from Figure 2.1.

In solids, there is one more empty band which is above valence band and sometimes overlapped with valence band. This band is named as conduction band. This band has very important role for conduction.

There is a need for an empty state that moving of charged particles (electrons) in solids. In other words, if there is an empty state, electrons can move. If there is not, electrons can not move. Even, a voltage is applied, electrons will not move.

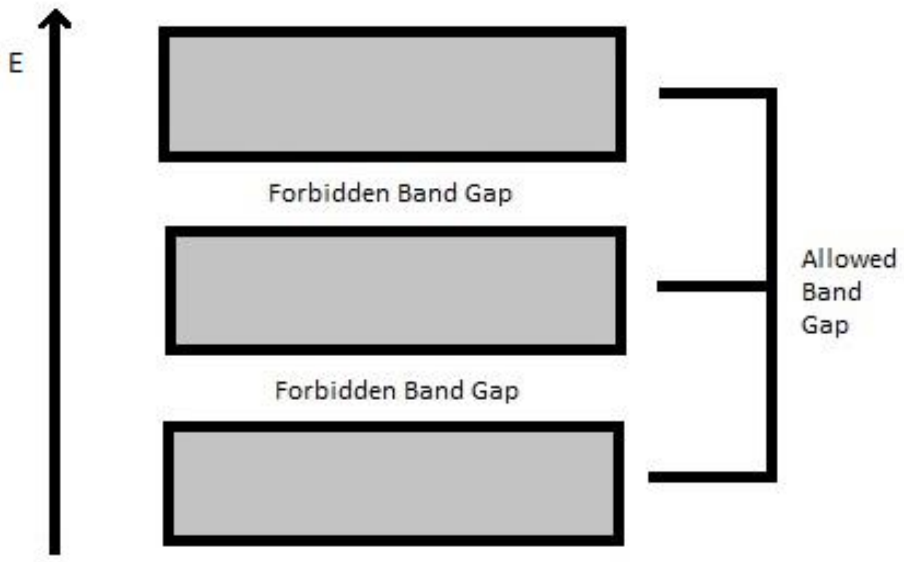

Figure 2.1 : Allowed and forbidden energy regions for electrons in a solid.

According to Figure 2.2 (a), band is not full and there is an energy state in the band that electron can move. In this case, there is not an obstacle for moving of electrons and even at small potential differences, no matter what temperature is, current can be measured. This type of material is known as metal and metals conduct electricity well.

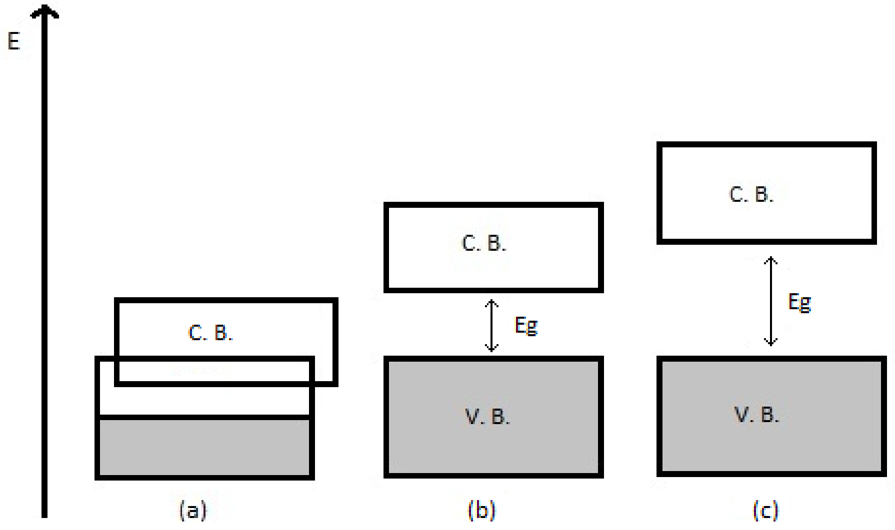

Figure 2.2 : T= 0 ^{o}K, conduction and valence band conditions, (a) metal, (b) semiconductor, (c) insulator.

In Figure 2.2 (b), semiconductor is represented. This type of materials has the energy band gap below 3 eV. In this situation, valence band is full and conduction band is empty.

In Figure 2.2 (c), insulator is represented. In fact there is not a difference between semiconductors and insulators except energy band gap value. The energy band gap is above the value of 3 eV. We can say that both insulators and semiconductors can not conduct electricity, because valence band is completely full and conduction band is empty. This can be said for the condition which is at absolute temperature. It is different at room temperature. Electrons which obtain enough energy (E_g) from environment can jump into conduction band from valence band. This behaviour can be seen in semiconductors, not in insulators.

2.2. Semiconductors

Semiconductor material shows insulator character at absolute zero temperature. But when temperature is increased, it becomes conductor. The typical characteristic of semiconductors is the band gap between valence band and conduction band. At T= 0^{o}K, as valence band is full of electrons, conduction band is empty. To be electrically conductive, charge carriers must move from a state in energy band to another. So under this circumstance, which is that all energy levels are full or empty, conduction can not happen. When temperature is increased or photon which has higher energy than energy band gap of semiconductor is sent to semiconductor, energy which is needed for passing from valence to conduction band is transferred to electrons. Electron leaving from valence band forms a hole behind. When this hole is filled by another electron, it forms a hole behind too. As a result, there can be seen a hole movement because of the electron which leaves valence band.

2.3. Doping of Semiconductors

2.3.1. n-type Semiconductors (Donors)

In silicon crystal, silicon atoms make covalent bonds with each other. So that, each silicon atoms consist of four neighbour atoms. Instead of silicon atom in silicon crystal when phosphorus (P) atom which is one of the element of fifth group in the periodic table is doped, four of the five atoms in phosphorus is used in making covalent bond and fifth electron adhere to phosphorus with small energy (0.04 eV).

When this electron has this much energy, it jumps into conduction band. When this energy is compared with energy band gap of silicon (1.1 eV), it can be seen that this value is much smaller than silicon band gap [28]. As a result of giving fifth electrons of phosphorus, number of electrons increase and there is not any hole formation in valence band. By virtue of this, electron density in semiconductor will be higher than hole density. This type of semiconductors is named as n-type semiconductors and dopant material is named as donor. Conduction increases according to density of dopant in n-type semiconductors. For example, if dopant density increases, conduction will increase too.

2.3.2. p-type Semiconductors (Acceptor)

Instead of a silicon atom in silicon crystal, when boron which is one of the element of third group in periodic table is doped, one empty state remains in one of the Si-B bonds because boron takes three electrons. Lower boron concentration is not enough for doping [1]. This missing electron is filled with an electron which is taken from valence band (Si-Si covalent bond). Required energy is very low (0.04 eV). In this case, boron (B) is named as acceptor. As hole forms in valence band, electrons do not jump into the conduction band. Conduction increases with doping concentration.

2.4. P-N Junctions

When two semiconductors which are dopped n-type and p-type piece together, p-n junction is formed.

Electron deficiency in p-type semiconductor and redundancy of electrons in n- type semiconductor take place. The movement of electrons and holes are opposite to each other. When n-type and p-type piece together, free electrons in n-type and holes in p-type combine. In that case, p-side gains net (-) charge and n-side gains net (+) charge. Because p-side has (-) charge, it pushes electrons of n-type. Similarly, n-side has (+) charge and it pushes holes of p-type. So they prevent flowing of electrons and holes between p-side and n-side. Consequently, a region which is called as “potential barrier” is formed between p-n junction.

Before the application of any potential across the p–n specimen, holes will be the dominant carriers on the p-side, and electrons will predominate in the n-region, as illustrated in Figure 2.3. An external electric potential may be established across a p–

n junction with two different polarities. When a battery is used, the positive terminal may be connected to the p-side and the negative terminal to the n-side; this is referred to as a forward bias. The opposite polarity (minus to p and plus to n) is termed reverse bias [20].

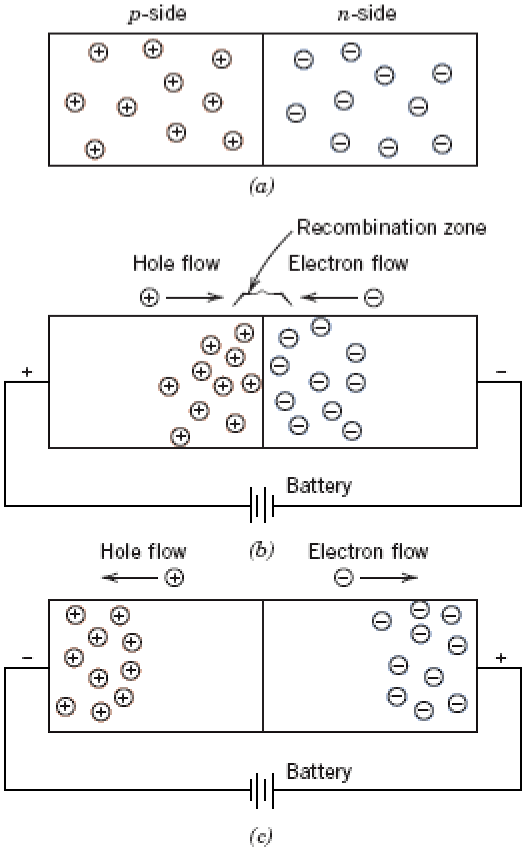

Figure 2.3 : For a p–n rectifying junction, representations of electron and hole distributions for (a) no electrical potential, (b) forward bias and (c) reverse bias [20].

3. SOLAR CELLS

3.1. Solar Energy

Sun which is the source of life provides the most of the energy of natural system. Its diameter is approximately 1.4 million kilometer and it has very dense gases in its internal environment. It is the main source of all fuels used in the world except nuclear energy. Hydrogen is converted to Helium within the Sun continuously, which is named as Fusion. The mass difference formed of this reaction converts to heat energy and spread to the space. The amount of radiation emitted from Sun and reaching the World is approximately 70 %.

Radiation has electromagnetic property. Most of radiation which comes to the World is in visible region. It can be seen from Figure 3.1 that in visible region, red has the lowest energy. On the other hand, purple has the largest energy.

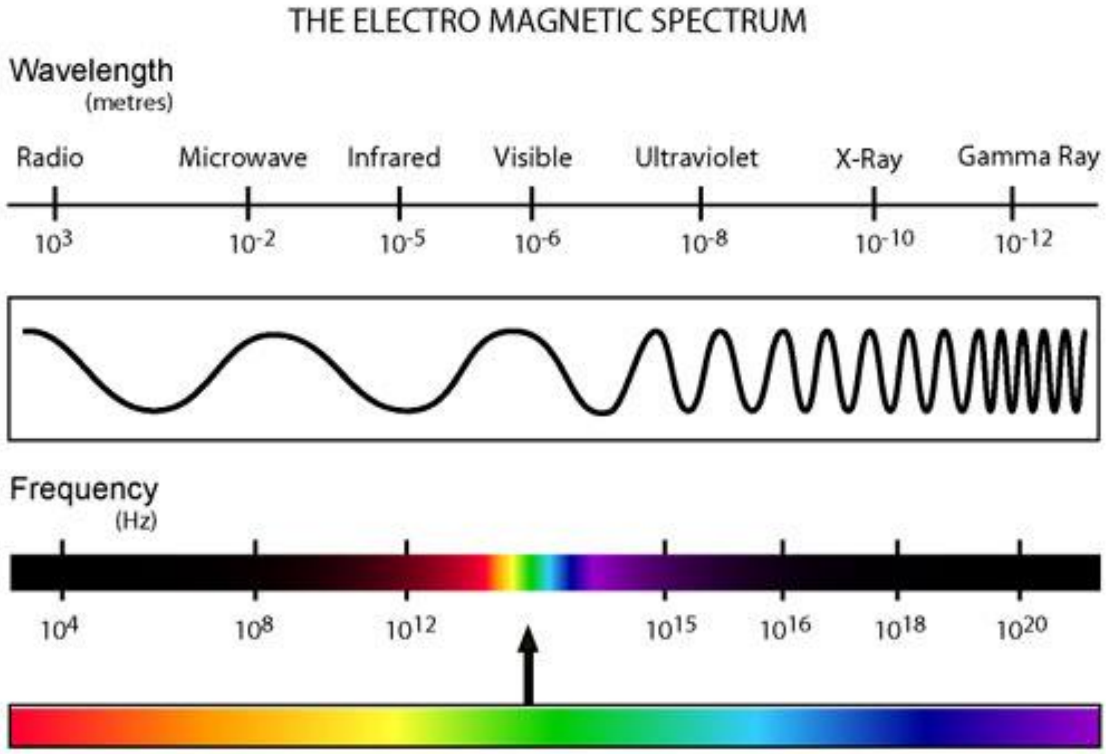

Figure 3.1 : Electromagnetic spectrum [40].

In all over the world there is a necessity for searching renewable energy sources, because of the shortage of fossil fuels. Renewable energy sources can be described as:

- Solar Energy
- Wind Energy
- Hydroelectrical Energy
- Geothermal Energy
- Biomass
- Wave Energy
- Hydrogen Energy

Turkey has more advantages than other countries to enhance solar energy technologies in terms of sunlight potential, because of its location.

3.2. Solar Cells

Solar cells are devices that convert solar energy directly to electrical energy. Cell generates electrical energy as long as sunlight falls on cell. It is not necessary to charge solar cells like others, because source of solar cells is sunlight which is inexhaustible. In addition, solar cells are environmental friendly and they have not any moving part. Their application field are increasing day by day. Nowadays solar cells are used in traffic lights, street lights, agricultural irrigations, spacecrafts ... etc.

3.2.1. Working Principle of Solar Cells

When sunlight comes to solar cell, it charges the valence electron in the last orbit negatively. Light is formed of energy particles which are named as photon. When photons crash to an atom, all atoms become energized and the valence electron in the last orbit ruptures. In this electron which is released, potential energy emerges. This energy can be used for charging a power supply or running an electrical motor. The important point is that taking these free electrons out of cell. During production, there is constituted an internal electrostatic region which is near the front of cell and electrons are provided to become free. Other elements are inserted to silicon crystal. The presence of these elements in crystal prevents being in electrical balance. In material which encounters with light, these atoms break balance and they push free electrons to other cell or surface of cell for going to charge. While millions of photons flow into the cell, they gain energy and jump into higher level. Electrons flow to electrostatic region in cell and then out of cell. This flow is electrical current.

3.2.2. Light Absorption

Electron-hole formation takes place via either increasing of temperature or absorption of photon which has higher energy than $h\upsilon > E_g$, because electron jumps into conduction band from valence band.

The energy of photon which has the frequency of υ is

$$E = h\upsilon = \frac{hc}{\lambda} \qquad \text{(Eq. 3.1)}$$

h: Planck's constant

c: Speed of light

υ: Frequency

λ: Wavelength

If speed of light and Planck's constant put into equation, then it becomes

$$E = \frac{1.24}{\lambda}(\text{eV}) \qquad \text{(Eq. 3.2)}$$

To absorb incident photon, photon must have the energy which is equal to the band gap of semiconductor (E_g) or higher than the band gap of semiconductor. If the energy of photon is very high, solar cell will heat up. This effect disrupts structure of solar cell. Because of that, semiconductor to be used in preparation of solar cell must have convenient energy band gap.

As said before, the band gap is the difference in energy between the lowest point of conduction band (conduction band edge) and the highest point of the valence band (valence band edge).

In the direct absorption process, a photon is absorbed by the crystal with the creation of an electron hole pair. Semiconductors using the phenomena have their valence band maxima and their conduction band minima corresponding to the same momentum and are called direct-gap materials.

In the indirect absorption process, the band gap involves electron and holes separated by a wave vector kc i.e. the maximum of valence band and minimum of conduction band do not correspond to the same momentum. Such materials are called indirect gap materials [21]. Direct and indirect band gap models can be seen from Figure 3.2.

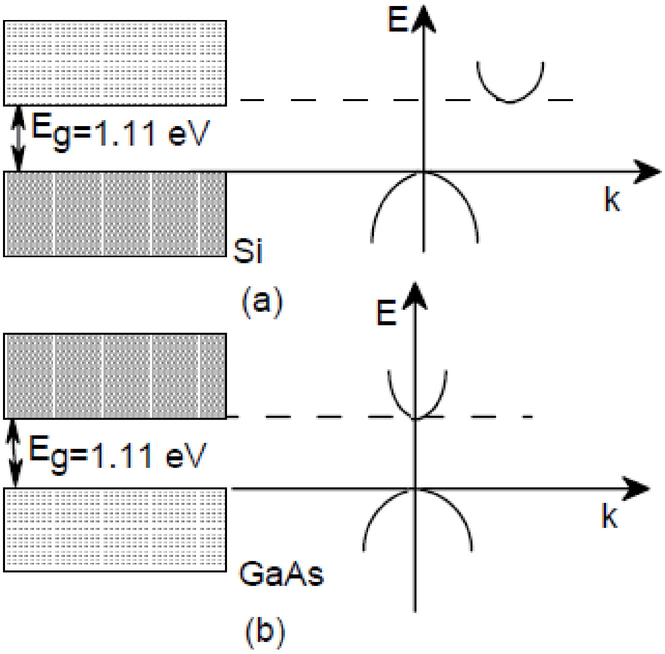

Figure 3.2 : Approximately the E-k diagram at the bottm of the conduction band and at the top of the valence band of Si and GaAs by parabolas [21].

3.2.3. Types of Solar Cells

Solar cells can be classified into three main groups in terms of development process:

1) First Generation: Crystalline Solar Cells (Monocrystalline silicon solar cells and polycrystalline silicon solar cells)
2) Second Generation: Thin Film Solar Cells (Amorphous silicon, Cadmium telluride, Copper Indium/Indium Gallium Diselenide)
3) Third Generation: Tandem Solar Cells

3.2.3.1 First Generation: Crystalline Solar Cells

Silicon which shows semiconductor character completely is used production of solar cell mostly. Silicon is preferred not only for its technological supremacy, but also for economic reasons. Crystalline solar cells constitute the large part of marketshare, its usage reaches 85 %.

a) Monocrystalline Silicon Solar Cells

The production method used for monocrystalline silicon is Czochralski growth technique mostly. Its yield is up to 25 % [39]. This type of silicon is the most efficient one. But due to its expensiveness and lots of material loss, different alternatives are investigated.

b) Polycrystalline Silicon Solar Cells

Because production of monocrystalline silicon is very expensive, polycrystalline silicon solar cells was thought to be as a good alternative. However, its yield is lower than monocrystalline solar cells due to material quality. Enhancing of material quality studies provide a little increment. Nowadays, yield of polycrystalline solar cell reaches 20 %.

The main obstacle in usage of monocrystalline solar cells is material loss. On the purpose of reduction of material loss, these cells are produced from silicon layers in plaque form.

3.2.3.2. Second Generation: Thin Film Solar Cells

Materials which have better absorbent property are used in this technique with one in five hundred thickness. For example; absorbent coefficient of amorphous silicon solar cells is higher than absorbent coefficient of monocrystalline solar cells. While the sun radiation whose coefficient of wave length is smaller than 0.7 micron can be absorbed with 1 micron thickness of amorphous silicon, it takes 500 micron thickness of crystal silicon to create the same effect. Because of that, less material is used in thin film solar cells and installation is easier.

a) Amorphous Silicon (a-Si)

Amorphous silicon solar cells (a-Si) are at the forefront of thin film solar cell technology. The first one of amorphous silicon cells were in Schottky form, afterwards p-i-n structures were made. Although amorphous silicon solar cells have lower yield than others, they are commonly used because of low production cost. They are eco-friendly and produced from silicon which is a lot in nature.

b) Cadmium Telluride Solar Cells (CdTe)

Thin-film cadmium telluride (CdTe) solar cells are the basis of a significant technology with major commercial impact on solar energy production. Large-area monolithic thin film modules demonstrate long-term stability, competitive performance, and the ability to attract production-scale capital investments [41]. But the usage of this type of solar cell is limited, because cadmium is a toxic material. The yield of CdTe solar cell is up to 17 % [39].

c) Copper Indium/Indium Gallium Diselenid Solar Cells(CIS/CIGS)

It is composed of copper, indium, selenium and sometimes gallium. In the thin film group, CIS/CIGS technology has demonstrated the highest efficiency rating, high stability in (kwh) output, little or no degradation and excellent performance in low light conditions [42]. Its efficiency reaches 20.3 % [39]. The disadvantage of this type is that production is hard and complicated because of using multiple elements.

3.2.3.3. Third Generation: Tandem Solar Cells

The obstacle in front of single layer solar cells is residual heat that because of photon with higher band gap. A way to decrease this heat is bunching different solar cells having different energy band gap together. On the other hand, multiple junction (tandem) solar cells are used to get higher efficiency than possible with a single junction solar cell. By virtue of this way, efficiency reaches 42.4 %.

3.3. Silicon Thin Film Solar Cells

3.3.1. Amorphous Silicon

Silicon atoms in amorphous silicon nearly resemble the structure of crystalline silicon, except being short range order. Amorphous silicon does not exhibit long range order, but there is a similarity in atomic configuration on an atomic scale like seen in crystalline silicon. All silicon atoms in amorphous silicon are connected to the other four silicon atoms as a tetrahedron by covalent bond. Though amorphous silicon lacks the long range order, it has some short range order like crystalline silicon. The structure of amorphous silicon is known as “random continuous network”.

In fact, all atoms in amorphous silicon are not fourfold coordinated, some atoms may be threefold coordinated. This means that a silicon atom has one unpaired electron. This is called as “dangling bond”. Physically, these dangling bonds behave as defect in continuous random network and they may cause abnormal electrical behaviour. For amorphous silicon, hydrogen solves this problem. While some of the silicon atoms make covalent bonds with three neighbours, fourth valence electron of silicon bonds to hydrogen atom.

To understand the electronic and optical properties of amorphous silicon, it is necessary to know its band structure. Normally, an ideal crystal has well defined band gap between valence and conduction band. Since not having long range order, in other words because bond length and bond angle is different and amorphous silicon has dangling bonds, there are lots of localized defect states in band gap of amorphous silicon as distinct from crystals. Since dangling bonds are saturated with hydrogen atoms in hydrogenized amorphous silicon, number of defect states decreases prominently as it is seen from Figure 3.3 [22].

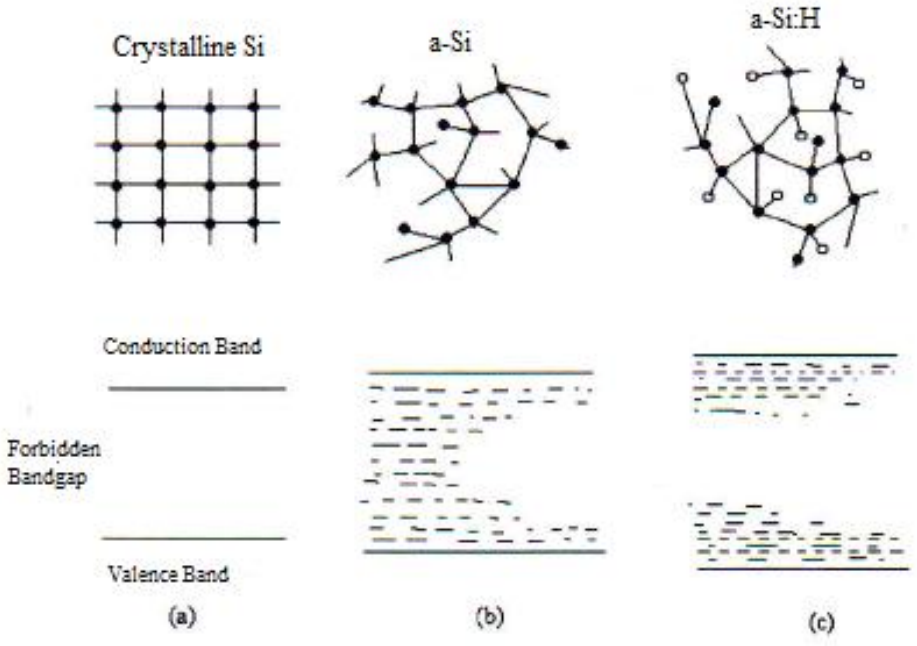

Figure 3.3 : a) Crystalline Silicon, b) Amorphous Silicon, c) Hydrogenated Amorphous Silicon atomic arrangement and band structure [22].

Defect concentration of pure amorphous silicon is about ~10^{19} cm^{-3} which is very high value. This level decreases electronic conductivity dramatically. Due to disorder in amorphous silicon, there are lots of unsaturated dangling bonds in structure. This remains as defect states in energy band gap of amorphous silicon. But when H_2 atoms are added to structure, electronic conductivity of amorphous silicon enhances. Lots of dangling bonds are passivated with hydrogen atoms. Thus, defect density decreases ~10^{15} cm^{-3} degree.

The atomic arrangement and microstructure of a-Si:H is shown in Figure 3.4. As it is said before, the atomic arrangement of a-Si:H is characterized by the same local order as crystalline silicon. Each Si atoms are bonded to four neighbour silicon atoms. But atoms do not have long range order which is seen in crystalline silicon that bond length and bond angle are same along the structure. In amorphous silicon, bond length and bond angle may vary through arrangement. Si-Si bonds can be stretched or compressed, or the angle between Si atoms can be affected by the amorphous matrix [36]. Variation of bond length and angle effects electronic properties that tail states comprise between conduction and valence band. Lack of bonding of four silicon neighbour atoms cause creating of unsaturated dangling bonds of Si-H bonds.

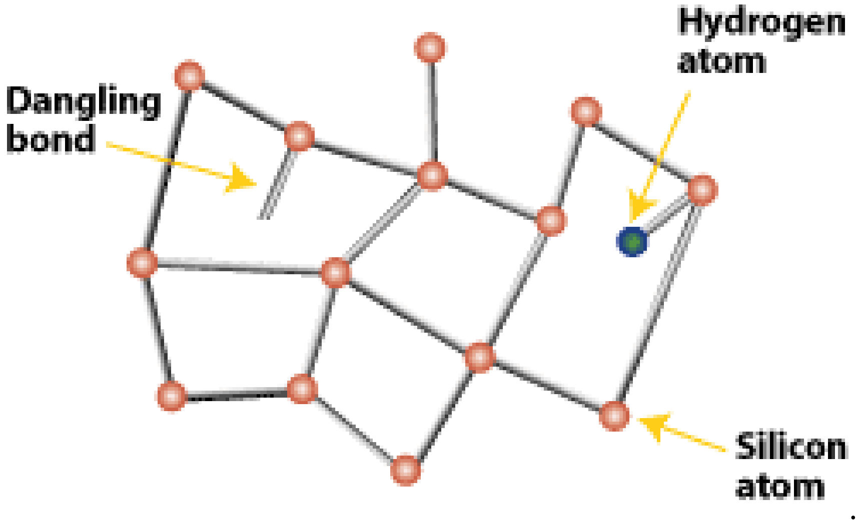

Figure 3.4 : Schematic drawing of the atomic structure and microstructure of hydrogenated amorphous silicon [38].

As a result of hydrogenization of amorphous silicon, structure becomes relaxed. Because of that, electronic properties of a-Si:H is different from crystalline silicon. In c-Si the periodic arrangement of Si atoms leads to sharply defined valence and conduction band edges as can be seen in Figure 3.5 (a). The gap between these two edges is defined as the band gap. In a-Si:H the amorphous arrangement of Si atoms leads to continuous distribution of electronic states with tail states and defect states located energetically in between the extended band states, as can be seen in Figure 3.5 (b). The mobility gap is indicated in the figure, which represents the energy gap which must be overcome by electrons to get from one delocalized extended state in the valence band to another delocalized state in the conduction band. Electronic states in the band tails are considered to be localized states [36]. The band gap of amorphous silicon is larger than crystalline silicon. The band gap of amorphous silicon is 1.8 eV.

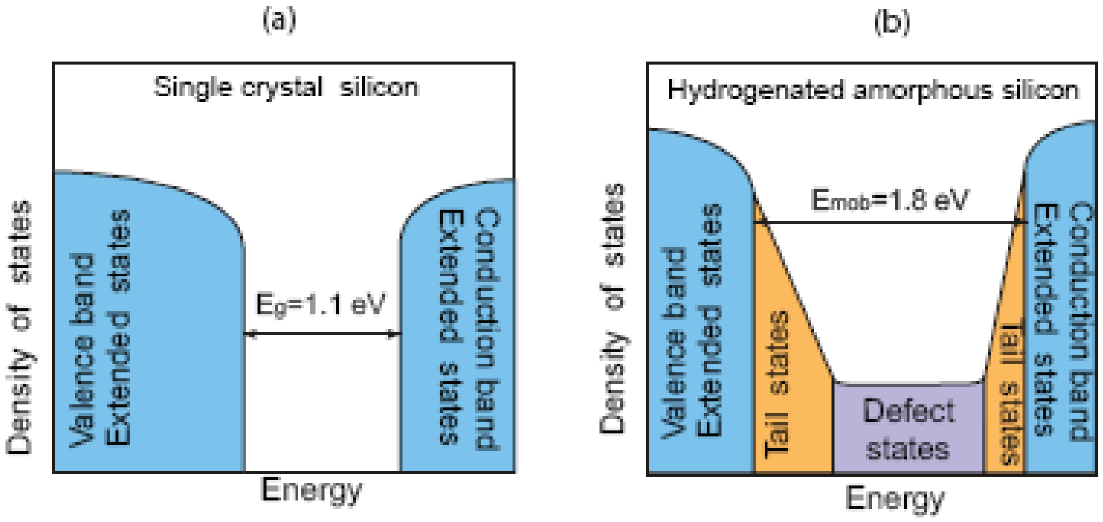

Figure 3.5 : Schematic densities of states for (a) crystalline silicon and (b) hydrogenated amorphous silicon [36].

3.3.1.1. Staebler-Wronski Effect

It is the light-induced degradation seen in amorphous silicon solar cells. Its name belongs to researchers Staebler and Wronski who observed this effect at first in 1977. They synthesized amorphous silicon via Glow Discharge and under prolonged illumination, they observed that dark conductivity and photoconductivity decreased significantly. These changes could be reversible by the help of annealing at elevated temperatures (>150 °C) and were attributed to a reversible increase in density of gap states acting as recombination centers for photoexcited carriers and leading to a shift of the dark Fermi level E_F toward mid gap [23].

There are lots of models suggested for metastable illumination defect. The most acceptable one is recombination of photocarriers. It is a model that recombination of photocarriers break weak Si-Si bonds and metastable defects arise. In this model, during recombination of photocarriers, non-radiative energy release accompanied and it is enough to break the bond. A hydrogen atom which is back-bonded to silicon prevents rebuilding of breaking bonds by bond switching. Staebler-Wronski Effect effects efficiency of solar cells produced using amorphous silicon significantly.

3.3.2. Nanocrystalline Silicon

Even though amorphous silicon has many advantages, it has some disadvantages that effect usage of amorphous silicon. These disadvantages are Staebler-Wronski effect and low efficiency. The advantages of nc-Si:H are stability against light-induced degradation and the extension of its spectral response to the near infrared light region. When amorphous silicon samples are annealed at proper temperature, nanocrystallized particles are obtained.

Nanocrystallized silicon is formed of a mixed phase material which is composed of amorphous silicon matrix, nanocrystalline particles and voids. Deposition techniques and substrate material effect microstructure. Nanocrystalline silicon shows similar behaviour with amorphous silicon about optical properties. By comparison, nc-Si:H has lower absorption coefficient than a-Si:H at the region of short wavelength spectral region (>1.7 eV). But nc-Si:H can absorb energy from photon in the region between 1.1-1.7 eV where amorphous silicon shows reduced response. It can be said that this higher absorption effect is related with combined effect of amorphous silicon and nanocrystallized silicon. The absorption as a function of wavelength of nanocrystalline silicon compared with a-Si:H can be seen from Figure 3.6.

As said before, deposition conditions and substrate material effect microstructure. The size and number of nanocrystalline particles effect properties of structure. Size and number of nanocrystals depend on level of hydrogen dilution during deposition. Grain sizes increase directly as the hydrogen dilution increases. Increasing hydrogen dilution beyond the amorphous to nanocrystalline transition results in large grain sizes with the associated voids and grain boundaries [25].

Structure of nc-Si:H is heterogeneous. It has nanocrystalline particles, amorphous component and voids. Randomly oriented crystallites are embedded in columns. Just like a-Si:H, nc-Si:H has defects which effect efficiency of solar cells significantly.

Defects in nc-Si:H may exist in grain boundaries between crystallites, in amorphous matrix or at surface.

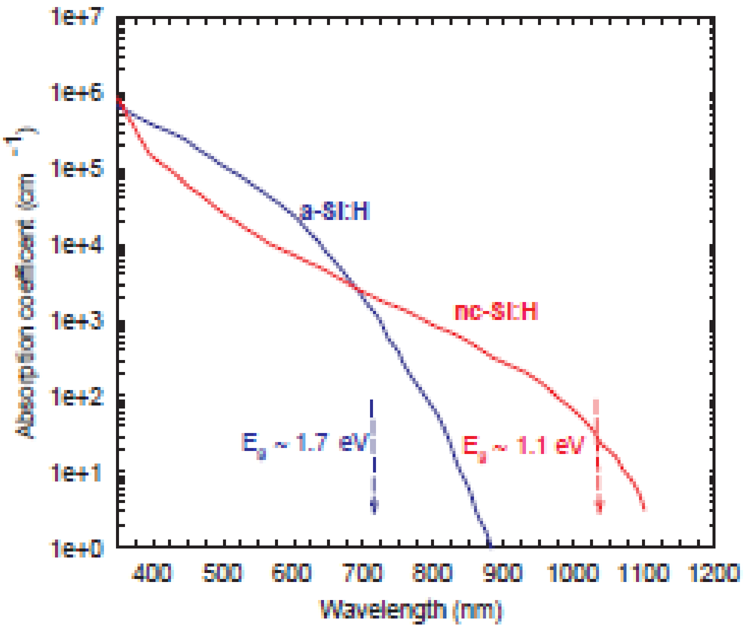

Figure 3.6 : The absorption as a function of wavelength of thin film nanocrystalline silicon compared to that of a-Si:H. The band gaps, E_g, of the two materials are shown [24].

The crystalline mass fraction (*f*) of nc-Si:H is an important issue for application of solar cell. This effects optical properties as well as electrical properties. Certain amount of increment of crystal mass fraction is favourable but extreme increase is not good for performance of solar cells. With increasing of crystallinity, density of grain boundaries and voids increase too, which cause constituting of defect and deteriorate solar cell efficiency. Optimized proportion of crystallinity is above 50 % [26].

4. MAGNETRON SPUTTERING

It is a type of physical vapour deposition (PVD) technique that obtain thin films in nanometer range. Sputtering is a process whereby atoms are ejected from a solid target material due to bombardment of the target by energetic particles [27]. Particles used in surface bombardment are generally heavy noble gas. If gas is light, bombardment will not be effective. Argon is the most used gas in sputtering. Sputtering is not only used for deposition, but also for etching. But it is mostly used for sputtering.

In general manner, sputtering happens when cathode surface is bombarded by high energy ions. During sputtering, particles leaving from surface or sputtered atoms are the atoms that have energy which vary between 1-10 eV and constitutes cathode. These high energy range is the most important property of magnetron sputtering. When energy range of magnetron sputtering is compared with the energy created by evaporation, it is much higher. Another reason to choose magnetron sputtering is that magnetron sputtering is a high vacuumed system. Because of that in this system very clean thin films can be obtained. It is important to acquire thin films without impurity.

Another advantage of magnetron sputtering systems is that sputtering yield is higher than conventional sputtering systems. In conventional sputtering system, sputtering yield is increased by the help of increasing operating power. Because operating power increases, ion flow towards to target surface increases too and sputtering yields enhance. But in magnetron sputtering system, increasing of sputtering yield is provided by magnet which is located back of the target. It enables trapping of electrons, which come out during ionization, in magnetic field. By this means, ion density rises near the target and this increases the amount of Ar^+ ions, so sputtering yields enhances considerably.

In magnetron sputtering system, target material is placed on a holder which consists of water cooled magnet or electromagnet. While centreline of target constitutes one pole of magnet, second pole is constituted from magnets which is placed edge of target shaped like circle. This way of design provides that magnetic field and electric field are orthogonal to each other. Magnetic fields can be designed shaped like circular or rectangular. Shape of magnetic field and motion path in circular shaped magnetic fields are shown in Figure 4.1.

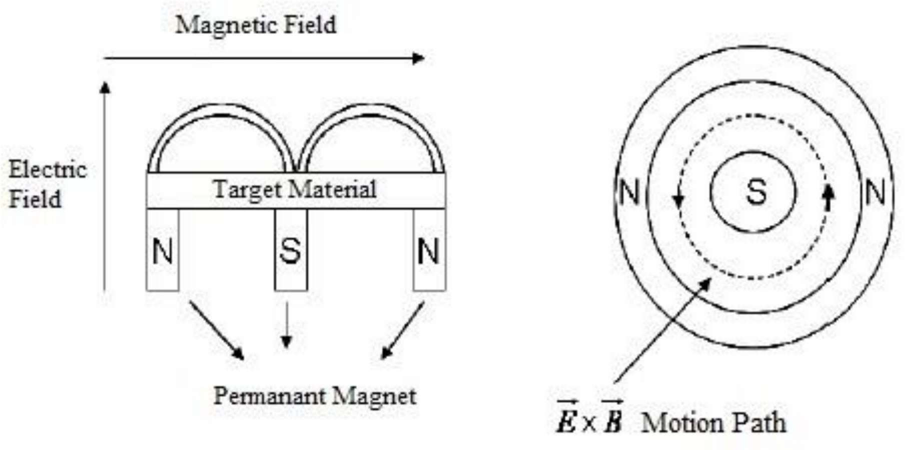

Figure 4.1 : Circular magnetic field [2].

In ExB which expresses motion path, E and B represent electric field and magnetic field, respectively. ExB motion path is parallel to target surface and constitutes closed circle. Thus, secondary electrons leaving from cathode via ion bombardment cause increasing of ionization and making plasma denser [2].

By the help of increasing of ionization effect, magnetic field which creates plasma at lower working pressure can be generated. With decreasing working pressure, because sputtered target atoms are less at gas phase, it is provided that number of particles reaching at substrate increases and so deposition rate increases too.

Factors that effect deposition rate are target material, distance between target and substrate, power applied to target, area of target and working pressure.

5. X-RAY PHOTOELECTRON SPECTROSCOPY

Photoelectron Spectroscopy used for getting information about electronic structure is based on photoelectric effect. This method is based on the principal that photoelectrons, which are emitted from surface illuminated by monochromatic light source, are detected by the help of electron energy analyzer according to their kinetic energies.

$$E_k = h\upsilon - E_b - \Phi \qquad \text{(Eq. 5.1)}$$

In this equation $h\upsilon$ is "sending photon energy", Φ is "working function", E_b is "binding energy" and E_k is "kinetic energy which electron has at vacuum level". Working function, Φ is the energy which is necessary for the electron to jump from Fermi level to vacuum level. Binding energy, E_b is the position of electron according to Fermi level.

Photoelectron Spectroscopy is named differently, according to photon energy which is used. If photon energy is $h\upsilon$ between 200 and 2000 eV, it is named as X-Ray Photoelectron Spectroscopy (XPS). If energy is between 10-60 eV, the method is named as Ultraviolet Photoelectron Spectroscopy (UPS).

XPS, which is used for surface characterization research, is a spectroscopic analysis technique with high sensitivity based on electron-energy analysis. It is possible to obtain information about chemical composition and chemical states of surface component by the help of XPS.

In XPS method, sample is settled in high vacuumed system and exposed to X-ray. As X-ray source, generally monochromatic Al-K_α-1486.6 eV or Mg-K_α-1253.6 eV are used. Incident X-rays stimulate electrons at core levels. Photoelectron energy emitted from core levels is a function of binding energy and photoelectron energy represents the element that they break from.

The hole which is created by the stimulation of core electrons from incident X-ray is filled up by an incident electron existing at the outer shell or which comes from valence band. Energy of this transition is balanced with emitting of characteristic X-ray or Auger electron.

Auger electrons and photoelectrons emitting from sample are detected by the help of electron energy analyzer. Thus, density spectrum of photoelectrons and Auger electrons are obtained as a function of kinetic energy. Owing to acquired spectrum elemental analysis, chemical stoichiometry and chemical bonds of the sample can be identified.

In XPS technique, spectrums are saved by making two different surveys. These can be identified as the Survey Spectrum and the high resolution XPS spectrum. Survey Spectrum is carried out generally at energy ranges between (-5)-1100 eV for Mg-K_α and (-5)-1300 eV for Al- K_α depending on used X-ray source in steps of 1 eV. Because electron distribution of each element in core orbits is characteristic, a characteristic peak distribution can be acquired in XPS measurements. So, elemental composition (except hydrogen and helium, because they are so small) can be identified until 100 Å by the help of XPS graphics.

High resolution XPS spectrum is made in steps of 0.1 eV to main core peaks of elements identified from extensive survey. Concentration of elements (chemical stoichiometry) identified from extensive survey is determined by fitting of high resolution spectra taken from main core peaks of elements. Area under main core peaks are measured by the fitting operation and it is divided by Atomic Sensitivity Factor (ASF) which takes characteristic values depending on the angle between analyzer and X-ray source for each element. Proportion of found values is measured and chemical stoichiometry is identified.

Result of fit operation made for high resolution spectra, binding energies of peak/peaks located under main core peak and chemical bond/bonds in sample are identified. Slipping (comparing with binding energy of pure state) which takes place in binding energy may happen as a result of the atom making a chemical bond or its oxidization.

6. EXPERIMENTAL STUDY

Experimental section was studied at Nanotechnology Research Center in Gebze Institute of Technology. At this section Magnetron Sputtering was used for deposition and X-Ray Photoelectron Spectroscopy (XPS), X-Ray Diffraction (XRD), Atomic Force Microscopy (AFM) and Scanning Electron Microscopy (SEM) were used for characterization. On the other hand, Raman Spectroscopy was used and these measurements were done in Sabancı University Nanotechnology Research and Application Center.

Magnetron sputtering and XPS integrated system which were used during this study is shown in Figure 6.1. The integrated system which is composed of sample loading, magnetron sputtering and surface analysis chambers are seen in this figure. This system has high vacuum ($<10^{-10}$ mbar) and connects with ion pump and turbomolecular pump.

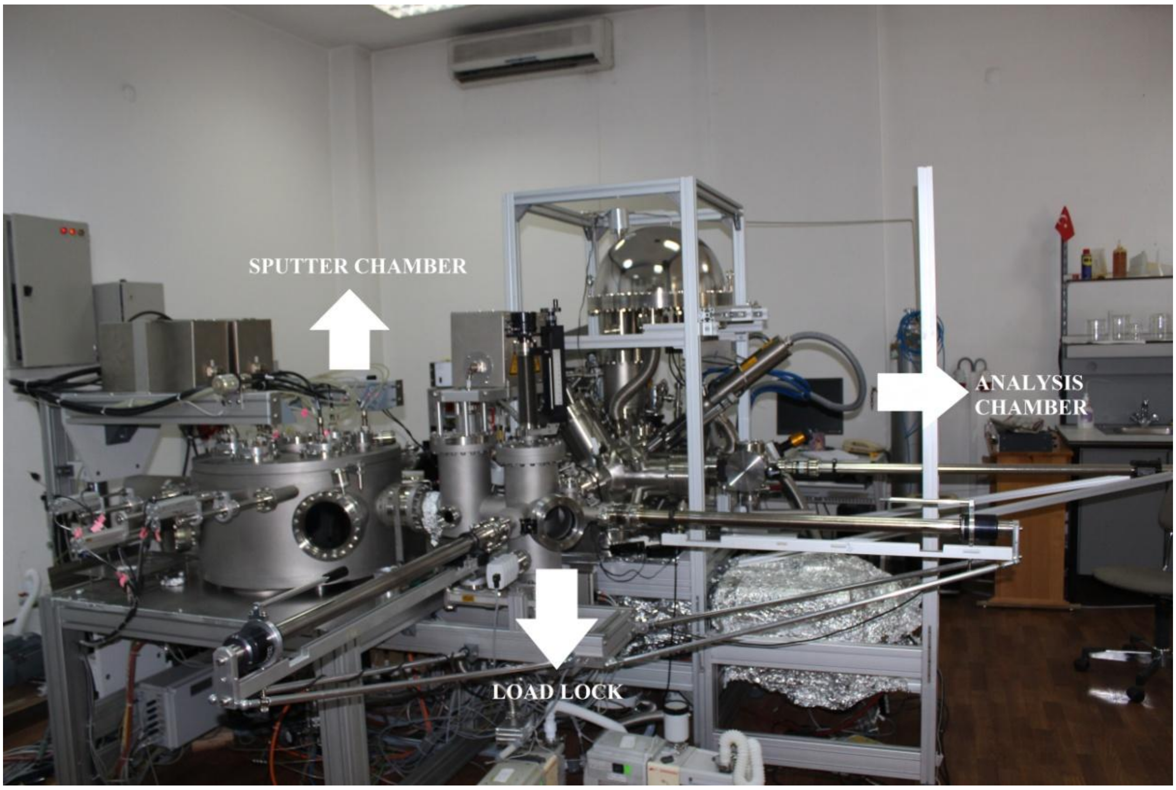

Figure 6.1 : Magnetron Sputtering and XPS integrated system.

6.1. Thin Film Deposition by Magnetron Sputtering

6.1.1. Deposition of Amorphous Silicon by DC Power Supply

It is the first part of the study. In this part, amorphous silicon was deposited with DC power supply and characterized.

Deposition rate is a very important parameter for the process and it is determined by thickness calibration. For obtaining a reliable deposition rate, the thickness value which is obtained from QCM and the thickness value which is got from XPS must cohere with each other. If the value read from QCM is confirmed by the value read from XPS, QCM will continue to be used.

In this work, (111) oriented native oxidized silicon substrate was used as substrate and because depositing material was silicon too, it was decided that it needs a buffer region between these. Titanium was decided to be the buffer, since titanium sticks silicon splendidly. Titanium was deposited on each sample before silicon deposition with 150 Å thickness.

At first, deposition process was done in four series by using 1 Watt, 4 Watt, 10 Watt and 15 Watt power and argon flow rate was 2.7 sccm for each power value. After getting characterization results, observations were done at 1 Watt and at 15 Watt and at lowest-highest argon flow rates. Then, an extra deposition was done on glass substrate to confirm crystallinity. Since glass is amorphous, there is not any peak that overlaps on silicon peaks in XRD pattern.

Depositions were carried out periodically and for every time intervals, XPS spectrum was taken separately. As a result of obtained XPS datas, deposition rates were calculated for each power value by using the formula which is shown under.

$$I = I_o.e^{-(d/\lambda)} \qquad \text{(Eq. 6.1)}$$

Deposition rates were calculated by this formula, but there was a huge difference between the values of QCM and XPS. This is because of plasma shape which was different from ordinary shape. Because the number of atoms which left from target and fell on substrate surface as a result of bombardment was more than the number of atoms which fell on QCM.

After calculating deposition rate, all the samples were deposited until 300 Å thickness achieved. After these, for determining of homogeneity of coating XPS spectrum analysis was carried out on surface of the samples with certain distance interval. So, it was identified that all coatings were homogenous.

6.1.1.1. Deposition of Substrate with Titanium

In the first step, calibration process which is needed for determining of deposition rate and deposition process were carried out together. The deposition rate is calculated as 0.0058 Å/s. Titanium deposition was made on native oxidized single crystalline silicon (Float Zone, (111)). For depositing titanium, substrate was located in the chamber which had ~$2x10^{-8}$ mbar base pressure and sent under the titanium target. The distance between substrate and target was adjusted to 70 mm. Pulsed DC power source which was connected to the titanium target was adjusted to 5 V and argon flow rate was adjusted to 2.7 sccm. Temperature was 18 ^{o}C. All the samples were deposited with titanium 150 Å thick. These settings were the same for all the samples. After deposition procedure, XPS analysis was carried out.

6.1.1.2. Deposition of Amorphous Silicon

Samples which were deposited with titanium were entered the vacuumed chamber separately for depositing at 1 Watt, 4 Watt, 10 Watt and 15 Watt. Base pressure was ~$2x10^{-8}$ mbar. The distance between target and substrate was adjusted to 70 mm. Temperature was 18 ^{o}C. Samples were deposited at fixed time intervals and after all deposition procedure, XPS analysis was carried out for understanding whether substrate is deposited or not.

Deposition rates were calculated by the help of XPS analysis. All parameters that used in deposition procedures and results are shown in Table 6.1.

Table 6.1 Deposition conditions of films which were prepared with different power values.

Power (Watt)	Time (sec)	Argon Flow Rate (sccm)	Thickness (Å)
1	600	2.7	12
4	150	2.7	22.5
10	60	2.7	23.4
15	40	2.7	28

In the aspect of such informations, deposition rates were calculated for all samples by Eq. 6.1. The calculated values are shown in Table 6.2.

Table 6.2 Calculated deposition rates for all samples.

Power (Watt)	Deposition Rate (Å/s)
1	0.02
4	0.15
10	0.39
15	0.706

According to calculated values, it is clearly seen that while power increases, deposition rate increases. Because when power is increased, argon gases accelerate and they bombard the surface of target faster. So the number of atoms broken from target surface increase and substrate is deposited faster.

After this calculation step, deposition was continued until reaching 300 Å thick for every sample. The times needed for reaching 300 Å thicknesses are shown in Table 6.3.

Table 6.3 Total time required for deposition.

Power (Watt)	Time (sec)
1	15000
4	2000
10	769
15	425

After depositions, characterizations were done. In the view of such informations, it was decided that for lowest and highest power values used before, depositions were done at lowest and highest argon flow rates that plasma can be formed. Then 1 Watt and 15 Watt were chosen. The lowest argon flow rates were determined according to the lowest values that plasma can be generated. The lowest and the highest power and argon flow rates are shown in Table 6.4.

Table 6.4 The lowest and the highest power and argon flow rates.

Power (Watt)	The Lowest Argon Flow Rate (sccm)	The Highest Argon Flow Rate (sccm)
1	2	20
15	0.8	20

So the deposition rates were calculated and samples were deposited until thickness reached 300 Å. The deposition rates and total time required for obtaining 300 Å thicknesses are shown in Table 6.5.

Table 6.5 Calculated deposition rates and deposition time for the lowest and the highest power and argon flow rate.

	1 Watt-2 sccm	1 Watt-20 sccm	15 Watt-0.8 sccm	15 Watt-20 sccm
Deposition Rate (Å/s)	0.02	0.009	0.49	0.26
Deposition Time (sec)	15000	33334	612	1154

For the proof of amorphousity of thin films, deposition was done on lamellae glass substrate in similar cases. The parameters are shown in Table 6.6.

Table 6.6 Deposition on glass.

Substrate	Power (W)	Argon Flow Rate (sccm)	Temperature (^{o}C)
Glass	15	2.7	18

For comparison with silicon coated substrates, a single crystalline substrate was also deposited with titanium with 150 Å thickness. The deposition parameters are shown in Table 6.7.

Table 6.7 Parameters of deposition of titanium.

Substrate	Volt (V)	Argon Flow Rate (sccm)	Temperature
Single crystalline silicon	5	2.7	18

6.1.2. Deposition of Amorphous Silicon by RF Power Supply

At this section two targets were used. One of them is powder target and the other one is single crystalline silicon substrate. Both of them are connected to RF power supply.

6.1.2.1. Depositions by Powder Target

At first, depositions were done with powder target. Substrates were (111) oriented single crystalline silicon. Samples were deposited at 10 Watt and 15 Watt. In addition, a sample was deposited at 150 Watt to observe coating at higher power values. Like done in DC power, all samples were deposited with titanium before coating with silicon. The thickness of titanium thin film is 150 Å and silicon thin film thickness is 300 Å for every samples. Deposition rates for every power values were calculated. Because plasma of RF did not behave like DC plasma, deposition rate which was shown by QCM was compatible with the deposition rate calculated from XPS. Parameters are shown in Table 6.8.

Table 6.8 Parameters of deposition of samples with powder target.

Power (Watt)	Argon Flow Rate (sccm)	Deposition Rate (Å/s)	Time (sec)	Temperature (^{o}C)
10	2.7	0.046	6522	18
15	2.7	0.096	3125	18
150	2.7	3.7	81	18

It can be understood from the calculation why the deposition rate of RF power is slower than DC power.

6.1.2.2. Depositions by Substrate Target

After depositing substrates with powder target, single crystalline substrate was started to be used as target. Substrates were again (111) oriented single crystalline silicon. Samples were deposited at 10 Watt and 15 Watt. Again all samples were deposited with titanium before coating with silicon. The thickness of titanium thin film is 150 Å and silicon thin film thickness is 300 Å for every samples. Deposition rates for every power values were calculated. Parameters are shown in Table 6.9.

Table 6.9 Parameters of deposition of samples with substrate target.

Power (Watt)	Argon Flow Rate (sccm)	Deposition Rate (Å/s)	Time (sec)	Temperature (^{o}C)
10	2.7	0.029	10345	18
15	2.7	0.055	5455	18
150	2.7	2.6	115	18

If a comparison is done, the deposition rate of substrate target is slower that powder target. It can be because of the structure of powder target that it was not sintered when it was prepared. So atoms are broken easily from surface of powder target.

6.1.3. Formation of Nanocrystalline Silicon

After deposition of amorphous silicon by different power sources and targets, nanocrystallization process was started. At that time, quartz was also used besides native oxidized single crystalline silicon substrate, because quartz is amorphous. So crystalline silicon peaks in Raman Spectroscopy analysis does not overlap. The second reason for using quartz is that it has high melting temperature.

Depositions were done by RF power and with substrate target and powder target. At this time titanium was not used, because deposited silicon and titanium interact with each other with the effect of increasing temperature. All samples were deposited at 15 Watt power and 2.7 sccm argon with 300 Å thickness. They were annealed at 800 °C temperature for 1 hour. The parameters of this deposition are shown in Table 6.10.

Quartz and silicon substrates were deposited simultaneously. Quartz substrates were deposited for Raman Spectroscopy characterization and single crystalline silicon substrates were deposited for XPS, X-Ray Diffraction and AFM characterizations of thin films.

Table 6.10 Deposition parameters of annealed substrates.

Substrate	Power (Watt)	Argon Flow Rate (sccm)	Target	Annealing Temperature (°C)
Quartz&Silicon	15	2.7	Powder Silicon	800
Quartz&Silicon	15	2.7	Substrate Silicon	800

6.2. Characterization of Thin Films

6.2.1. X-Ray Photoelectron Spectroscopy (XPS) Analysis

Surface analysis of samples was made at vacuum room of system as seen in Fig. 6.2. For identifying elemental analysis, chemical stoichiometry and bonds of samples prepared by Magnetron Sputtering, XPS analysis was made. Main components in XPS are shown in Fig 6.2. The appearance of sample in XPS chamber is shown in Fig. 6.3.

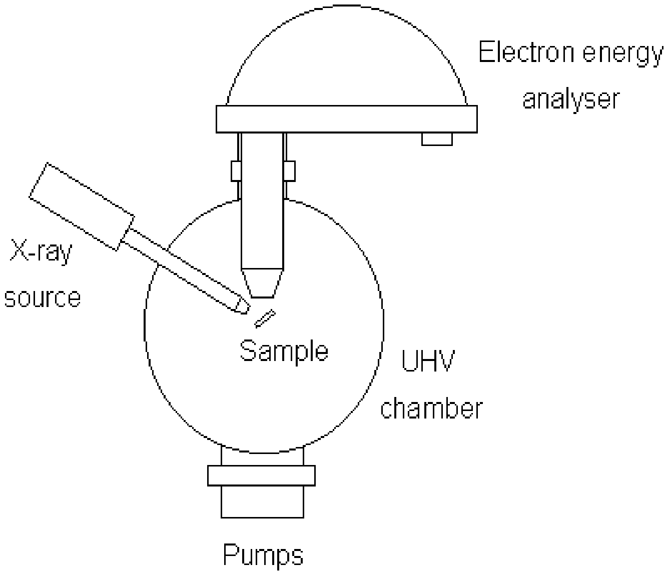

Fig. 6.2. The main components of XPS.

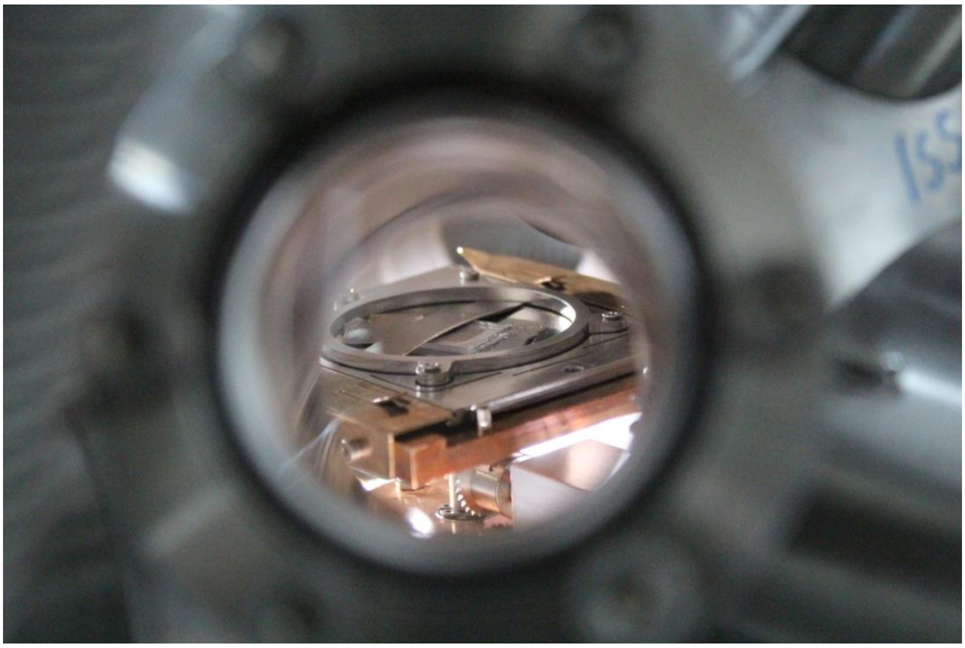

Fig. 6.3. The appearance of sample in XPS analysis chamber.

During the study, as X-Ray source Al K_α (15 kV, 20 mA) with 300 W is used. Kinetic energies of photoelectrons emitted from film surface was analysed by an electron energy analyzer, SPECS GmbH PHOIBOS 150. XPS spectrums were carried out in two ways which are survey spectrum and extensive survey.

6.2.2. Raman Spectroscopy Analysis

For finding out of crystallinity or amorphousity of thin films, Raman Spectroscopy characterization was made. The characterizations were done at Sabancı University Nanotechnology Research and Application Center. The Raman spectra was obtained using Renishaw inVia Reflex Microscope and Spectrometer equipped with an Ar+ laser beam (532 nm) excitation.

6.2.3. X-Ray Diffraction (XRD) Analysis

In order to investigate structural features, phase analysis and obtain particle size, XRD analysis was carried out. This also gives information orientation. For this study, XRD measurements were carried out at Gebze Institute of Technology, Nanotechnology Research Center, Nanomagnetism and Spintronic Laboratory. Rigaku Smartlab XRD was used. Cu-K_α characteristic radiation (λ=0.154 nm) was used. The angle of incidence was fixed to 0.01 deg and the detector moved with a constant step of 0.01 degree from 3 to 80 degree on the 2ϑ scale.

6.2.4. Atomic Force Microscopy (AFM) Analysis

Atomic Force Microscopy (AFM) is a high resolution surface scanning microscopy is used to investigate the morphology of surfaces. The system consists of a cantilever to which a point probe or scanning tip is attached. For this study, Digital Instrument Veeco Nanoscope IV AFM device, which is at Gebze Institute of Technology, Material Science and Engineering, was used in contact mode for measurements. Datas were obtained from scanning of 2µmx2µm, 5µm x 5µm and 10µmx10µm area by using Si_3N_4 tip.

6.2.5. Scanning Electron Microscopy (SEM) Analysis

Scanning Electron Microscopy (SEM) is a high resolution microscopy that used to analyse microstructure of samples. For this study, Philips XL30 SFEG Scanning Electron Microscopy, which is at Gebze Institute of Technology, Material Science and Engineering, was used. In this study images from surface could not be taken, because the resolution of device is inadequate for the thickness of thin films which were 300 Å. But for lateral observation of thin film, cross-sectional images were taken. For this purpose, two samples from each power supply were broken into two pieces by the help of diamond pencil and they sticked to a holder.

7. RESULTS

7.1. X-Ray Photoelectron Spectroscopy

XPS characterizations were done for all samples after depositions. The impurities in thin films were observed in some cases and the proportion of them in thin films was calculated by CASA XPS programme.

At first, substrate which is wanted to be used was characterized by XPS for comparison. After that, because every samples were deposited by titanium before deposition of silicon, titanium deposited samples were characterized by XPS. These XPS images are shown in Figure 7.1 and Figure 7.2.

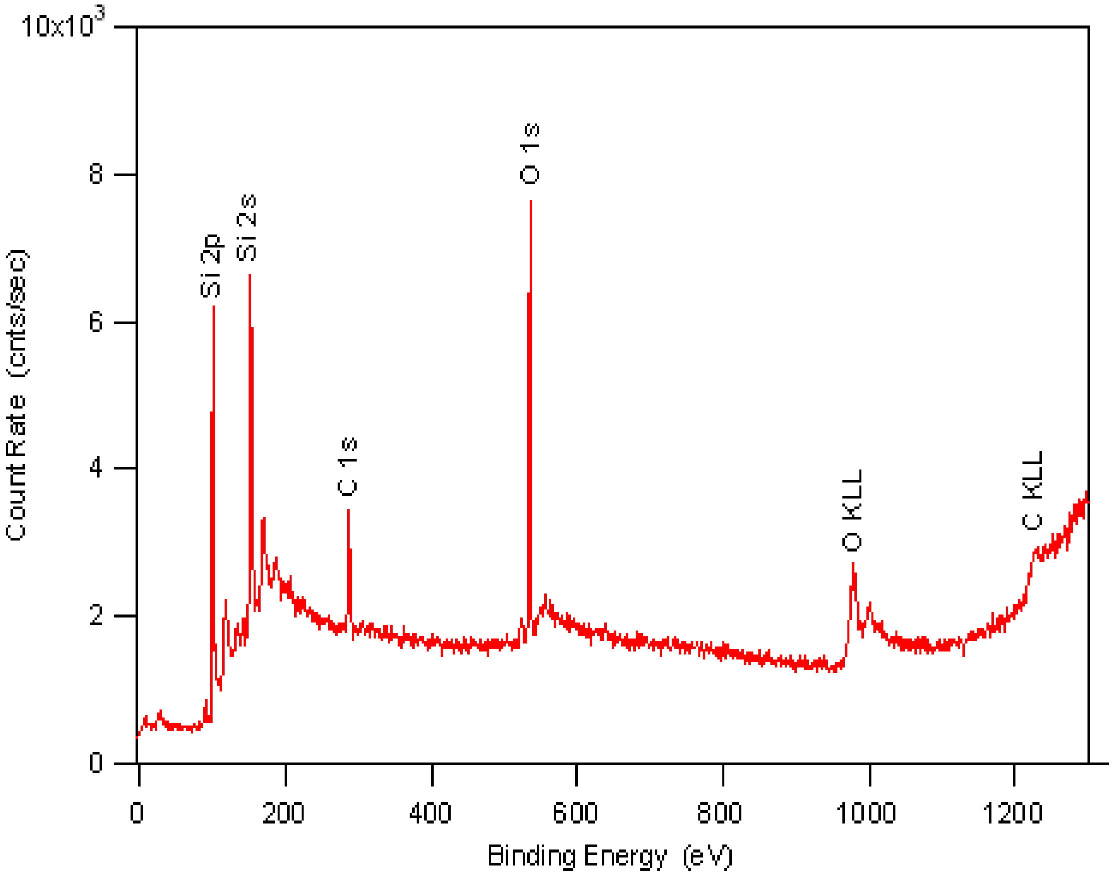

Figure 7.1 : XPS spectrum of native oxidized (111) oriented single crystalline silicon substrate.

As seen from Figure 7.1, silicon, carbon, oxygen and their Auger peaks are found in XPS spectrum of native oxidized single crystalline silicon. Carbon and oxygen are contaminations which are because of keeping substrates in environment, when they were not used. The chemical proportion of native oxidized single crystalline silicon substrate is shown in Table 7.1.

Table 7.1 Chemical proportion of native oxidized single crystalline silicon substrate.

Substrate	Silicon (%)	Oxygen (%)	Carbon (%)
Silicon	53.4	26.7	19.9

From Figure 7.2, titanium deposited silicon surface has titanium and oxygen. The reason of being oxygen at surface is due to oxidation of titanium easily. Even if there is small amount of oxygen in environment, titanium pulls toward oxygen itself. The oxygen content in thin film is 14.3 %.

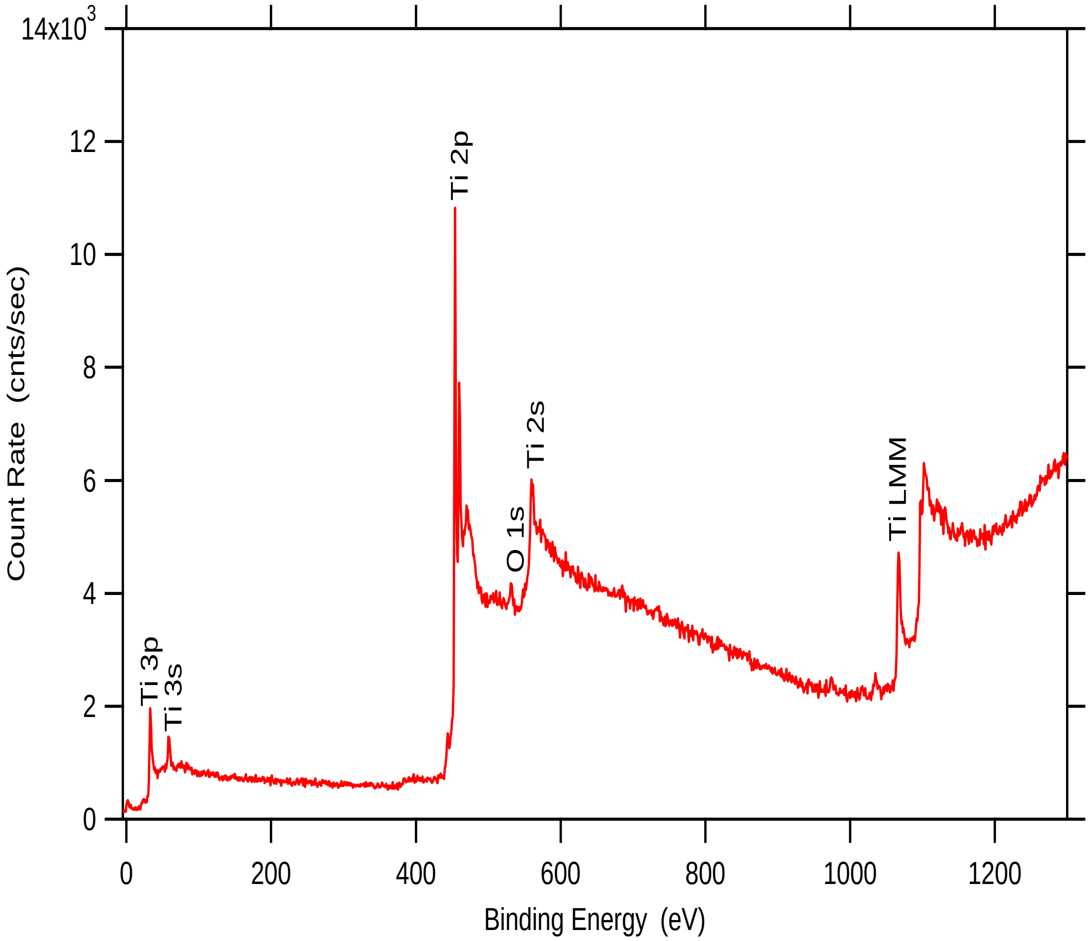

Figure 7.2 : XPS spectrum of titanium deposited silicon substrate.

7.1.1. Deposition of Thin Films by DC Power

7.1.1.1. Study of 1 Watt, 4 Watt, 10 Watt and 15 Watt

As seen from Figure 7.3, it can be only seen silicon and its Auger peaks in high resolution XPS spectrum of silicon films. Before silicon deposition, titanium deposition was done on silicon substrate. Titanium peaks do not appear in this spectrum. Thus, it can be said that silicon films were formed for all power ranges.

By looking Figure 7.3, it can be said that all the films have not any impurity such as oxygen.

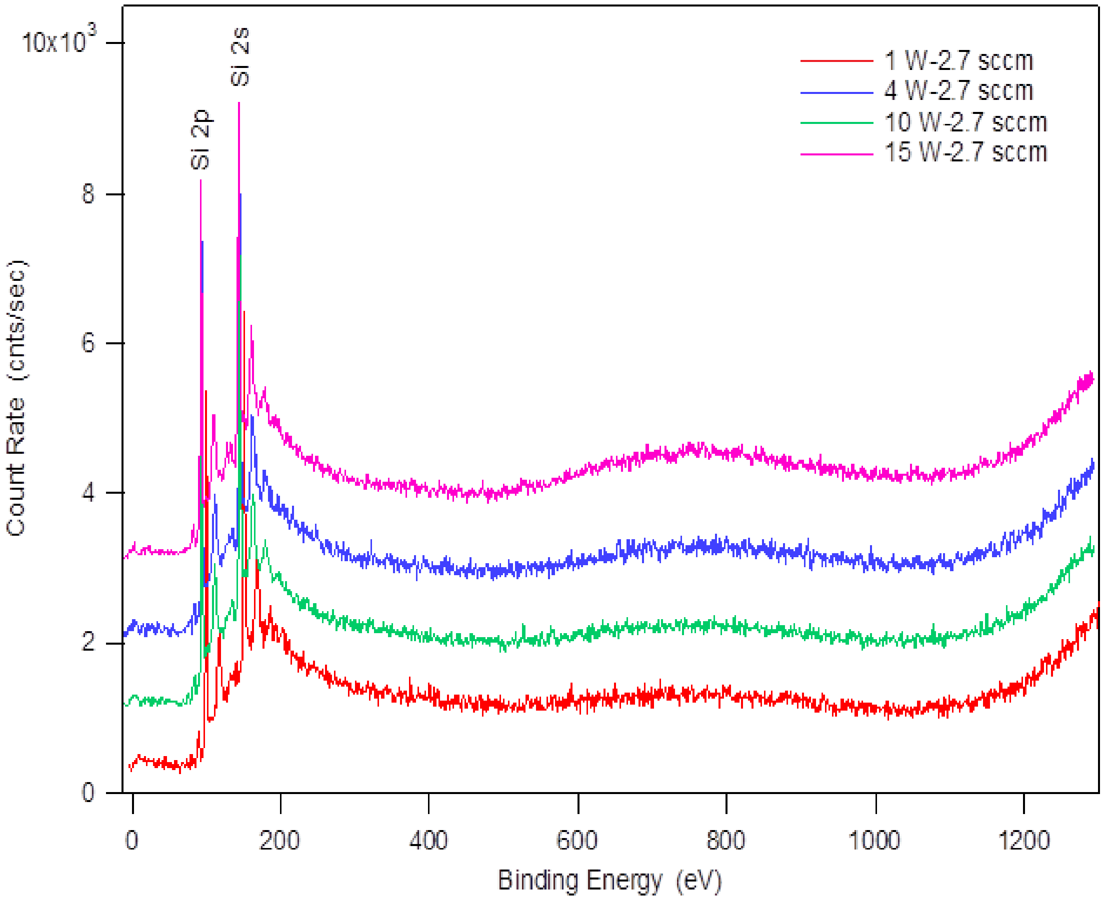

Figure 7.3 : XPS spectrum of samples deposited at 1 W, 4 W, 10 W and 15 W.

7.1.1.2. Study of The Lowest - The Highest Power and Argon Flow Rate

After applying several ranges of power, it was decided that at the lowest and the highest power, which were applied before, the minimum and the maximum argon flow rate were determined. The applied lowest and highest powers were 1 Watt and 15 Watt. In the aspect of such informations, the minimum and the maximum argon flow rates which can form plasma were determined for 1 Watt and 15 Watt. These are 2 sccm and 20 sccm for 1 Watt, 0.8 sccm and 20 sccm for 15 Watt. By the result of these studies, spectrums obtained from XPS are shown in Figure 7.4.

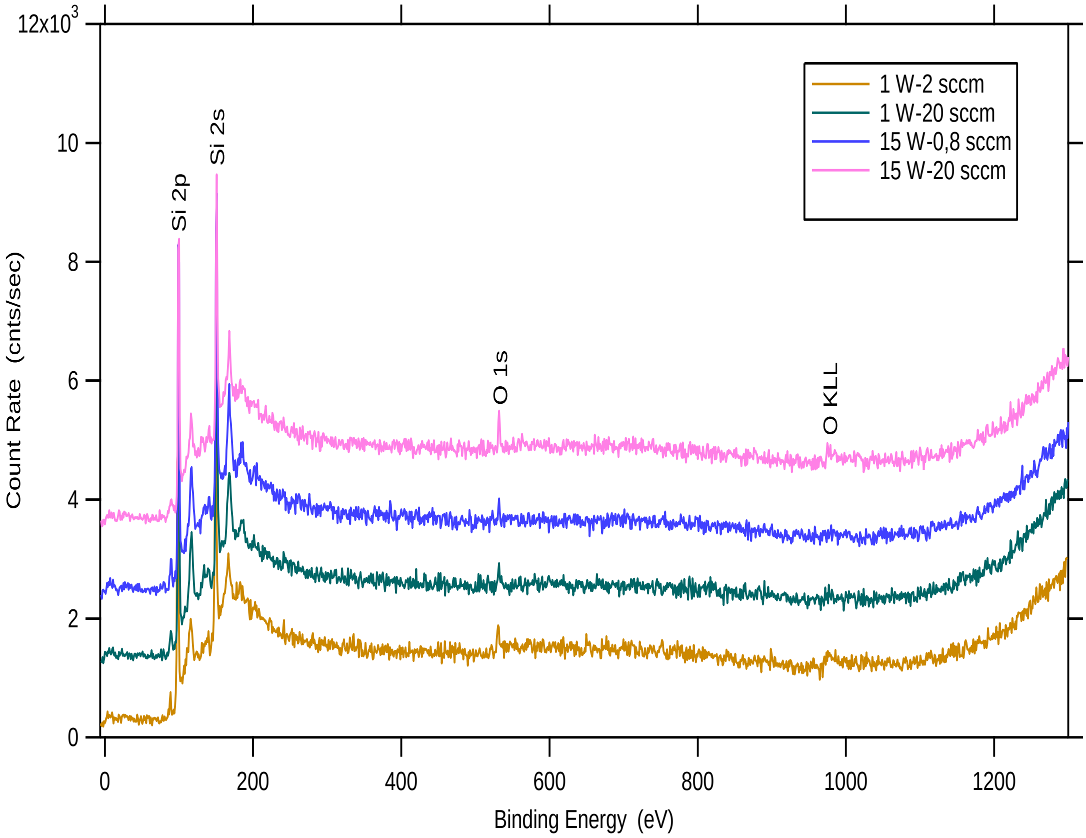

Figure 7.4 : XPS spectrum of silicon deposited sample at 1 Watt & 15 Watt and with lowest and highest argon flow rates.

As seen from Figure 7.4, silicon deposition was done, but oxygen content is observed in all films. The oxygen existence is because of argon line that its filter is out of date. If the calculations are investigated carefully, it can be understood that when argon flow rate increases, oxygen content increases too. The content of oxygen in all films is shown in Table 7.2.

Table 7.2 The chemical proportion of silicon thin films.

Content	1 Watt-2 sccm	1 Watt-20 sccm	15 Watt-0.8 sccm	15 Watt-20 sccm
Silicon (%)	97.3	92.5	97.6	93.8
Oxygen (%)	2.7	7.5	2.4	6.2

7.1.2. Deposition of Thin Films by RF Power

7.1.2.1. Deposition of Thin Films by Powder Target

The XPS results of the depositions done with RF power are shown in Figure 7.5.

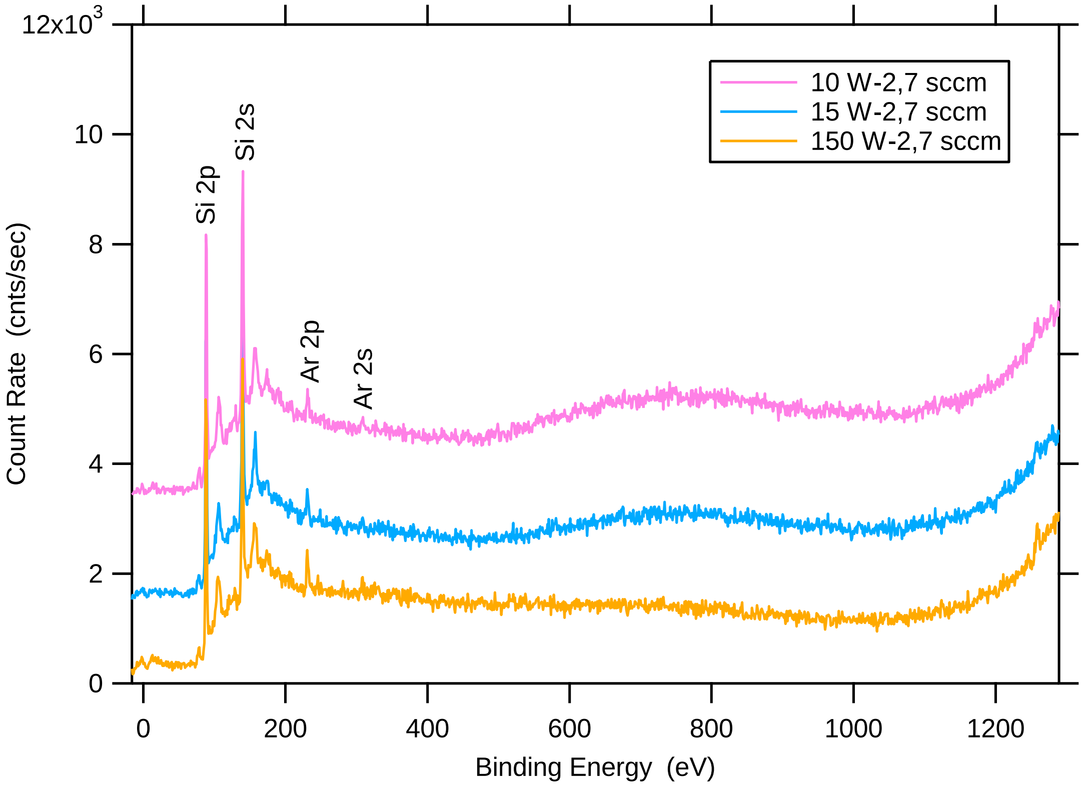

Figure 7.5 : XPS spectrum of silicon deposited sample at 10Watt, 15 Watt, 150 Watt and 2.7 argon flow rate.

As seen from Fig. 7.5, silicon films were obtained. But there can be seen argon main peaks resided in 242 eV. The argon content can be because of RF power. In as much as it was not seen in DC power. The argon content in all films is calculated and it is shown in Table 7.3.

Table 7.3 Argon content in silicon thin films.

Power – Argon Flow Rate	Argon (%)	Silicon (%)
10 Watt-2.7 sccm	4.21	95.79
15 Watt-2.7 sccm	5.24	94.76
150 Watt-2.7 sccm	4.46	95.54

7.1.2.2. Deposition of Thin Films by Substrate Target

As seen from Figure 7.6, silicon films were obtained. But there can be seen argon main peaks resided in 242 eV. The argon content can be because of RF power. On the other hand, oxygen which is not seen in samples deposited by powder target is found in thin films.

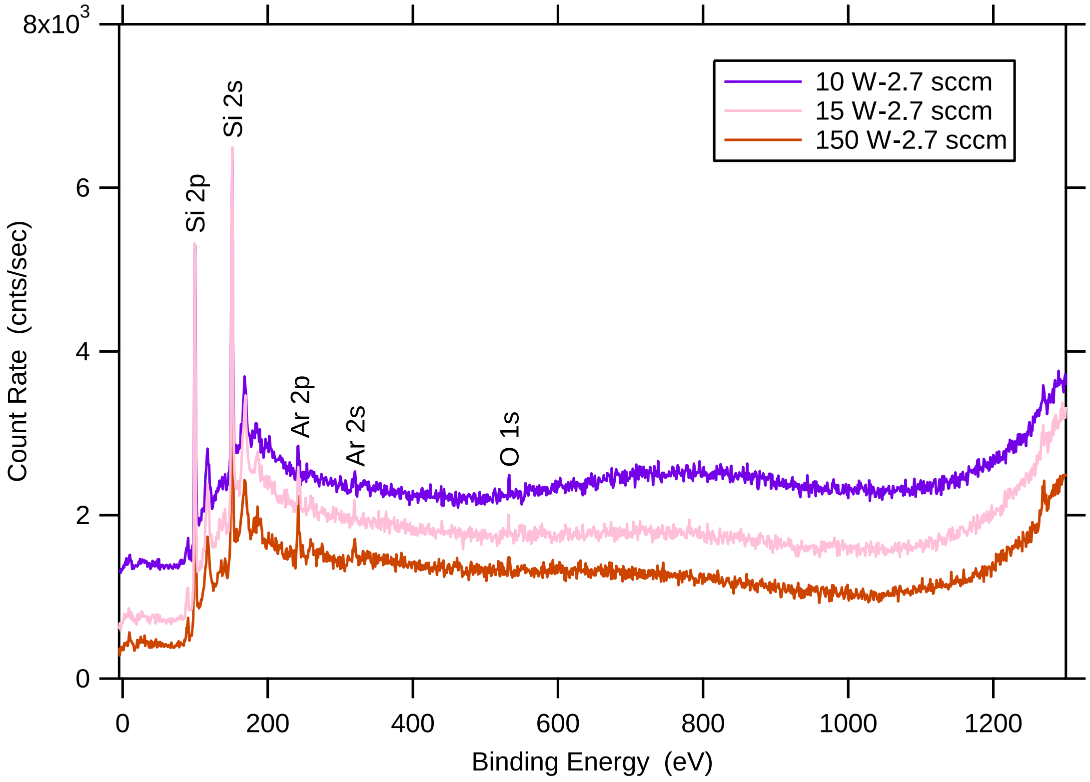

Figure 7.6 : XPS spectrum of silicon deposited sample at 10 Watt, 15 Watt, 150 Watt and 2.7 sccm argon flow rate.

It can be seen from Table 7.4 that when power increases, argon content increases too. It is understood that increase of argon content is related to RF power. Since argon is not seen in samples deposited by DC power.

Table 7.4 Argon and oxygen content of silicon thin films.

Watt - sccm	Argon (%)	Oxygen (%)	Silicon (%)
10 Watt-2.7 sccm	3.53	1.50	94.97
15 Watt-2.7 sccm	4.44	1.94	93.62
150 Watt-2.7 sccm	5.61	1.62	92.70

7.1.3. Annealed Samples

XPS spectrum of samples which were annealed at 800 °C for an hour is shown in Figure 7.7.

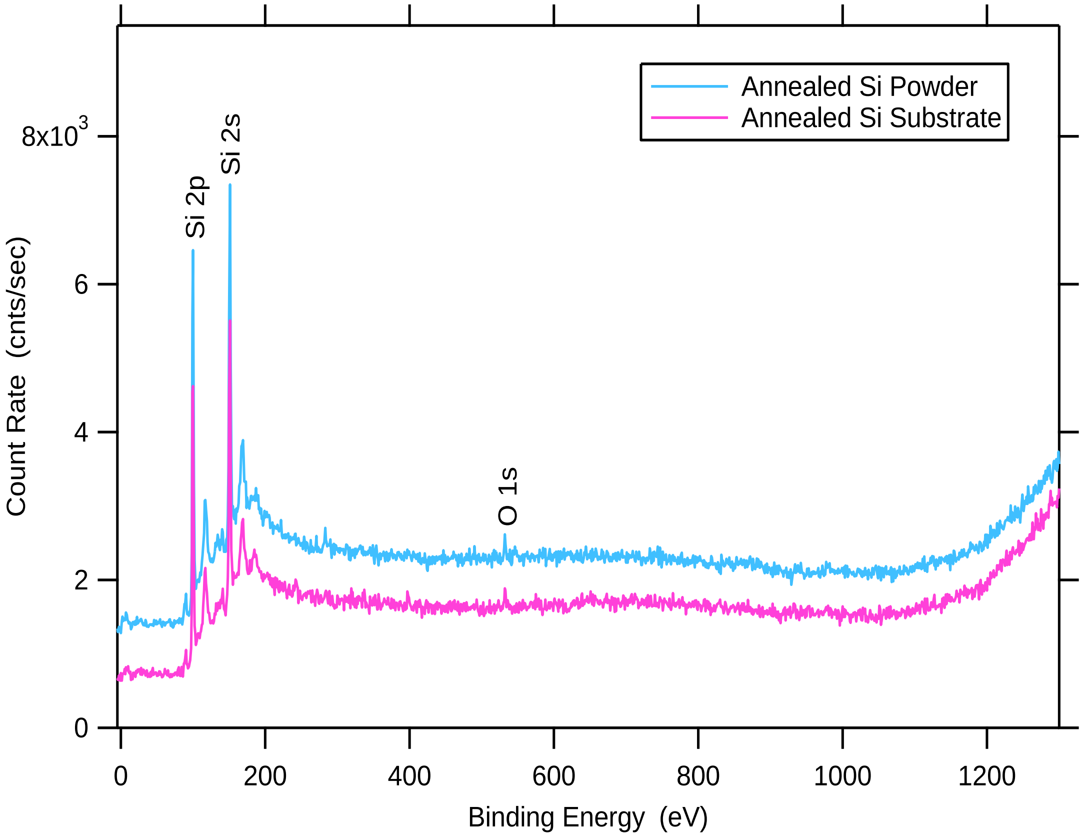

Figure 7.7 : XPS spectrum of annealed samples deposited by powder and substrate target.

As seen from figure, there is small amount of oxygen in thin films. The proportion of oxygen in silicon thin films is shown in Table 7.5.

Table 7.5 The oxygen content in silicon thin films.

Target	Oxygen (%)	Silicon (%)
Powder	2.45	97.55
Substrate	2.77	97.23

As seen from Table 7.5, oxygen content is higher in sample deposited by powder target than sample deposited by substrate target.

7.2. Raman Spectroscopy

Three samples were characterized by Raman Spectroscopy. One of them was deposited by silicon substrate target at 15 Watt and 2.7 sccm with 300 Å. The substrate was native oxidized single crystalline silicon. The Raman spectrum of native oxidized silicon substrate is shown in Figure 7.8.

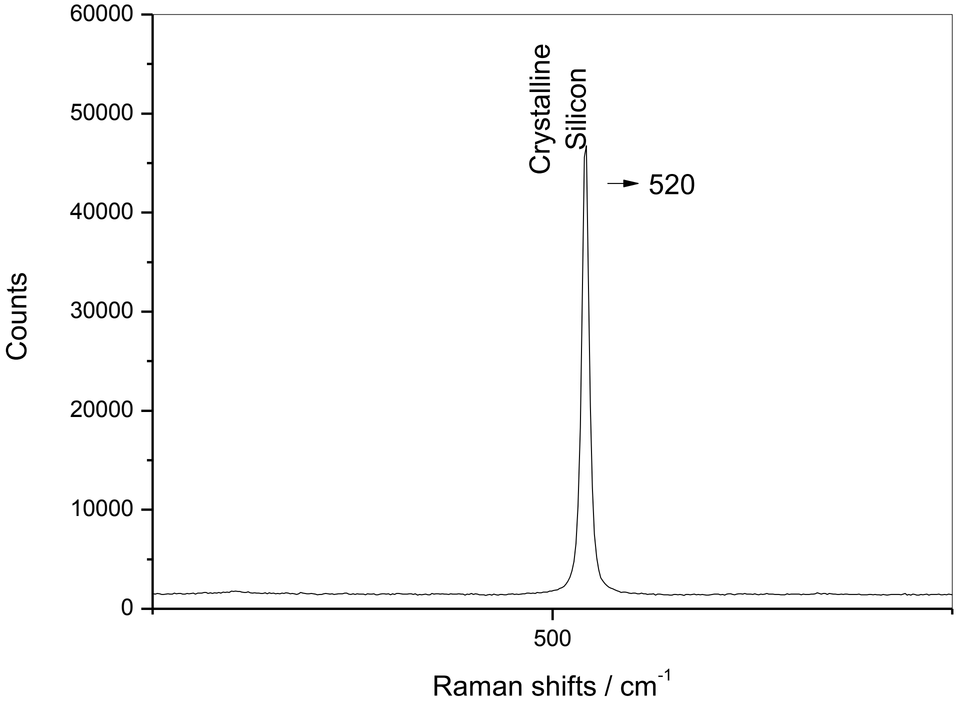

Figure 7.8 : The Raman spectra of native oxidized silicon substrate.

The substrate temperature was 18°C during deposition. Titanium was deposited on silicon substrate with 150 Å thickness before silicon deposition. The Raman spectrum of this sample is shown in Figure 7.9. As seen from this figure, there are two peaks which are resided in 470 cm^{-1} and 520 cm^{-1}. A broad band centred at ~470 cm^{-1} is the typical peak of amorphous silicon and this observation can be related to existence of amorphous silicon in the film [32]. A band peaked at 520 cm^{-1}, which is the characteristic of crystalline silicon, belongs to single crystalline substrate [32, 10].

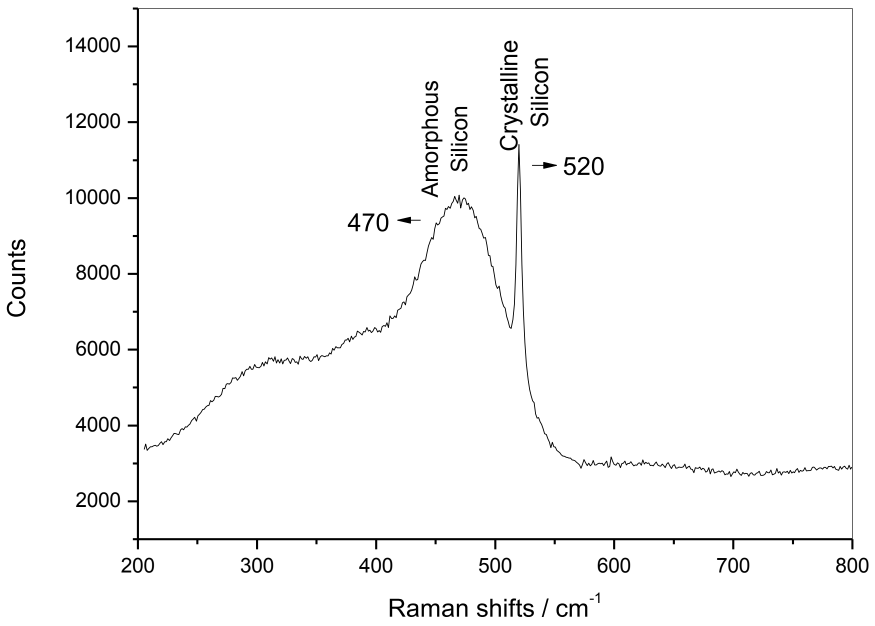

Figure 7.9 : The Raman spectra of the sample deposited by substrate target at 15 Watt and 2.7 sccm argon flow rate.

The other two are annealed samples. Substrates which were used at this time are quartz. This is because it is not desired that any peak comes from substrate. The Raman spectrum of quartz substrate is shown in Figure 7.10.

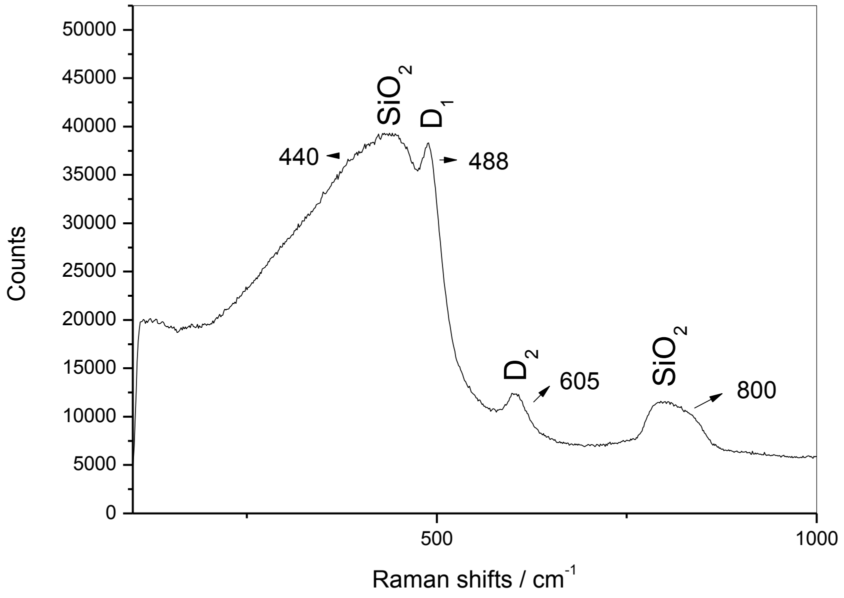

Figure 7.10 : The Raman spectra of quartz substrate.

As seen from Figure 7.10, broad peaks are seen in 440 cm^{-1} and 800 cm^{-1} which are attributed to SiO_2 bonds [34]. And a peak at 488 cm^{-1} belongs to amorphous silicon. The maximum position of the narrow line corresponds to D_1 line and D_2 line resided in 605 cm^{-1} reported in the literature [34, 35]. These lines are assigned to defects in the structure of bulk silica.

One of the quartz samples was deposited by powder target and the other one was deposited by substrate target and each of them was deposited at 15 Watt and 2.7 sccm argon flow rate with 300 Å thickness. Then each of them annealed at 800 °C for 1 hour. They were not deposited with titanium, because high temperature was applied to the samples and at that time titanium and silicon interact with each other. The Raman spectra of annealed samples are shown in Figure 7.11.

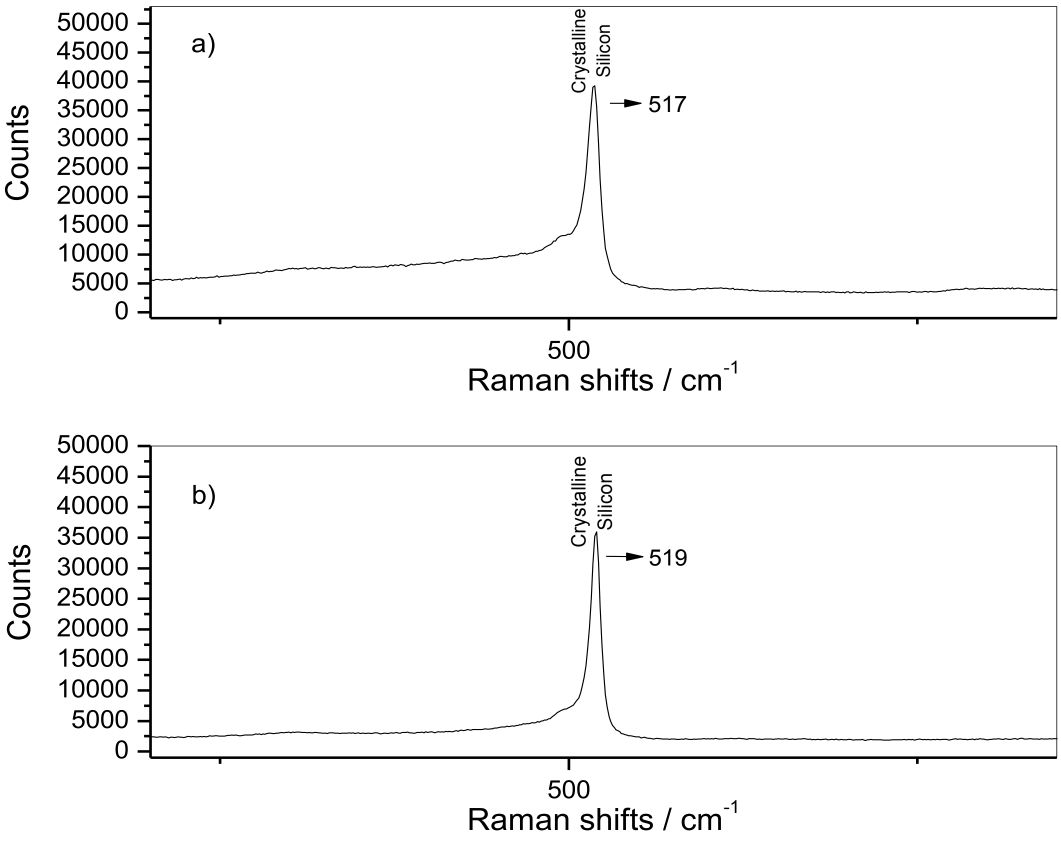

Figure 7.11 : The Raman spectra of the annealed samples deposited by a) powder target b) substrate target at 15 Watt and 2.7 sccm argon flow rate.

As seen from Figure 7.11, bands peaked at 517 cm^{-1} and 519 cm^{-1} which are attributed to the formation of crystalline silicon are observed. In fact, the crystalline silicon peak is observed at 520 cm^{-1}, but depending of annealing temperatures and a slight shift of the 520 cm^{-1} peak towards lower wavenumbers is observed and it is ascribed to crystalline size and/or stress effects in thin films [10, 32, 33].

7.3. Atomic Force Microscopy (AFM)

Before presenting the images which belong to deposited samples, single crystalline silicon substrate and titanium deposited silicon substrate are shown in Figure 7.12.

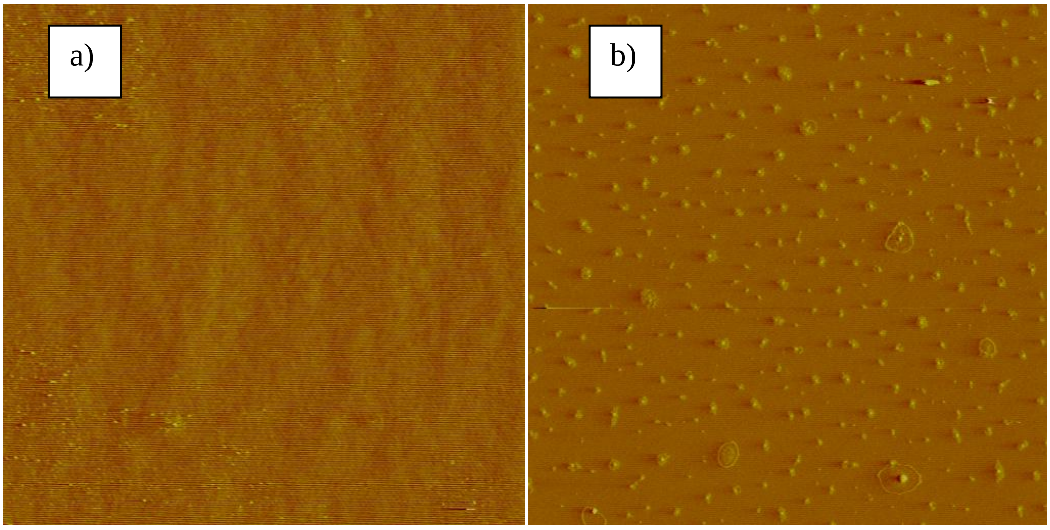

Figure 7.12 : The 10µmx10µm AFM images of samples a) native oxidized single crystalline silicon, b) titanium deposited silicon.

The images shown above represent the single crystalline silicon and titanium deposited silicon which are seen on the Figure 7.12.a and Figure 7.12.b, respectively. In the image belongs to single crystalline silicon, there is some conglomeration which are on the top right and down right of the image that is thought to be oxidized regions of substrate. This can be because silicon was kept in environment, while substrate was not used.

The root mean square (rms) values for single crystalline silicon and titanium deposited silicon substrate are 0.215 nm and 0.693 nm, respectively. Their lateral displays are shown in Figure 7.13 and Figure 7.14.

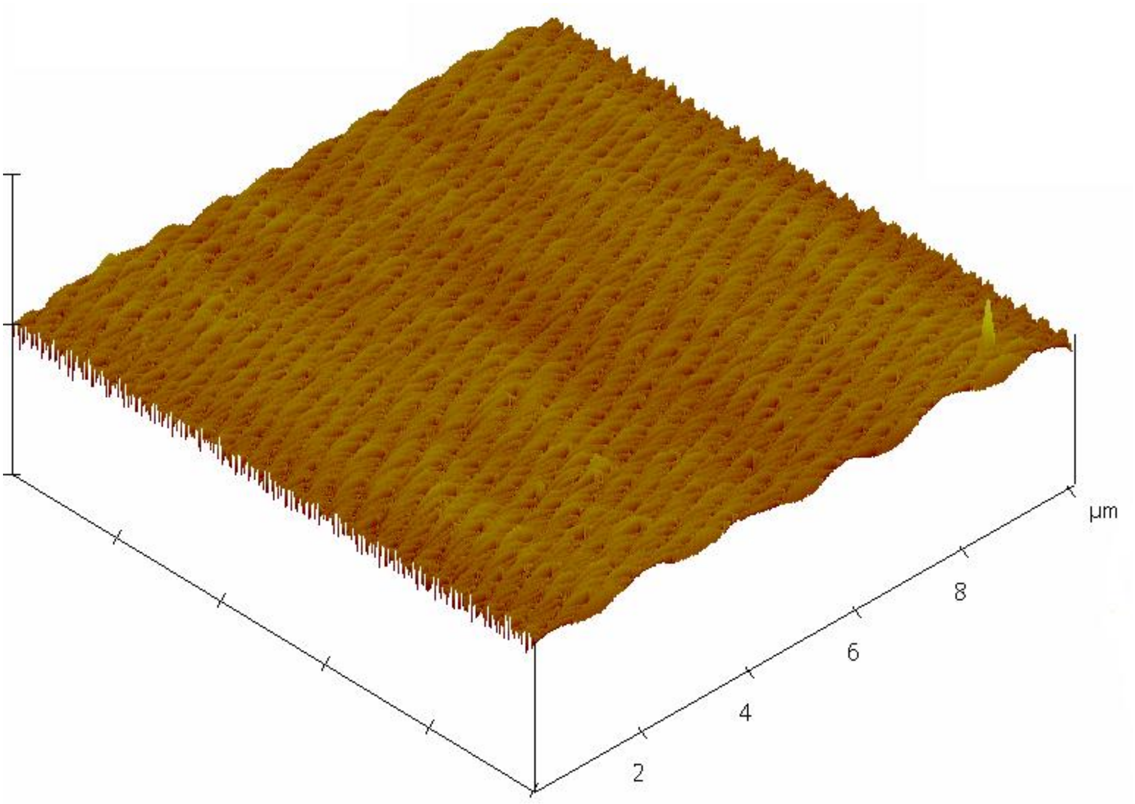

Figure 7.13 : The 10µmx10µm lateral AFM image of native oxidized single crystalline silicon substrate.

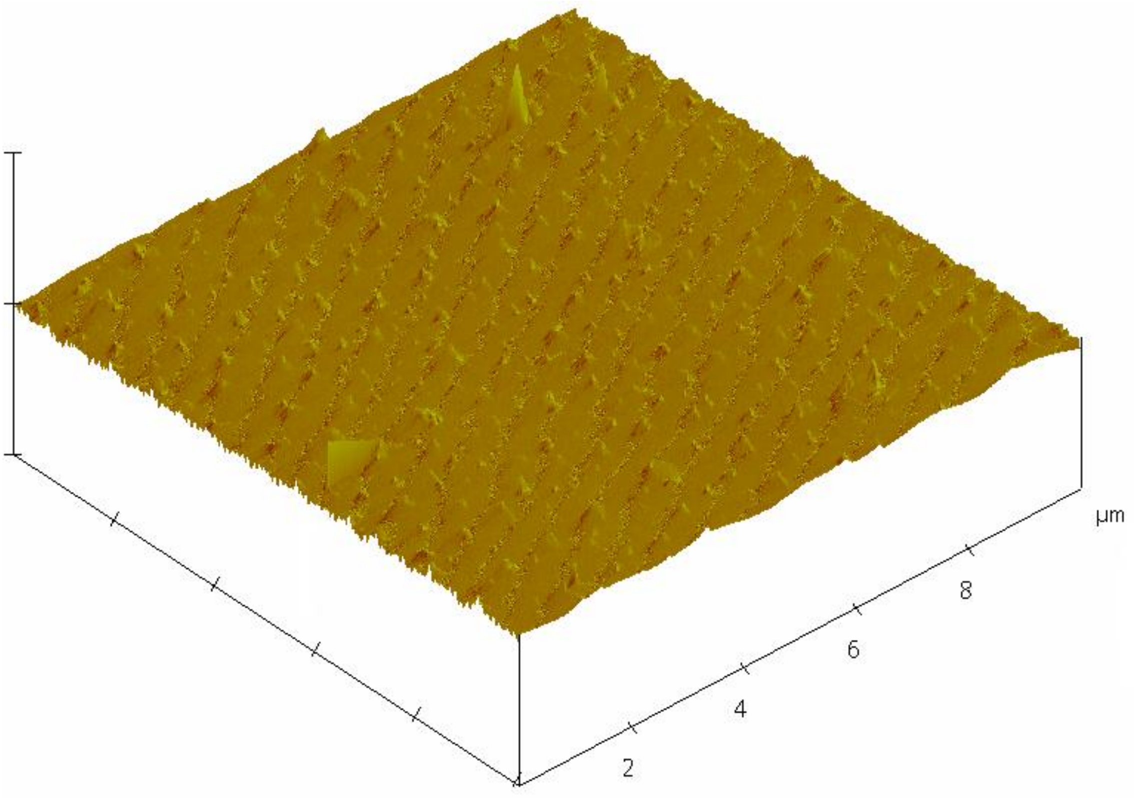

Figure 7.14 : The 10µmx10µm lateral AFM image of titanium deposited silicon substrate.

7.3.1. Deposition by DC Power Supply

7.3.1.1. Study of 1 Watt, 4 Watt, 10 Watt and 15 Watt

Figure 7.15 represents the AFM images of the a-Si:H thin films, which shows a root-mean-square (rms) surface roughness in the range of 0.655-2.082 nm. The surface roughness was measured by atomic force microscopy (AFM) (Digital Instruments Veeco Nanoscope IV system). Contact mode was used in this AFM analysis and it was only made on samples prepared at different power values. The images of depositions at 1 Watt, 4 Watt, 10 Watt and 15 Watt are shown in Figure 7.15.

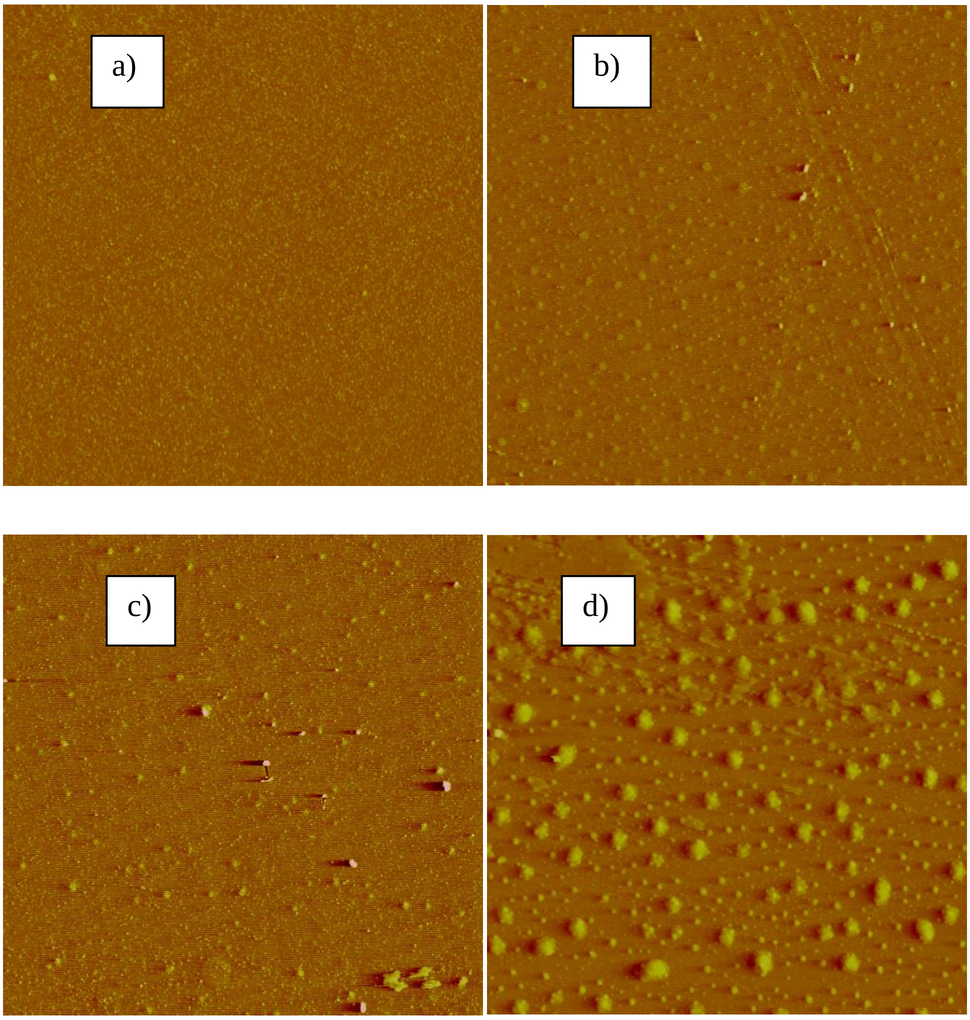

Figure 7.15 : The 10μmx10μm AFM images of the samples a) 1 Watt, b) 4 Watt, c) 10 Watt and d)15 Watt.

From the AFM images obtained, it is obviously seen that the shape of the grains on the surfaces is spherical. It is thought that these spherical grains are coming from target which is formed of silicon powder. This can be because the silicon powder target is not sintered, only pressed. For surely understanding this effect, “Study of the lowest- the highest power and argon flow rate” was done.

On the other hand, it can be seen from images that while power increases, size of particles broken from target increases too. The particles are arranged in an order in all films, in other words it can be said that films are homogeneous. As at lower power values films are smoother, higher power values films become rougher. Frankly speaking, while at 1 Watt the rms is 0.655 nm, at 4 Watt and 10 Watt the rms are 0.552 nm and 0.663 nm, respectively. At 15 Watt, the rms is 2.082 nm. In other words, it can be said that if power increases, film becomes rougher.

After this study, for understanding of behavior of the particles present on the films, it was decided that the minimum and the maximum argon flow rates were determined according to the maximum and the minimum power. By virtue of this study, it can be understood how the particles form.

7.3.1.2. Study of The Lowest - The Highest Power and Argon Flow Rate

During this part of the thesis at first 1 Watt and 15 Watt, which are the lowest and highest power used before, were chosen. The maximum argon flow rate giving to the system is 20 sccm. Then the minimum argon flow rates which can form plasma were determined. The minimum argon flow rates are 0.8 sccm for 15 Watt and 2 sccm for 1 Watt. Images for 1 Watt are shown in Figure 7.16.

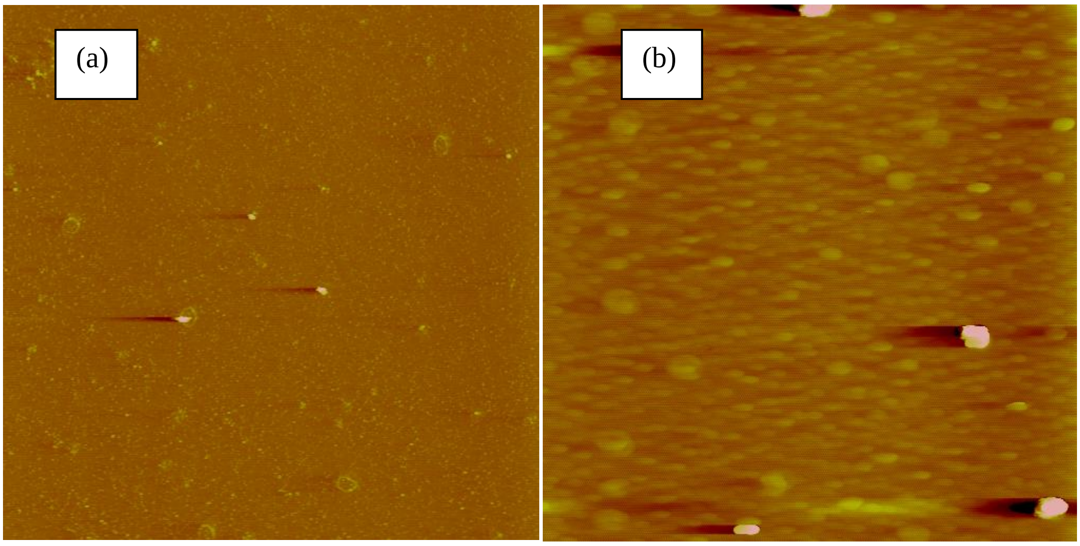

Figure 7.16 : 10μmx10μm AFM images of the samples a) 1 Watt and 2 sccm, b) 1 Watt and 20 sccm.

The images shown in Figure 7.16 demonstrate the films that 1 Watt and 2 sccm on the left and 1 Watt and 20 sccm on the right. It can be inferred from these images that while argon flow rate increases, the size of particles broken from target increases too. The rms value of 2 sccm is 0.727 nm and the rms value of 20 sccm is 1.783 nm. In other words, while argon flow rate increases, film becomes rougher. This is because target is powder and it is not sintered. It is just pressed. So particles tend to leave easily from target surface, when particles with high energy crash to it. When argon flow rate increases, mean free path of argon particles decreases and collisions increase. So particles reaching to substrate increase, too. The lateral images of 1 Watt are shown in Figure 7.17 and Figure 7.18.

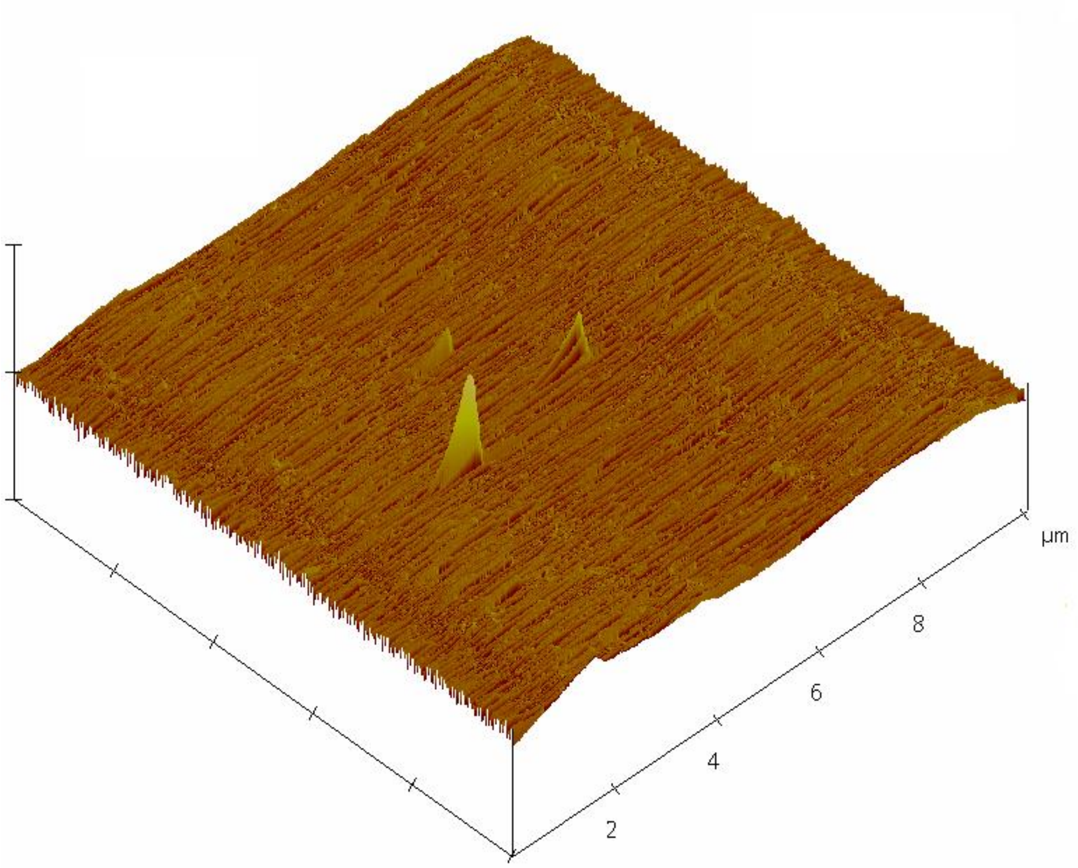

Figure 7.17 : The 10µmx10µm lateral AFM images of the sample deposited at 1 Watt and 2 sccm argon flow rate.

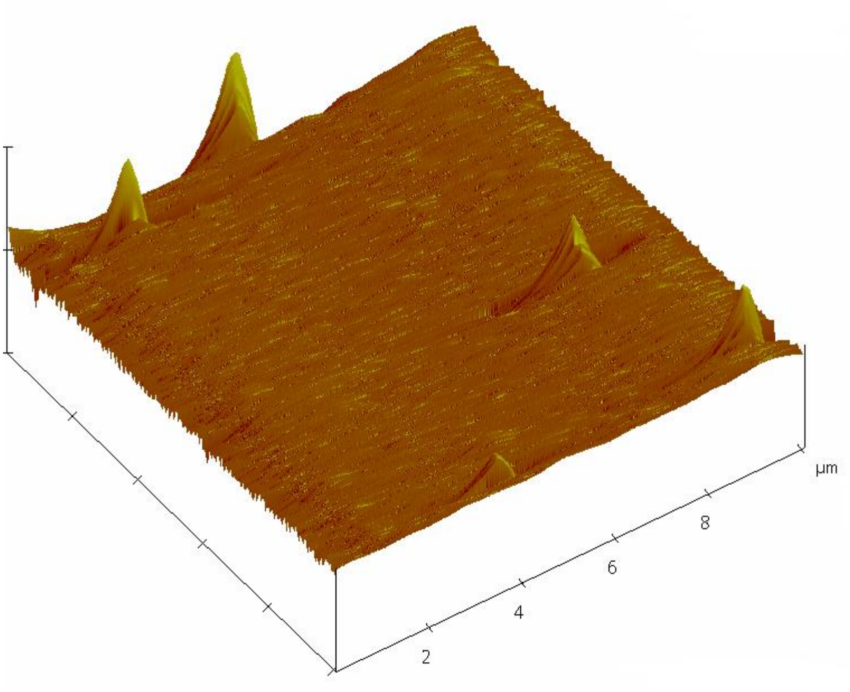

Figure 7.18 : The 10µmx10µm lateral AFM images of the sample deposited at 1 Watt and 20 sccm argon flow rate.

The images of 15 Watt-0.8 sccm and 15 Watt 20 sccm are shown in Figure 7.19.

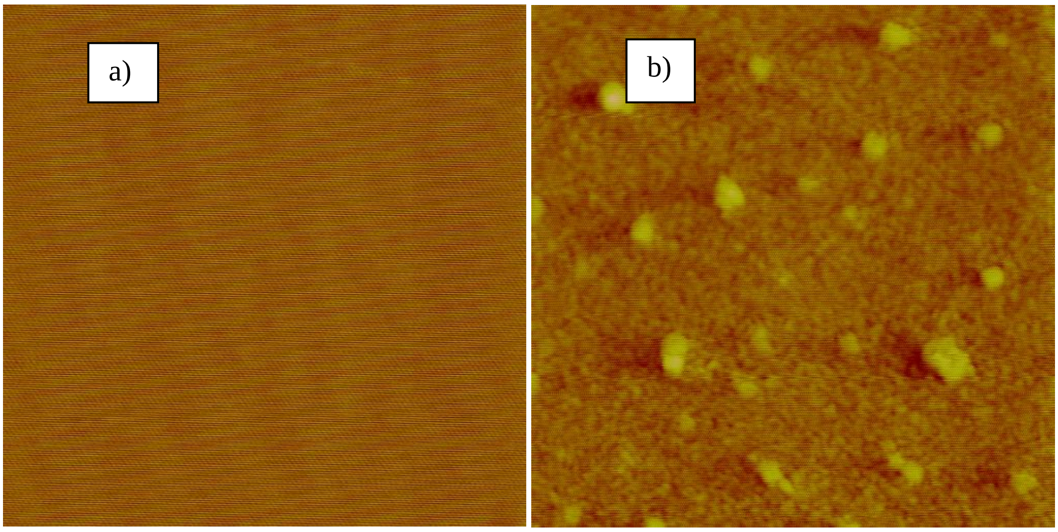

Figure 7.19 : The 2µmx2µm AFM images of the samples a) 15 Watt and 0.8 sccm, b) 15 Watt and 20 sccm argon flow rate.

In Figure 7.19, it is demonstrated that the films deposited at 15 Watt-0.8 sccm which is on the left and 15 Watt-2 sccm which is on the right. It can be inferred from images that, while argon flow rate increases, the film becomes rougher. The rms value of 0.8 sccm is 0.318 nm and the rms value of 20 sccm is 2.039 nm. The lateral images of this set are shown in Figure 7.20 and Figure 7.21.

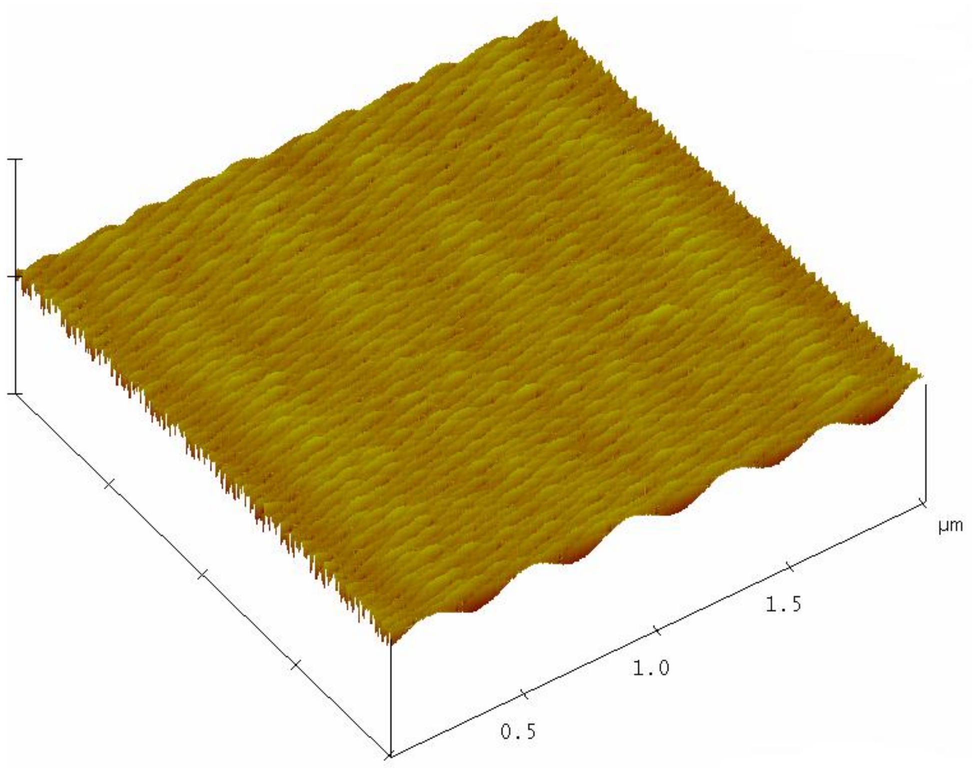

Figure 7.20 : The 10µmx10µm lateral AFM image of sample deposited at 15 Watt and 0.8 sccm argon flow rate.

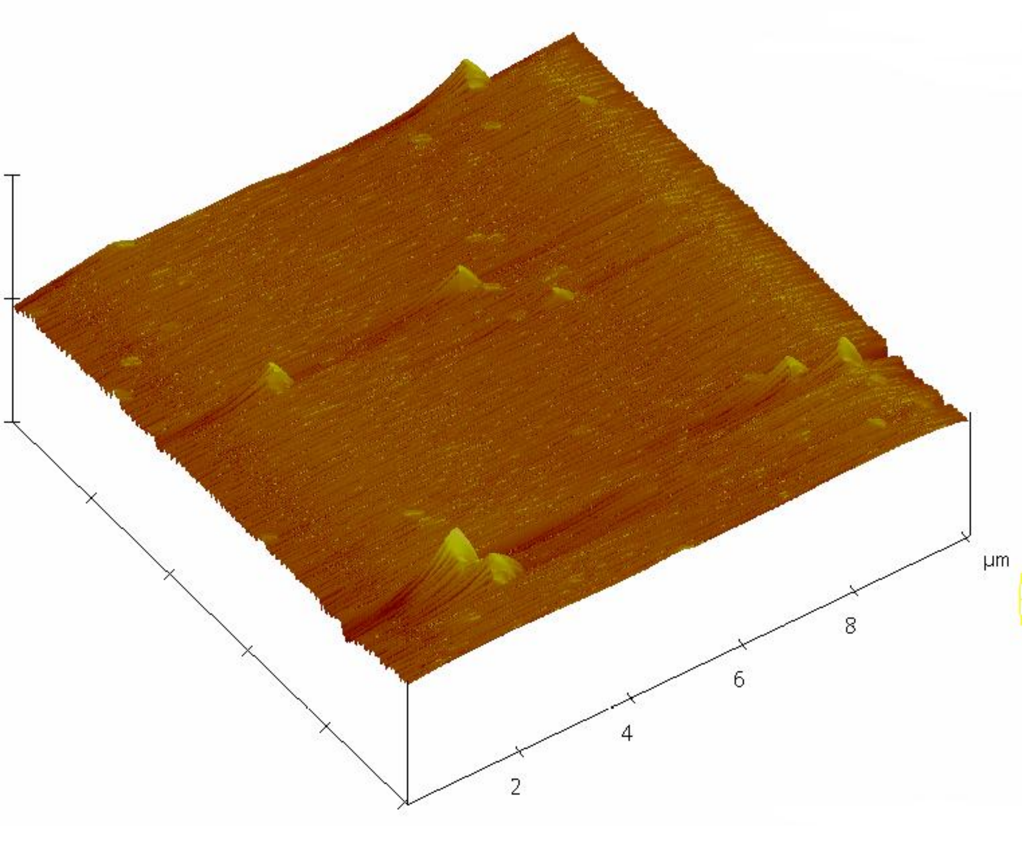

Figure 7.21 : The 10µmx10µm lateral AFM image of sample deposited at 15 Watt and 20 sccm argon flow rate.

As seen from Figure 7.21, the surface of 15 W-0.8 sccm is very smooth. On the other hand, the surface of 15 Watt-20 sccm is rougher.

From all these depositions, it can be said that the cleanest surface is obtained from 15 Watt-0.8 sccm argon flow rate. The dirtiest surface is 15 Watt-20 sccm which is understood from rms values.

In the light of these informations, it is thought that when annealing process starts, the particles on the surface arise from powder target can be turned into an advantage. The fallen particles can be crystallized easily by the help of increasing temperature. It will be shown in further studies.

7.3.2. Deposition by RF Power Supply

7.3.2.1. Deposition by Powder Silicon Target

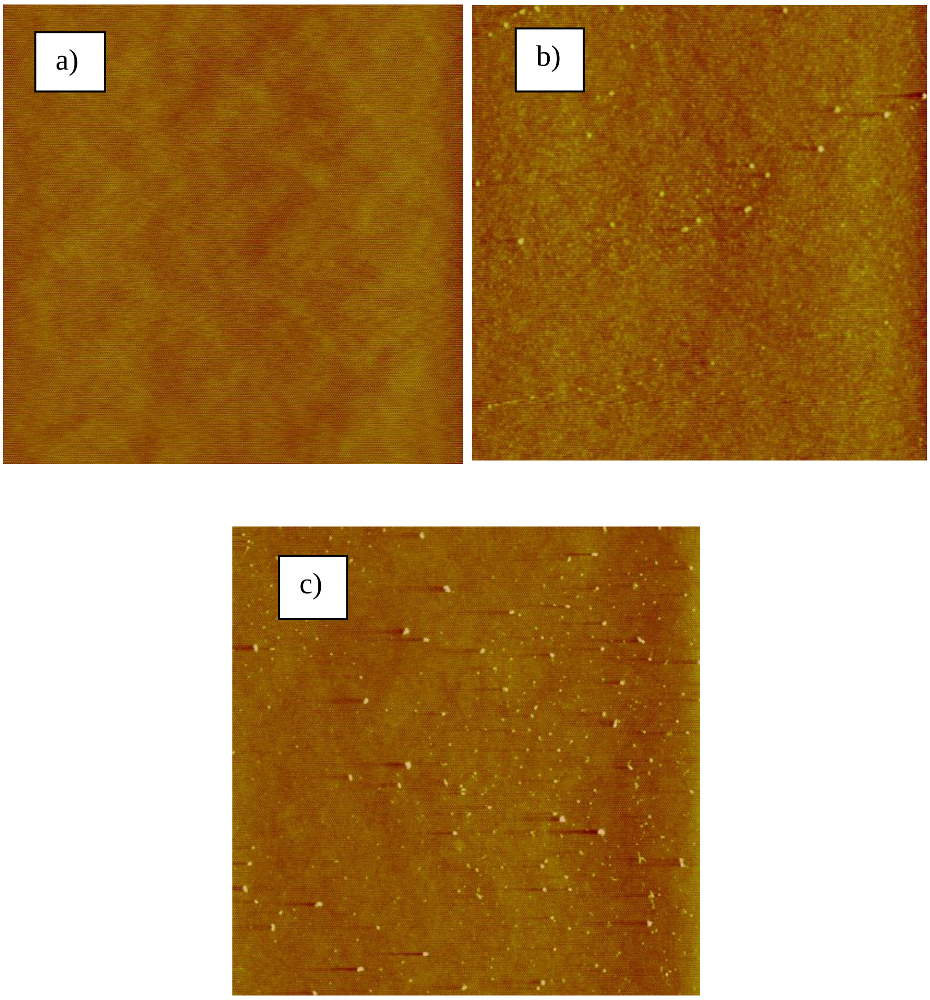

Figure 7.22 : The 10µmx10µm AFM images of samples a) 10 Watt and 2.7 sccm, b) 15 Watt and 2.7 sccm, c) 150 Watt and 2.7 sccm.

It can be understood from Figure 7.22 that while power increases, rms value increase too. The rms values of 10 Watt, 15 Watt and 150 Watt are 0.240 nm, 0.291 nm and 0.396 nm, respectively.

The lateral images of this set are shown in Figure 7.23, Figure 7.24 and Figure 7.25.

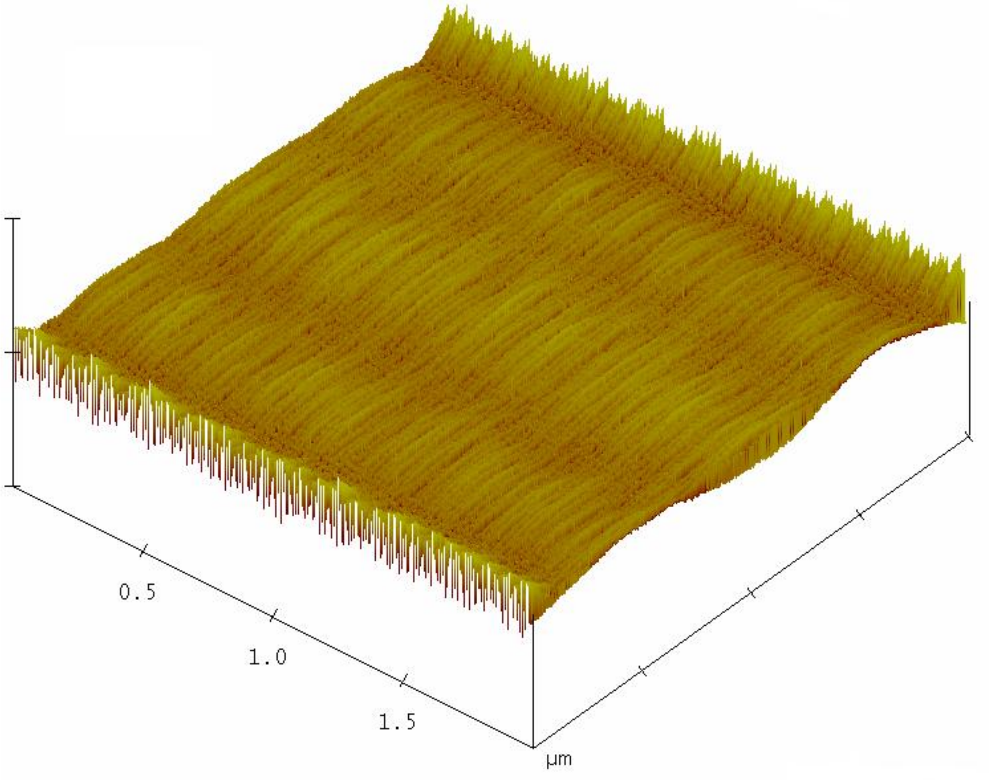

Figure 7.23 : The 2µmx2µm lateral AFM image of sample deposited at 10 Watt and 2.7 sccm argon flow rate.

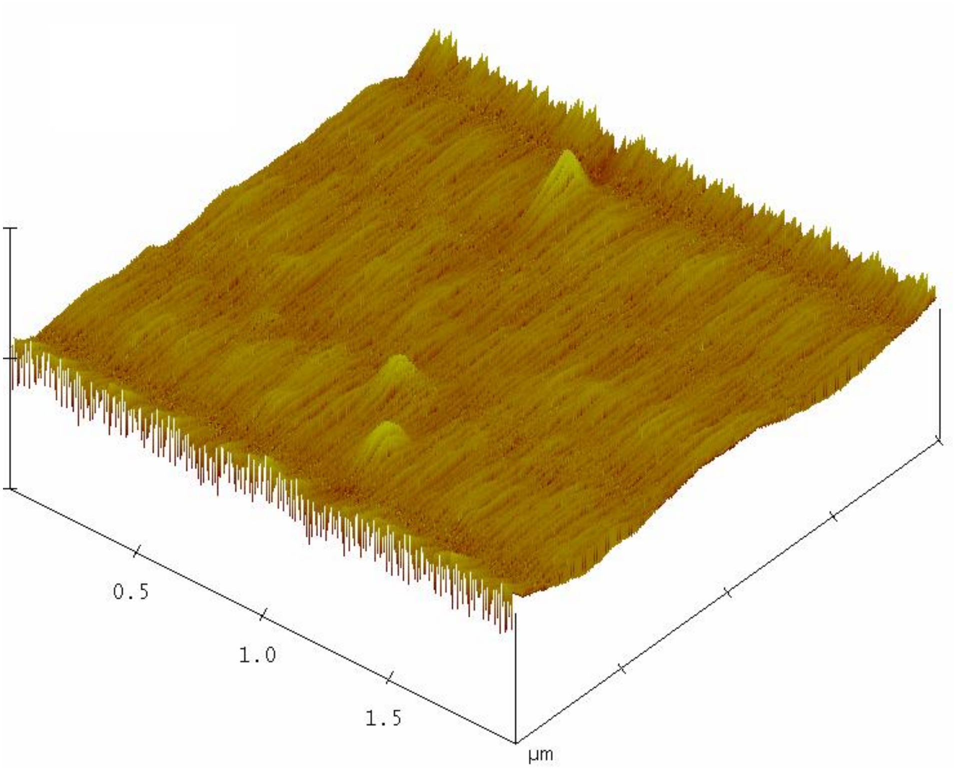

Figure 7.24 : The 2µmx2µm lateral AFM image of sample deposited at 15 Watt and 2.7 sccm argon flow rate.

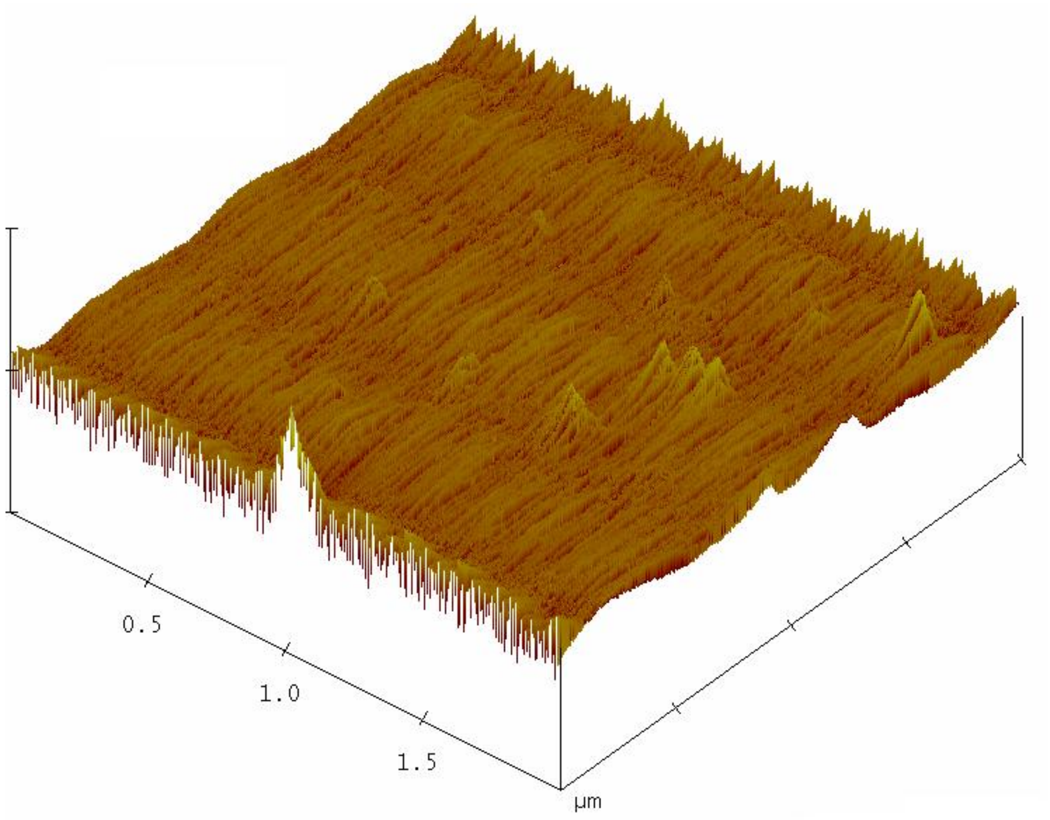

Figure 7.25 : The 2µmx2µm lateral AFM image of sample deposited at 150 Watt and 2.7 sccm argon flow rate.

7.3.2.2. Deposition by Substrate Target

The AFM images of samples deposited by substrate target are shown in Figure 7.26.

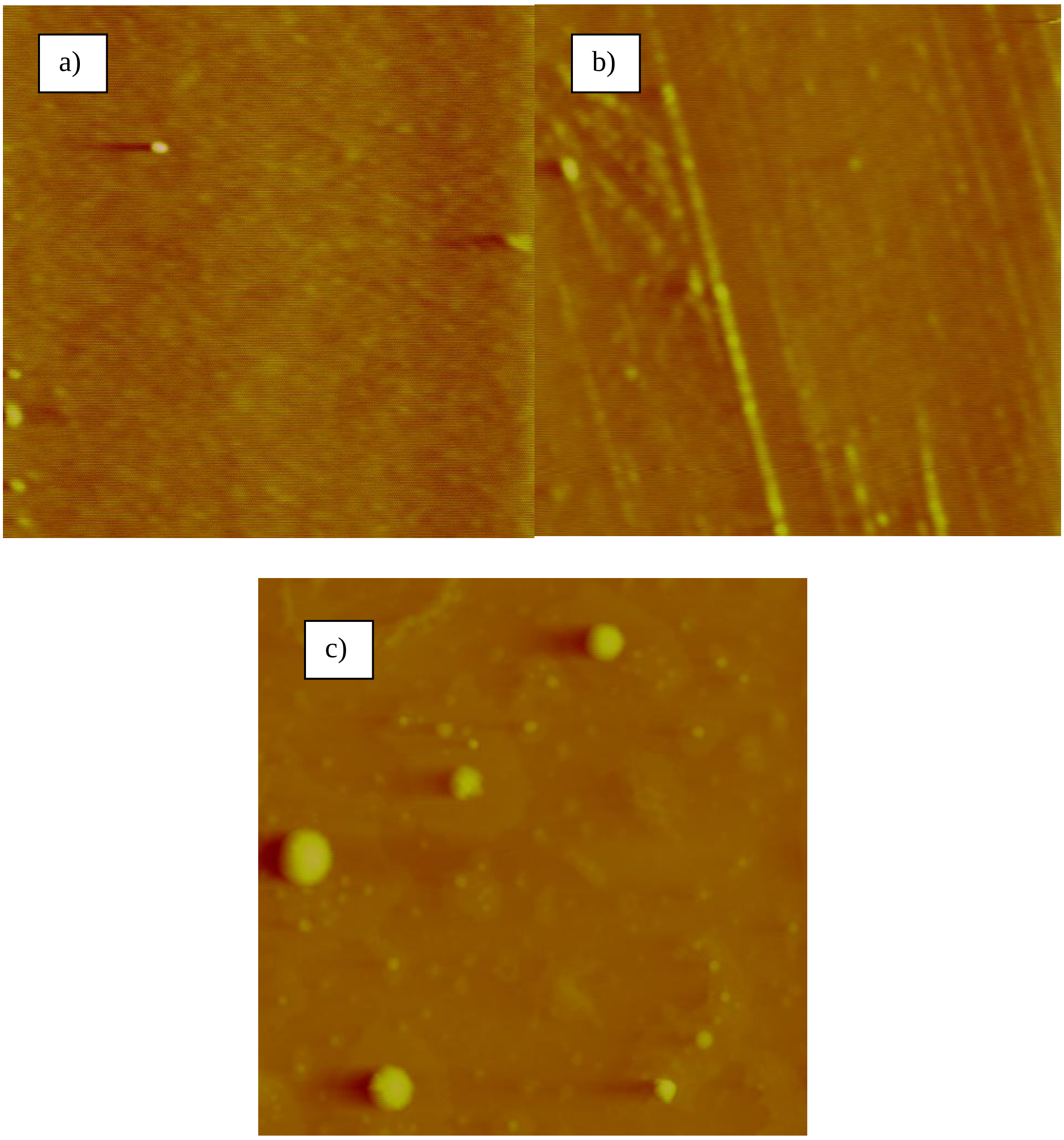

Figure 7.26 : The 5µmx5µm AFM image of sample deposited at a) 10 Watt and 2.7 argon flow rate b) 15 Watt and 2.7 sccm argon flow rate c) 150 Watt and 2.7 sccm argon flow rate.

It can be seen from this image that when power increases, roughness increases too. The rms values of 10 Watt, 15 Watt and 150 Watt are 0.250 nm, 0.345 nm and 3.057 nm, respectively.

If a comparison between powder target and substrate target is made, it can be said that deposition with powder target is faster than substrate target. It can be because powder target is not sintered. By this means, particles are broken easily and deposition rate increases.

The lateral images of this set are shown in Figure 7.27, Figure 7.28 and Figure 7.29.

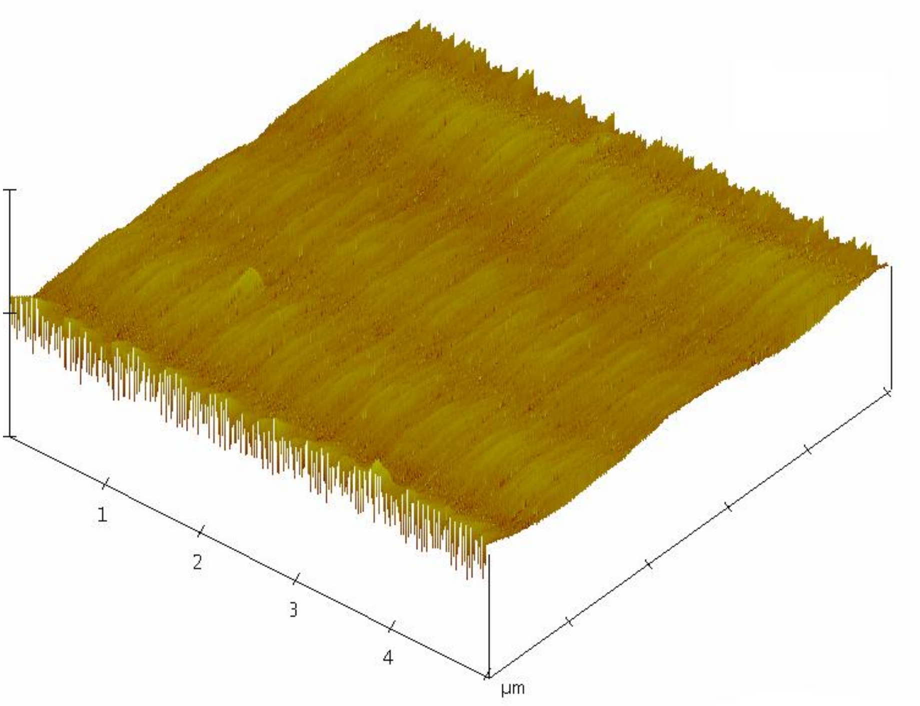

Figure 7.27 : The 5µmx5µm lateral AFM image of sample deposited at 10 Watt and 2.7 sccm argon flow rate.

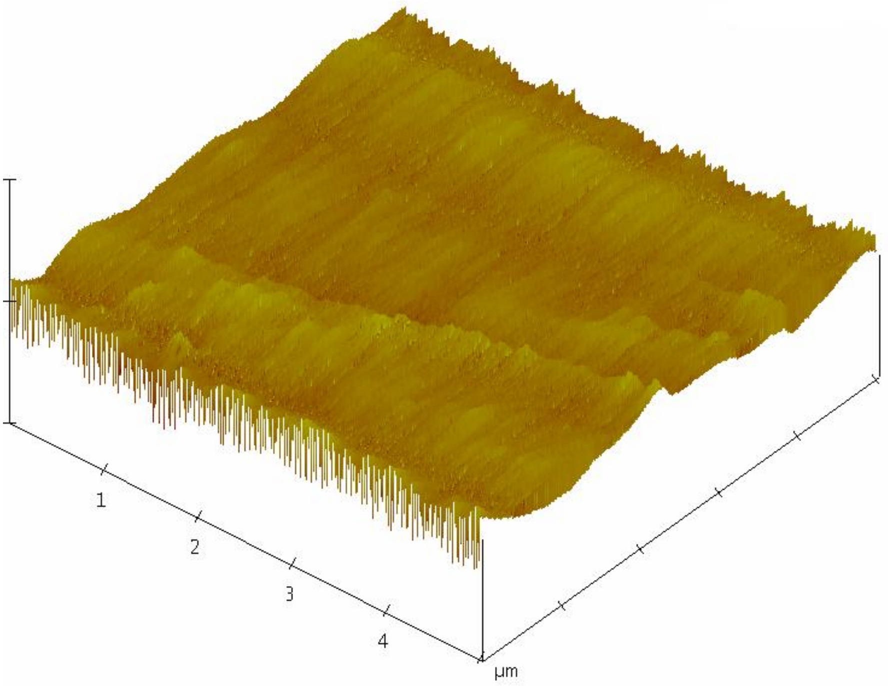

Figure 7.28 : The 5µmx5µm lateral AFM image of sample deposited at 15 Watt and 2.7 sccm argon flow rate.

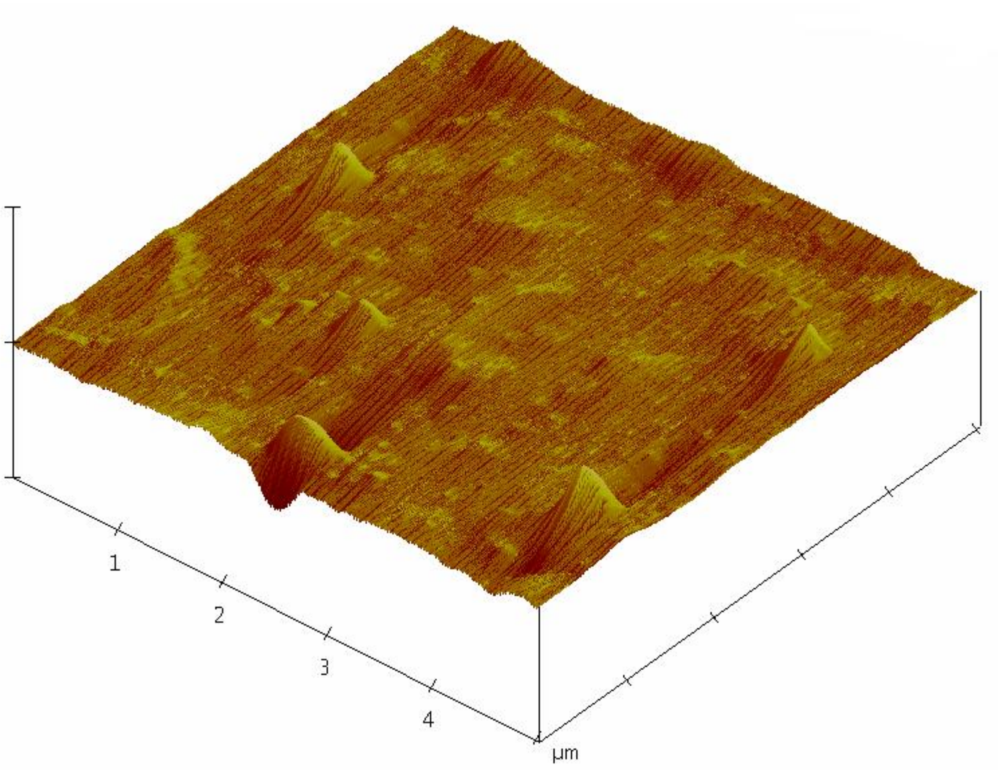

Figure 7.29 : The 5µmx5µm lateral AFM image of sample deposited at 150 Watt and 2.7 sccm argon flow rate.

7.3.3. The Annealed Samples

The AFM images of annealed samples are ahown in Figure 7.30.

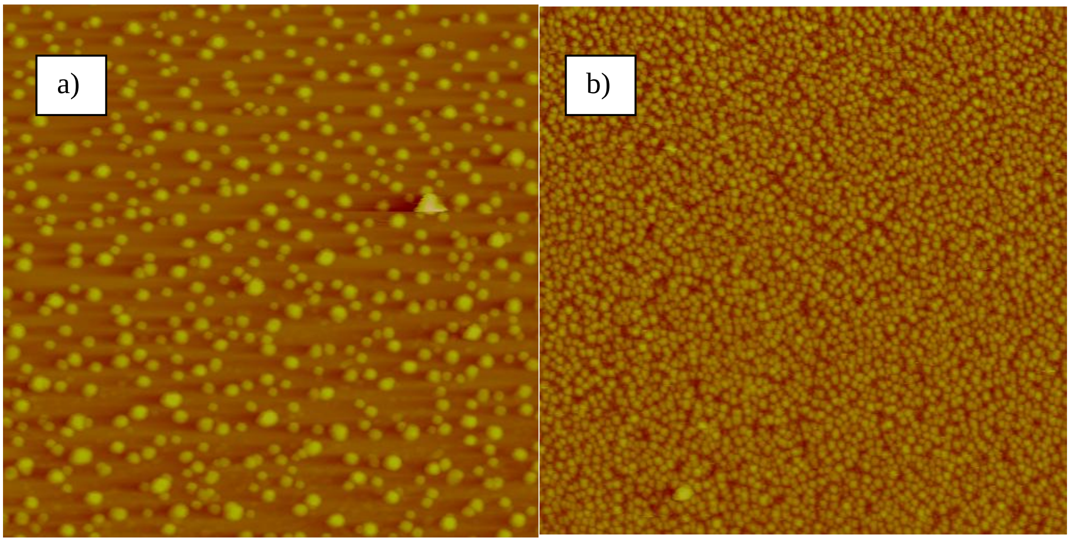

Figure 7.30 : The 10µmx10µm AFM image of sample deposited by a) substrate target b) powder target.

By looking Figure 7.30, it can be said that nanocrystalline silicon particles are obtained. The darker field in image is attributed to the amorphous silicon matrix, while the brighter spherical particles correspond to the crystalline silicon [30]. Spherical nanocrystalline particles were formed by the effect of increasing temperature. Rms roughness of samples is 13.540 nm for substrate target and 10.803 nm for powder target. In the light of these results, it can be said that rms roughness of sample deposited by substrate target is higher than that of powder target. On the other hand, it can be seen from figures that the number of particles formed by powder target is more than the number of particles formed by substrate target. If it is remembered that the AFM images of previous samples which were not annealed, the number of particles fell on samples deposited by powder target are higher than that of substrate target. This is because of particles which are easily broken from powder target. The reason of breaking easily is that powder target was not sintered. Even though at first sight the breakage of particles from target easily is a disadvantage because of increasing of dirtiness of thin films, it is turned to an advantage in annealing process.

The lateral images of annealed samples are shown in Figure 7.31 and Figure 7.32.

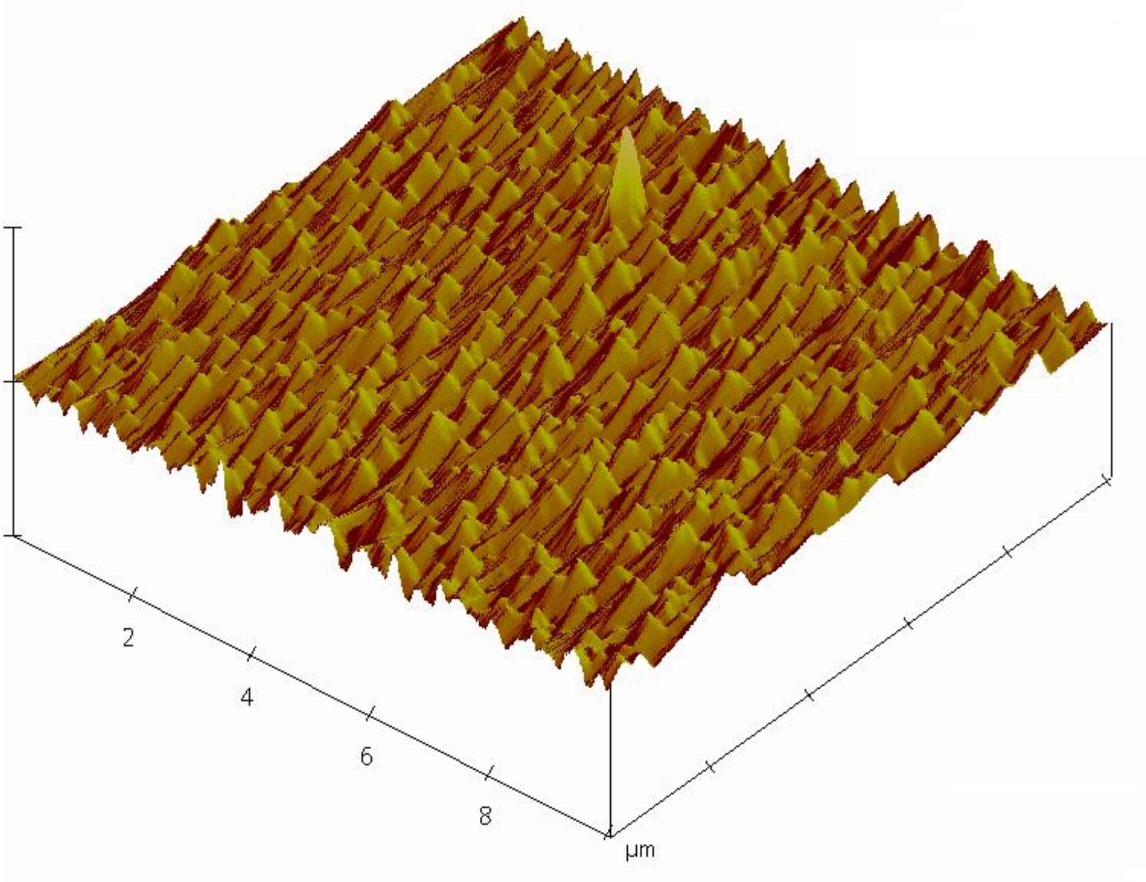

Figure 7.31 : The 10µmx10µm AFM image of sample deposited by substrate target.

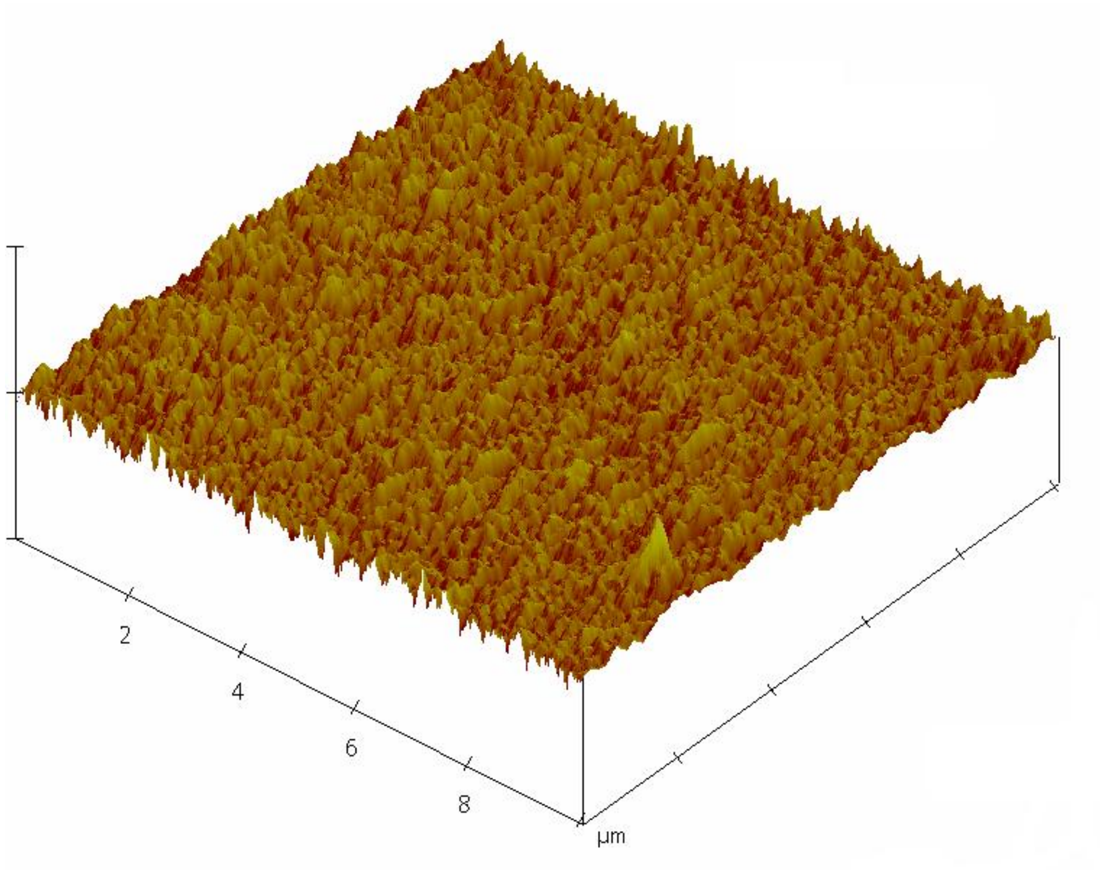

Figure 7.32 : The 10μmx10μm lateral AFM image of sample deposited by powder target.

7.4. X-Ray Diffraction (XRD)

X-Ray Diffraction was carried out on the samples which were deposited at 1 Watt, 4 Watt, 10 Watt and 15 Watt on native oxidized silicon substrate. Firstly, native oxidized single crystalline silicon substrate was characterized and then deposited samples were characterized. An additional deposition on glass with the same parameters was also done for confirmation of amorphism. According to the analysis, formation of amorphous silicon was confirmed. The XRD spectrum of native oxidized single crystalline silicon (111) substrate is shown in Figure 7.33.

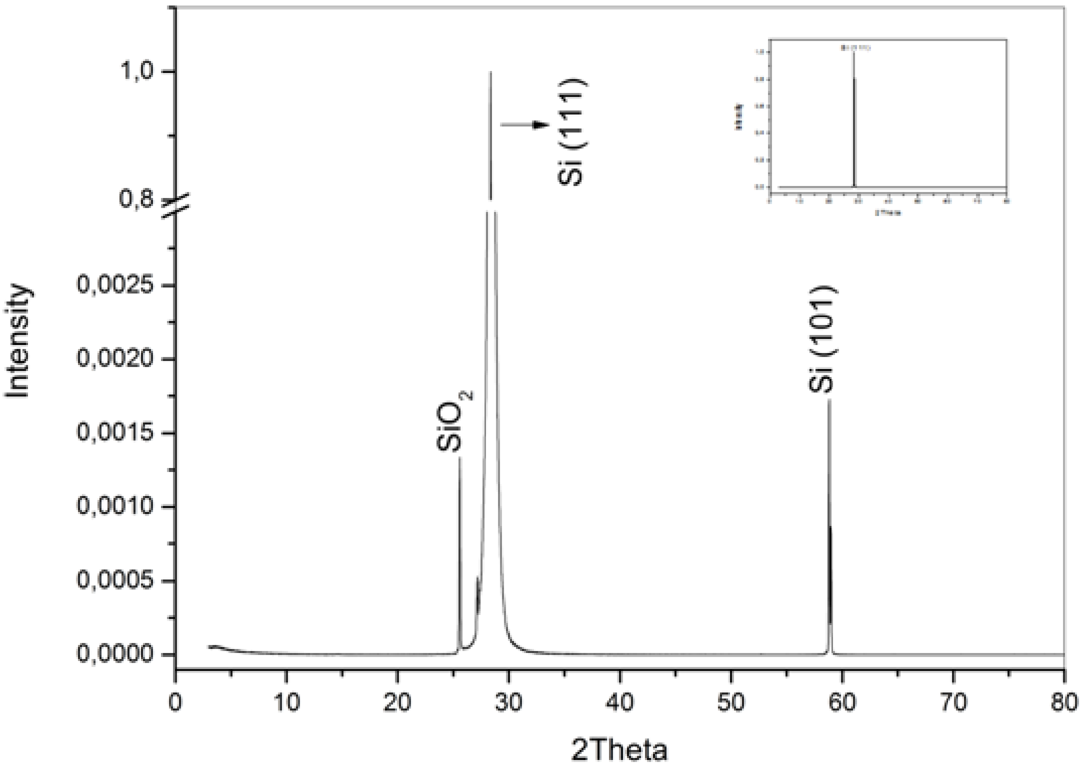

Figure 7.33 : The X-Ray Diffraction pattern of native oxidized silicon substrate.

As seen from Figure 7.33, native oxidized silicon substrate has a strong (111) orientation that it is the finger prints of silicon and it is observed at $2\vartheta\sim28^\circ$. In addition, it has silicon dioxide (SiO_2) peak that observed at $2\vartheta\sim25^\circ$. This is because silicon was not kept in a vacuumed environment. The other peak that observed in the spectrum is attributed to silicon (101) orientation and it exists at $2\vartheta\sim58.6^\circ$.Since all of the films were deposited with titanium, which had 150 Å thickness, before silicon deposition, a titanium deposited silicon substrate was also characterized by XRD. It is shown in Figure 7.34.

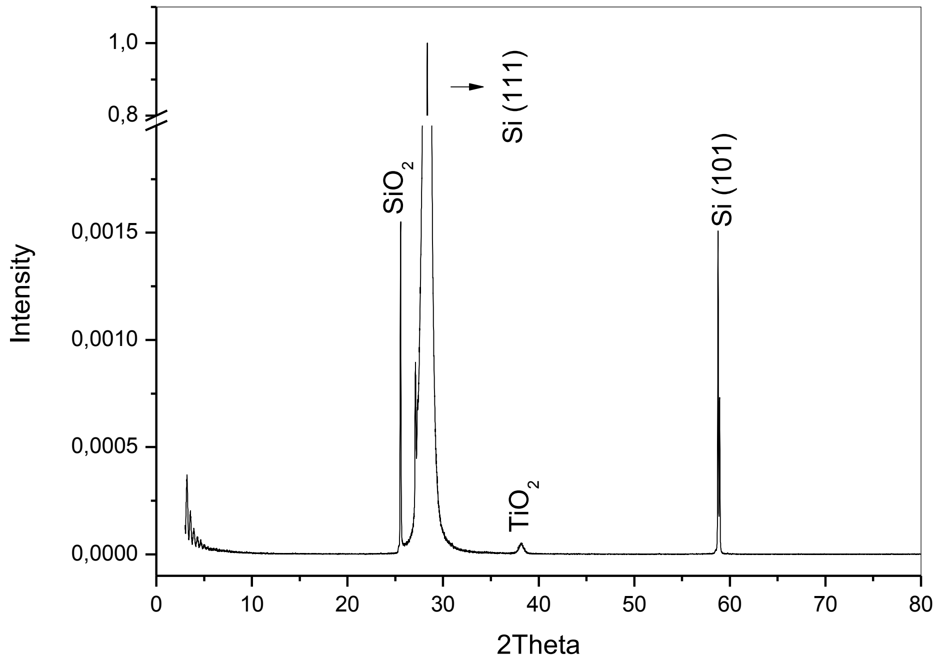

Figure 7.34 : The X-Ray Diffraction patterns of titanium deposited silicon substrate.

In Figure 7.34, there are the same peaks as seen from native oxidized silicon substrate except one peak which is resided at 2ϑ~38°. This peak belongs to anatase titanium dioxide.

7.4.1. Deposition of Thin Films by DC Power

7.4.1.1. Study of 1 Watt, 4 Watt, 10 Watt and 15 Watt

The samples were deposited in the same conditions except power value. They were deposited at 1 Watt, 4 Watt, 10 Watt and 15 Watt. The argon flow rate is 2.7 sccm for all samples. XRD patterns of these samples are shown in Figure 7.35, Figure 7.36, Figure 7.37 and Figure 7.38. The spectra that taken from all samples have the same peaks that attributed to silicon dioxide (2ϑ~14, 2ϑ~26°), silicon (111) (2ϑ~28°), titanium dioxide (2ϑ~38.5°) and silicon (101) (2ϑ~58.6°). The peak observed at 2ϑ~38.5° which is attributed to titanium dioxide formation is because of the depositon of titanium before silicon deposition. The reason of oxidation is due to tendency of titanium which is oxidized easily. On the other hand, it can be said that the deposited silicon thin films are amorphous, because it is not seen any peak that different from XRD peaks of single crystalline silicon substrate. In addition, this can be also understood from hump which is seen at low angles.

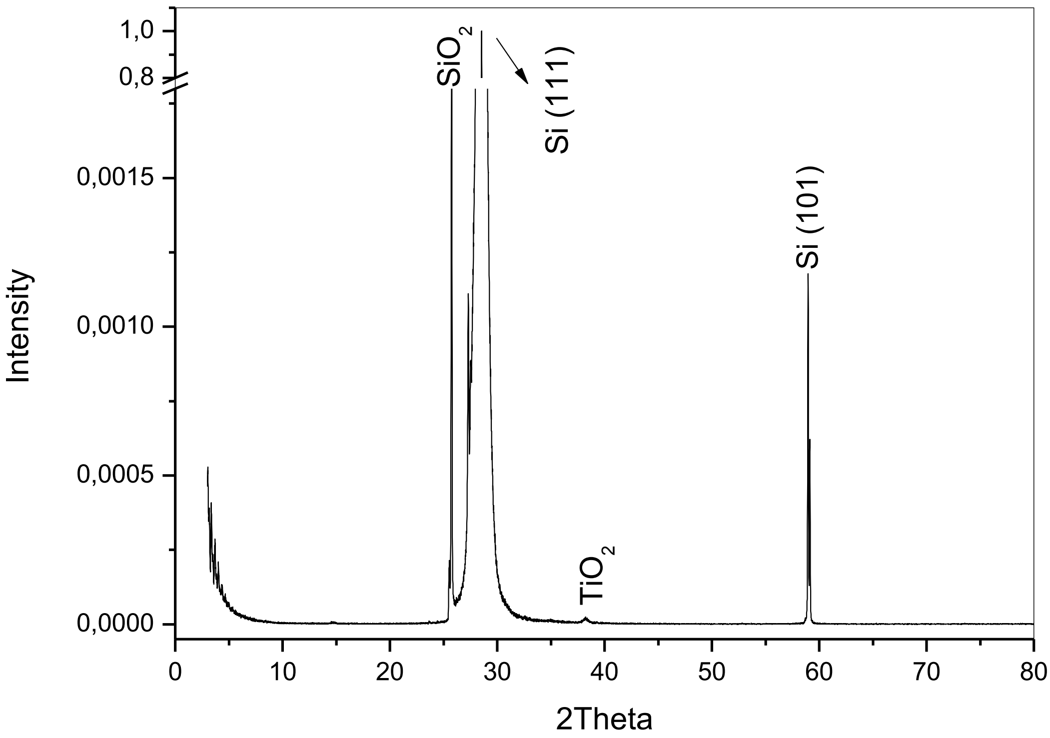

Figure 7.35 : The X-Ray diffraction patterns of silicon deposited substrate at 1 W.

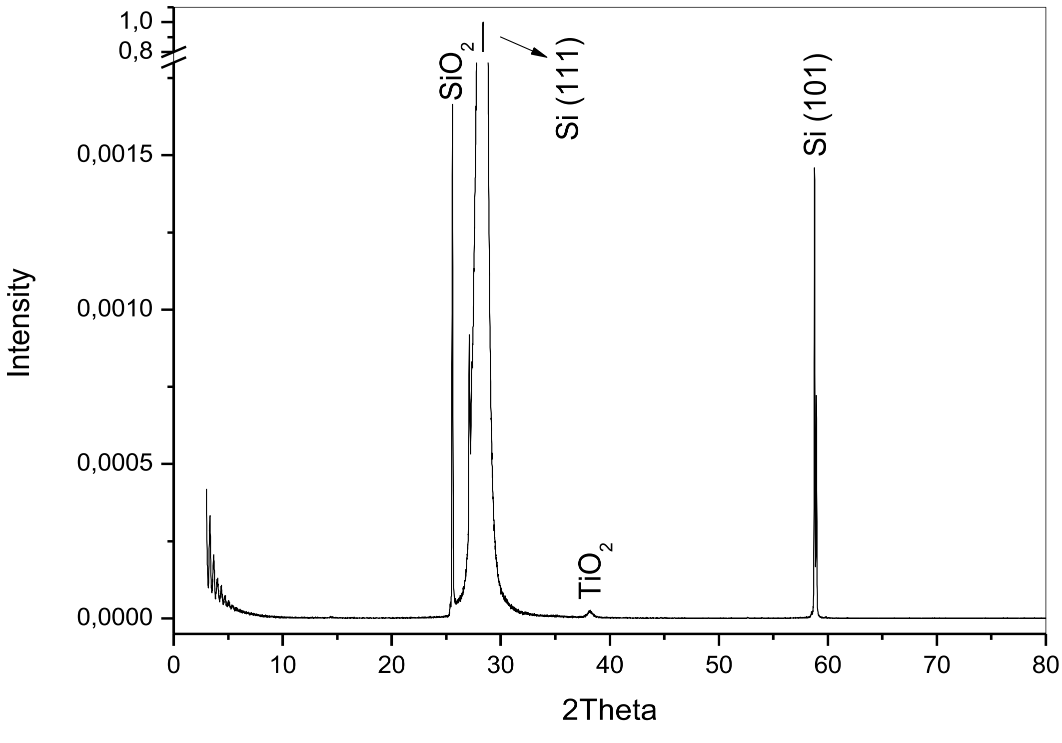

Figure 7.36 : The X-Ray diffraction pattern of silicon deposited substrate at 4 W.

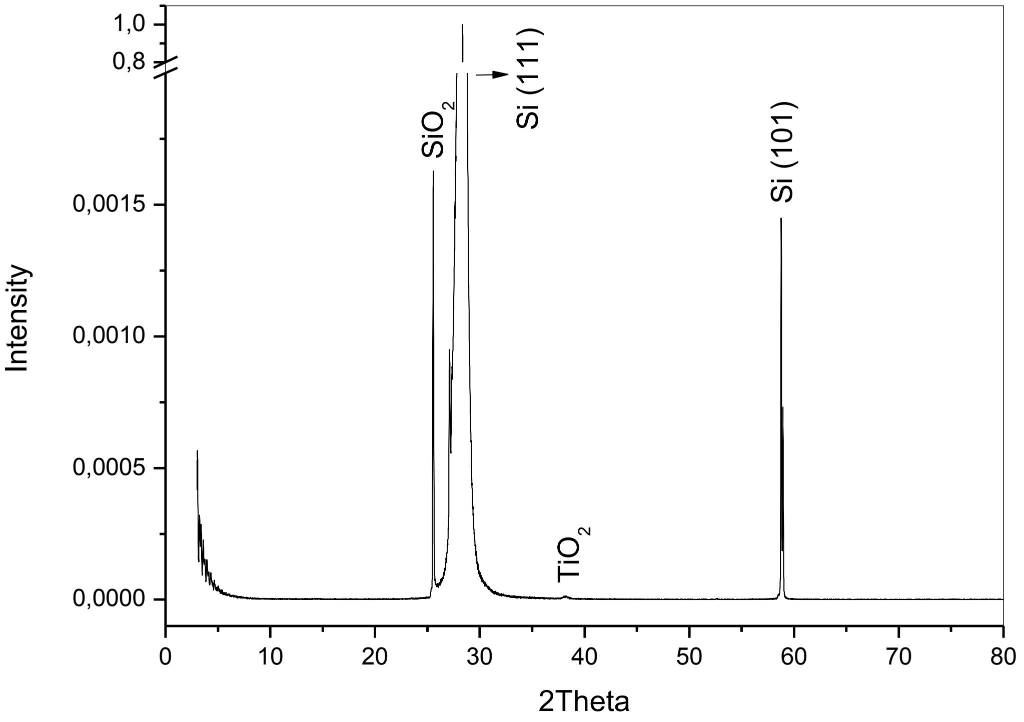

Figure 7.37 : The X-Ray Diffraction patterns of silicon deposited substrate at 10 W.

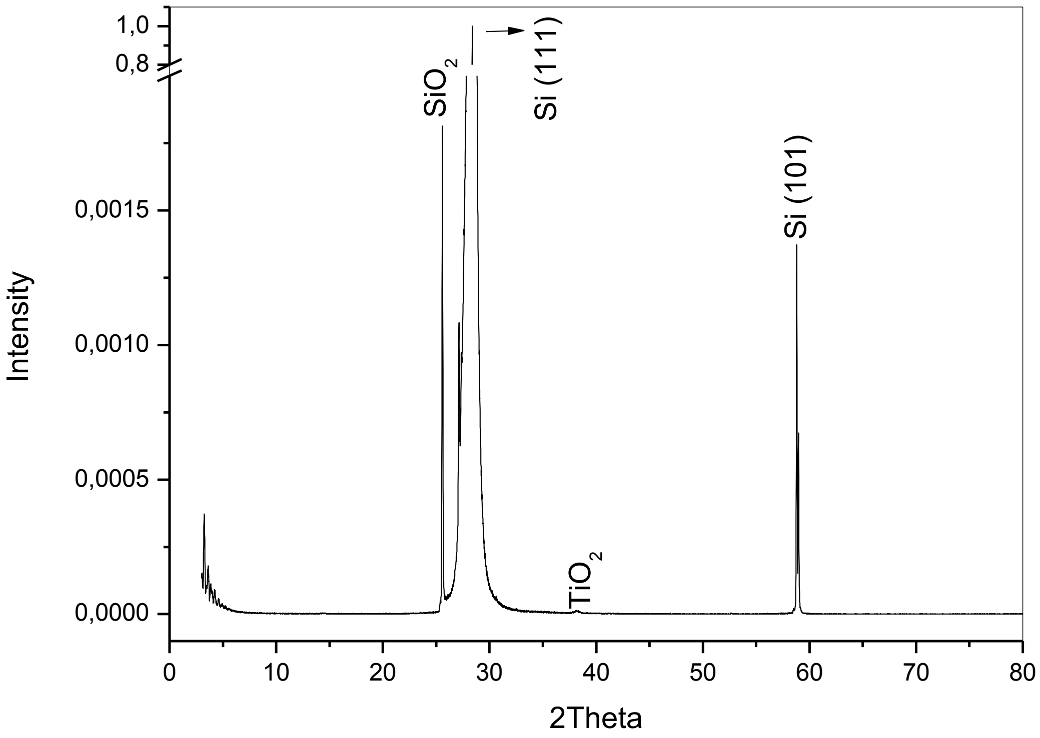

Figure 7.38 : The X-Ray diffraction pattern of silicon deposited substrate at 15 W.

As seen from all figures shown above, it can be said that SiO_2 decreases when power is increased. While the intensity of SiO_2 is 0.0023 for 1 Watt, the intensity of SiO_2 is 0.0017 for 15 Watt. On the other hand, the intensity of Si (101) increases when power increases. While the intensity of Si (101) is 0.0011 for 1 Watt, the intensity of Si (101) increases to 0.0015 for 15 Watt. The rise in intensity can be because of the increasing of roughness with increasing power. When roughness increases, scattering increases too and intensity rises. In addition, intensity of TiO_2 decreases with increasing of power.

The amorphousity can be also understood from the XRD pattern which belongs to silicon deposition of glass which is shown in Figure 7.39. There is not an apparent peak that belongs to any phase. So, it can be said that all the films are amorphous.

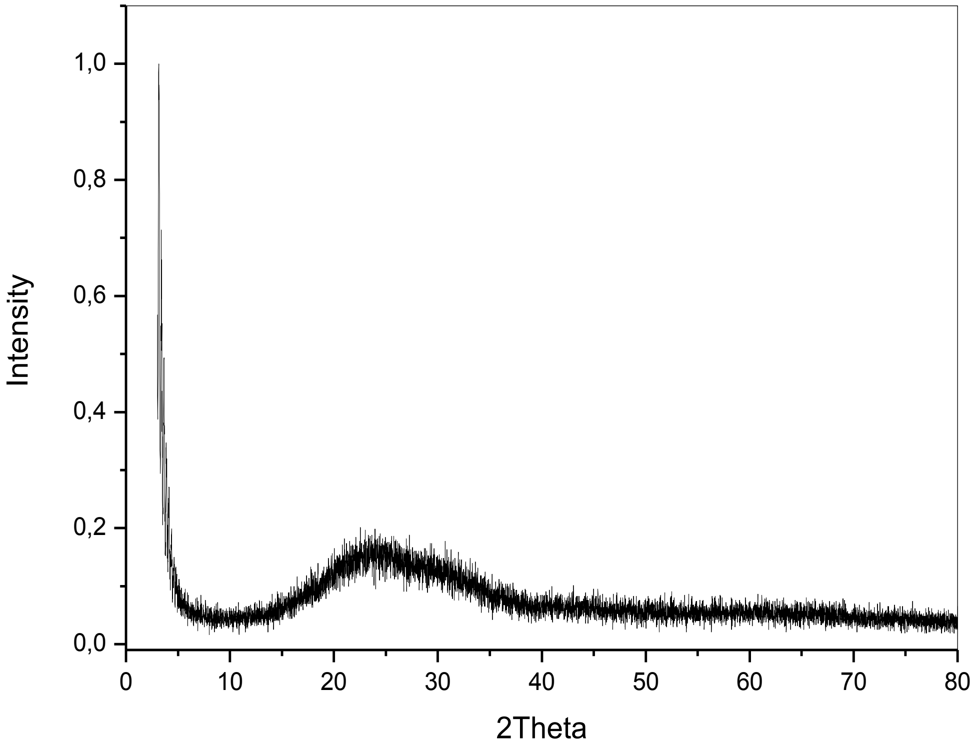

Figure 7.39 : The X-Ray diffraction pattern of silicon deposited glass substrate.

7.4.1.2. Study of The Lowest – The Highest Power and Argon Flow Rate

After 1 W, 4 W, 10 W and 15 W, in the light of result of previous study it was decided that samples were deposited at 1 and 15 W with the lowest and the highest argon flow rate for each power. The XRD patterns of this set are shown in Figure 7.40, Figure 7.41, Figure 7.42 and Figure 7.43.

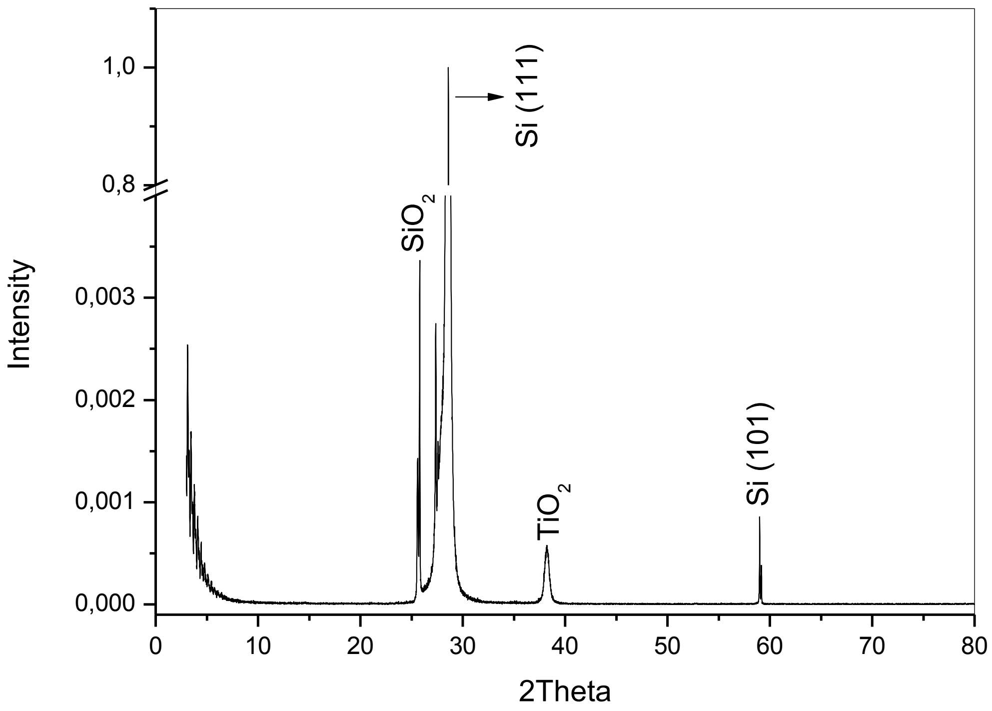

Figure 7.40 : The X-Ray diffraction pattern of silicon deposited sample at 1 Watt and 2 sccm argon flow rate.

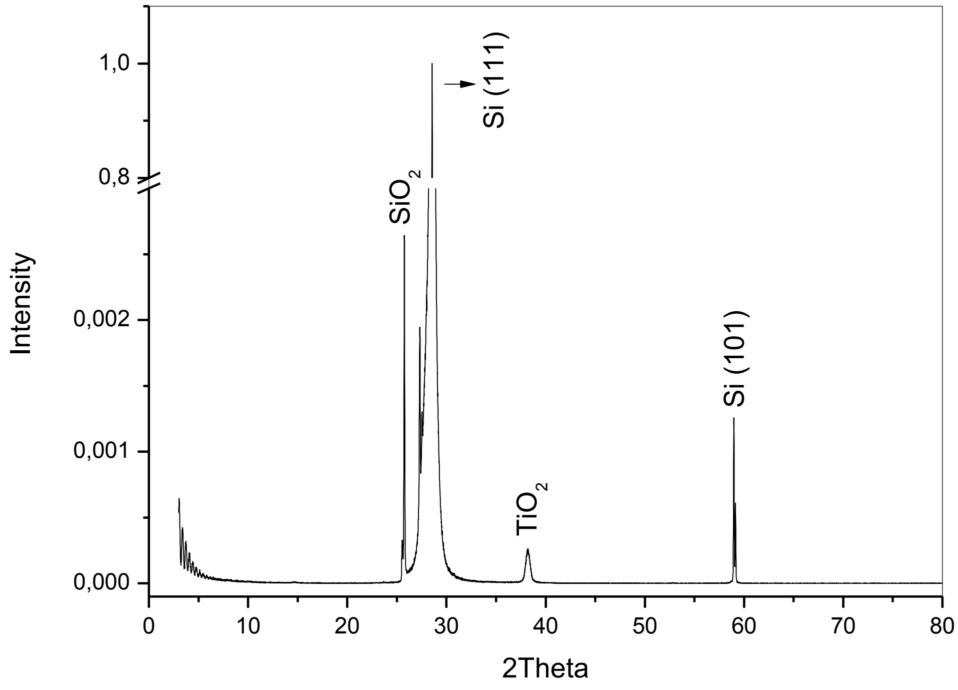

Figure 7.41 : The X-Ray diffraction pattern of silicon deposited sample at 1 Watt and 20 sccm argon flow rate.

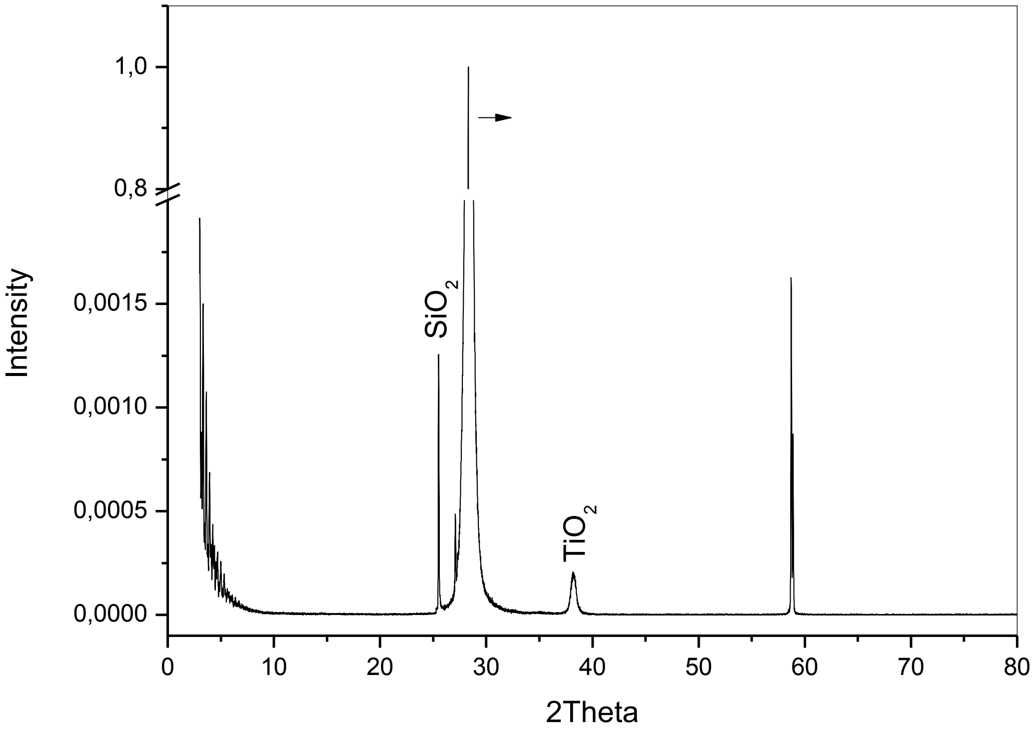

Figure 7.42 : The X-Ray diffraction pattern of silicon deposited sample at 15 Watt and 0.8 sccm argon flow rate.

It can be said for all films obtained from these studies that all films demonstrate the same peaks as obtained previous study. So it can be said that all films are amorphous.

For 1 Watt-2 sccm and 1 Watt-20 sccm argon flow rate, it can be said that the intensity of SiO_2 decreases with increasing argon flow rates. While the intensity of SiO_2 is 0.0033 for 2 sccm, the intensity decreases to 0.0026 for 20 sccm. On the other hand, intensity of Si (101) increases with increasing argon flow rate. Intensity of Si (101) is $8.6x10^{-4}$ for 2 sccm, but the intensity increases to $12x10^{-4}$ for 20 sccm. Intensity of TiO_2 decreases with increasing of argon flow rate.

For 15 Watt-0.8 sccm and 15 Watt-20 sccm argon flow rate, intensity of SiO_2 increases with argon flow rate. The intensity was 0.0012 for 0.8 sccm, but it increases to 0.0014 for 20 sccm. The intensity of Si (101) increases with increasing argon flow rate. The intensity is 0.0016 for 0.8 sccm, it increases to 0.0019 for 20 sccm. On the other hand, the intensity of TiO_2 also decreases with increasing argon flow rate.

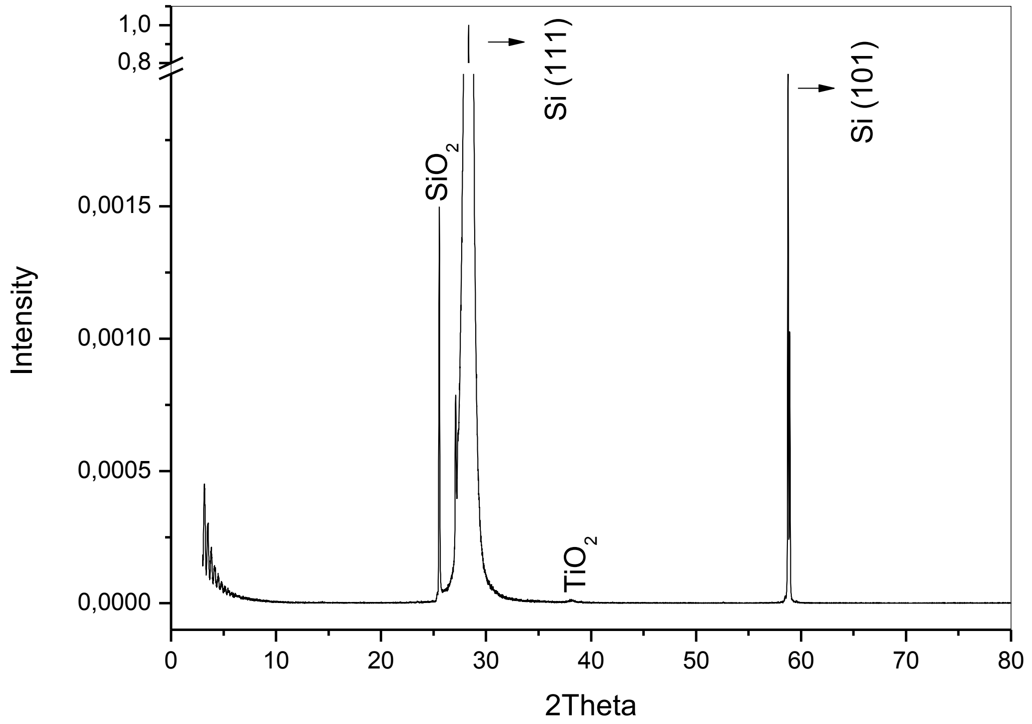

Figure 7.43 : The X-Ray diffraction patterns of silicon deposited sample at 15 Watt and 20 sccm argon flow rate.

7.4.2. Deposition of Thin Films by RF Power

7.4.2.1. Deposition by Powder Target

At first, powder target was used. Samples were deposited at 10 Watt, 15 Watt and 150 Watt with constant argon flow rate which is 2.7 sccm. XRD results are shown in Figure 7.44, Figure 7.45 and Figure 7.46.

It can be understood from figures, all the peaks obtained from this study is same as previous studies. Silicon dioxide (2ϑ~26°), silicon (111) (2ϑ~28°), titanium dioxide (2ϑ~38.5°) and silicon (101) (2ϑ~58.6°) can be seen from figures.

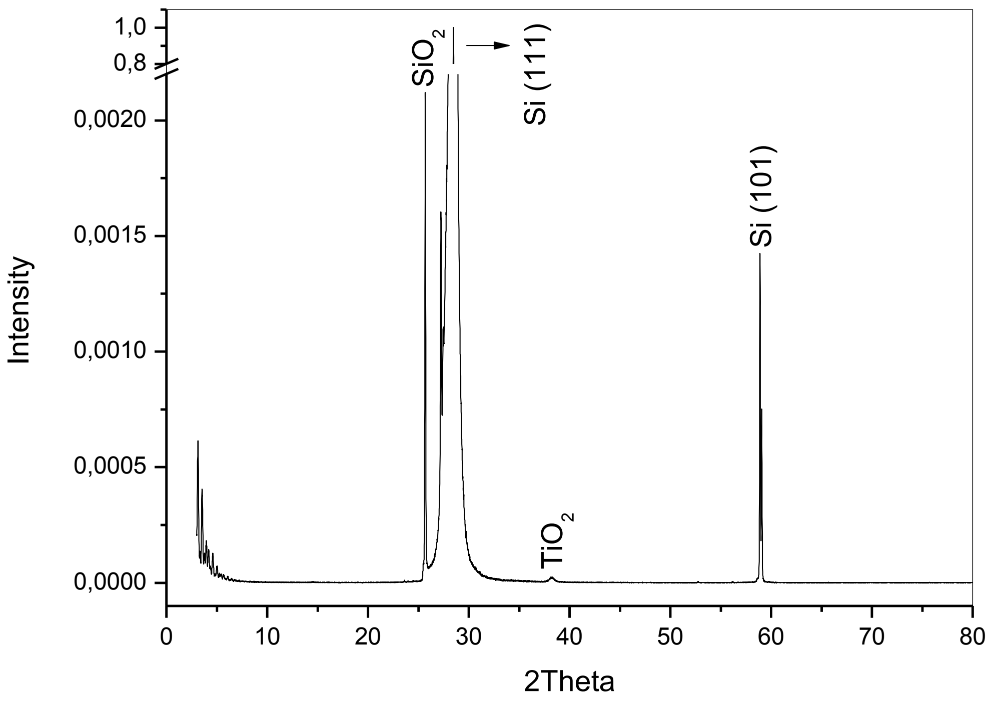

Figure 7.44 : The X-Ray diffraction pattern of silicon deposited sample at 10 Watt and 2.7 sccm argon flow rate.

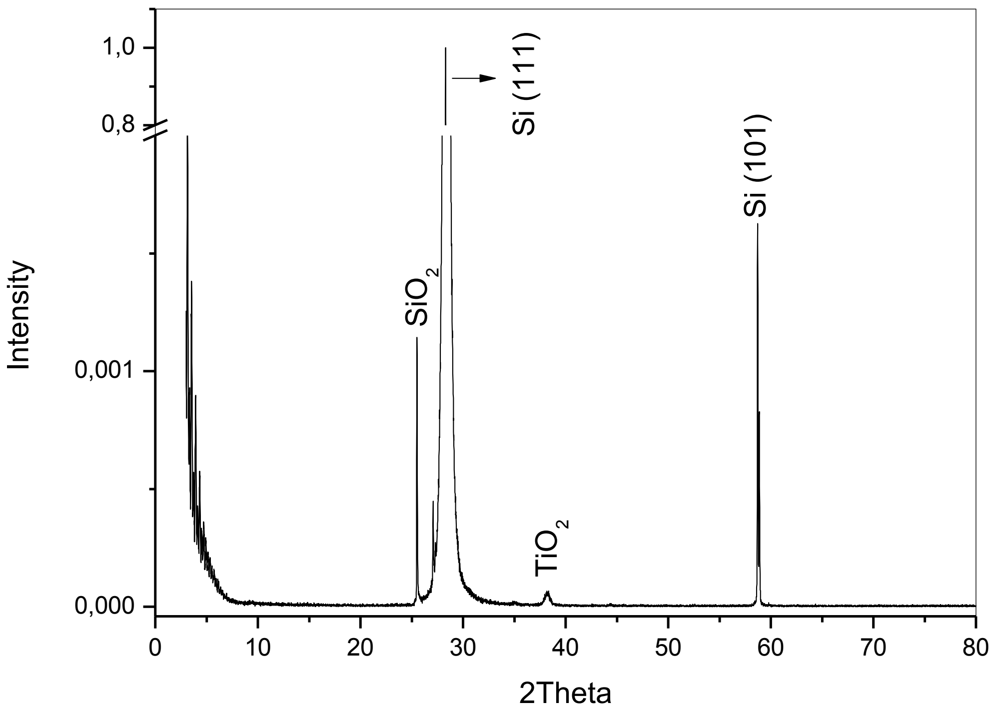

Figure 7.45 : X-Ray diffraction pattern of silicon deposited sample at 15 Watt and 2.7 sccm argon flow rate.

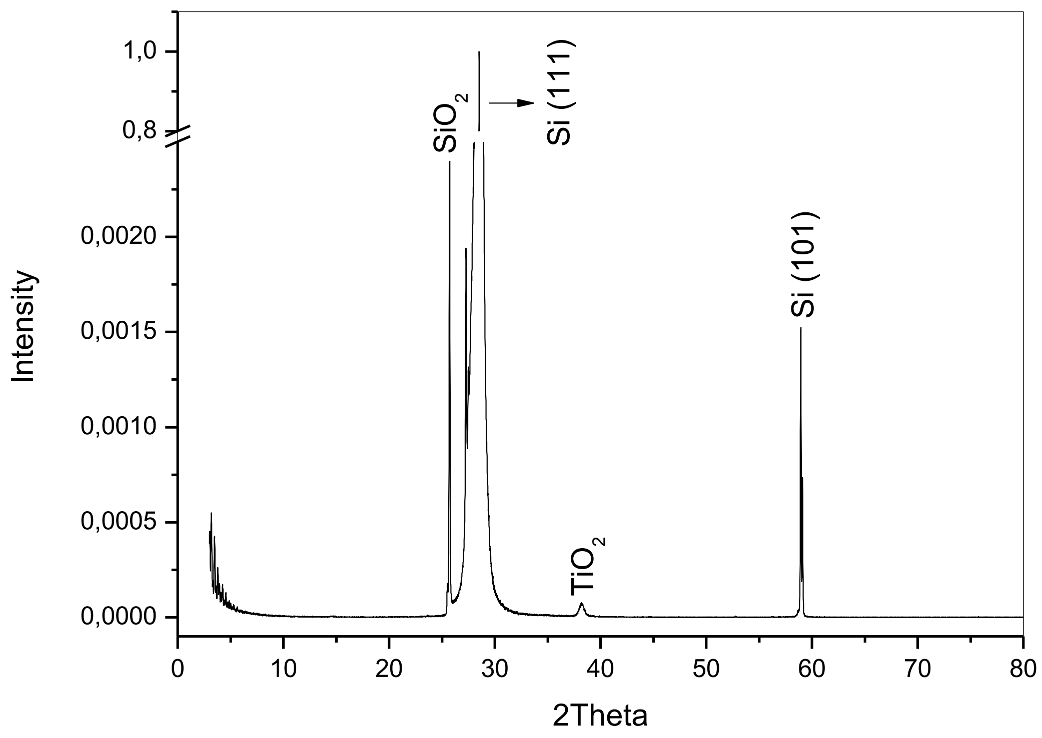

Figure 7.46 : X-Ray diffraction pattern of silicon deposited sample at 150 Watt and 2.7 sccm argon flow rate.

7.4.2.2. Deposition by Substrate Target

After deposition by powder target, deposition by substrate target was started. Samples were deposited at 10 Watt, 15 Watt and 150 Watt with constant argon flow rate which is 2.7 sccm. XRD results are shown in Figure 7.47, Figure 7.48 and Figure 7.49.

As seen from figures, everything is the same as previous results for deposition at 10 Watt and 15 Watt. But on the other hand, at 150 Watt Si (101) peak resided in $2\vartheta \sim 58^{o}$ is not seen. It can be because of the thin film thickness. Deposition rate is very high at 150 Watt and silicon could be deposited thicker than done in previous studies. It can be understood from intensity of SiO_2 which is at $2\vartheta \sim 25^{o}$. Intensity of SiO_2 decreased.

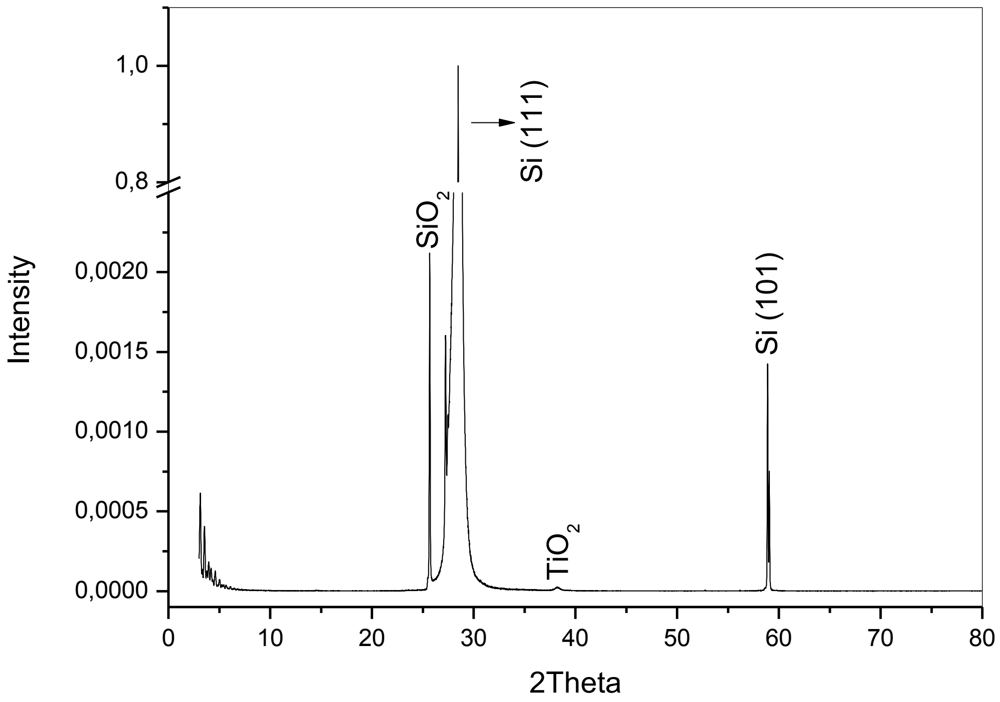

Figure 7.47 : The X-Ray diffraction pattern of silicon deposited sample at 10 Watt and 2.7 sccm argon flow rate.

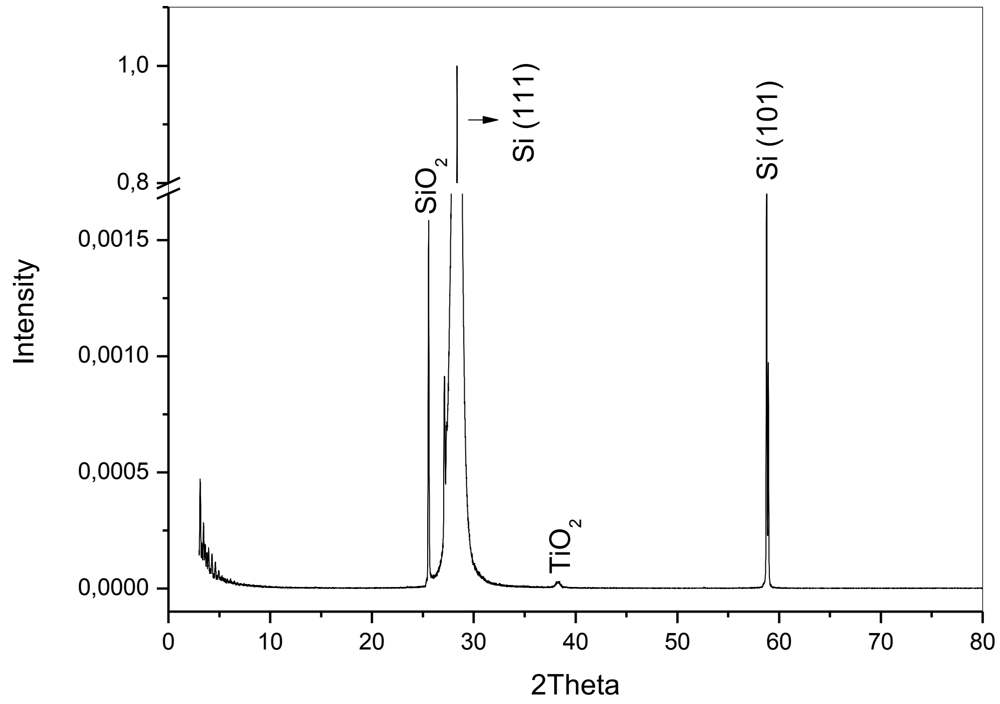

Figure 7.48 : The X-Ray diffraction pattern of silicon deposited sample at 15 Watt and 2.7 sccm argon flow rate.

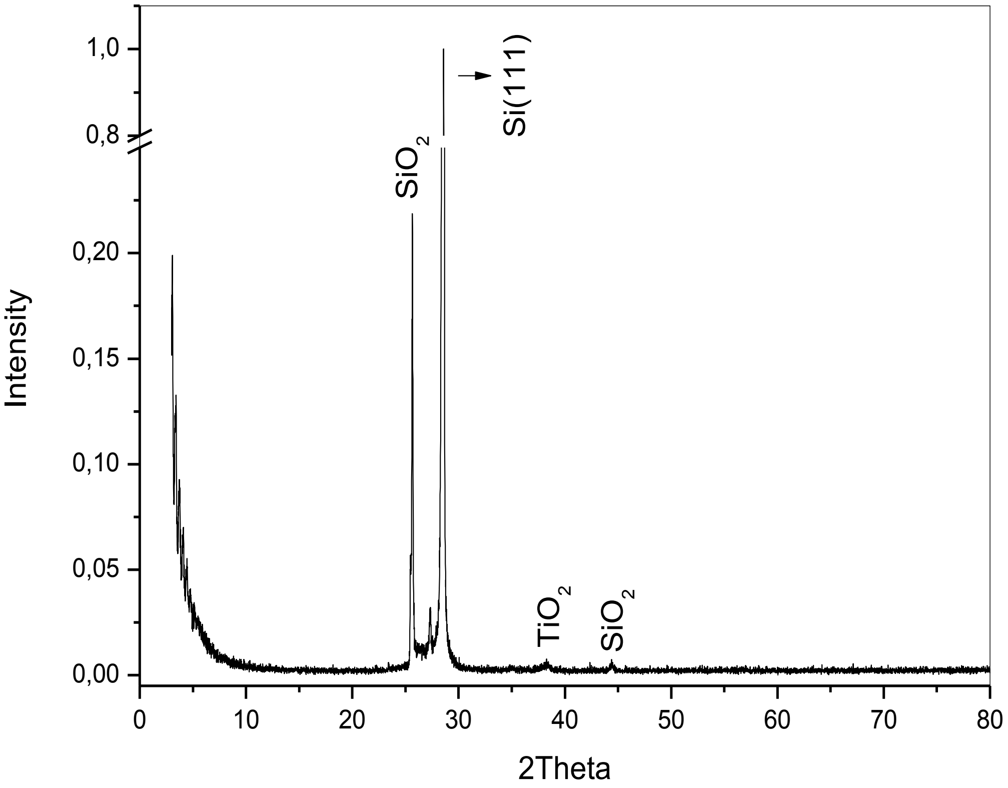

Figure 7.49 : The X-Ray diffraction pattern of silicon deposited sample at 150 Watt and 2.7 argon flow rate.

7.4.3. Annealed Samples

After amorphous silicon deposition was finished, annealing of deposited samples for nanocrystallization was started. Silicon deposition was done on native oxidized silicon substrate. XRD result is shown in Figure 7.50.

As seen from Figure 7.50, there are more peaks seen in annealed samples than not annealed samples. Addition to the peaks seen in not annealed samples, there are lots of additional peaks that observed. Silicon dioxide crystals are mostly formed. They are seen at 2ϑ~14°, 2ϑ~20°, 2ϑ~34°, 2ϑ~39°, 2ϑ~45°, 2ϑ~50°, 2ϑ~53° and 2ϑ~73°. On the other hand, there are several peaks that belong to silicon crystals. Si (100) is seen at 2ϑ~42° and Si (220) can be seen at 2ϑ~47°. So it can be said that nanocrystalline silicon particles are obtained.

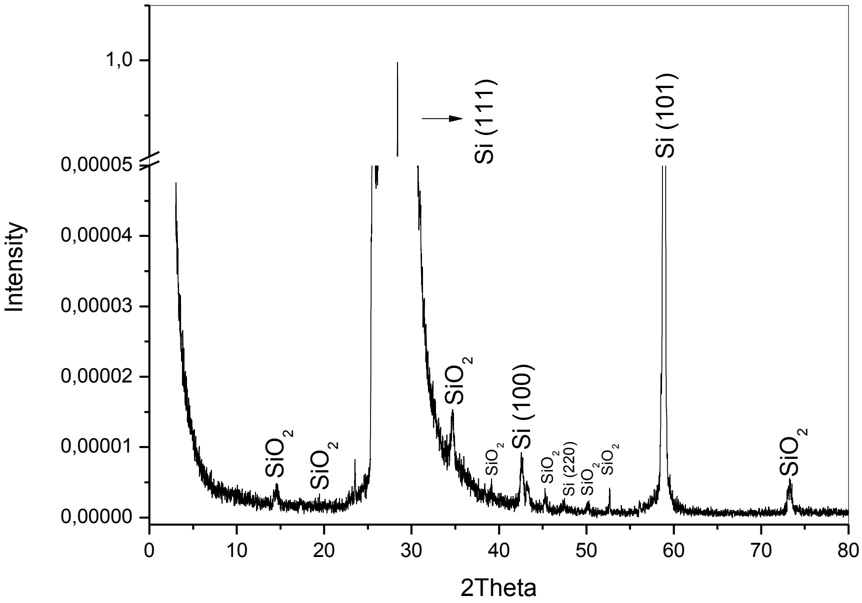

Figure 7.50 : X-Ray Diffraction patterns of sample deposited by powder silicon target and annealed at 800 °C for 1 hour.

7.5. Scanning Electron Microscopy (SEM)

For this system, two samples were chosen from each set and they were broken into two pieces by the help of a diamond pencil. Then, the broken pieces were located to a holder and images were taken from broken parts of the samples. The images can be seen from Figure 7.51 and Figure 7.52.

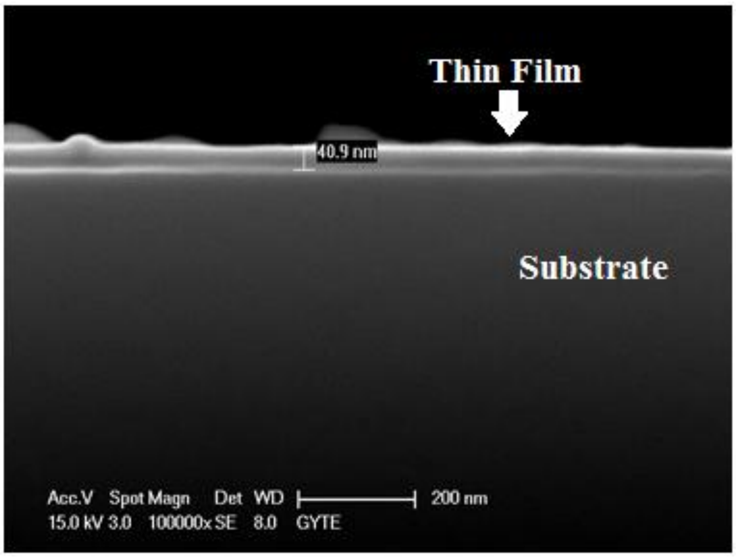

Figure 7.51 : The SEM image of sample which was deposited by DC power, 4 Watt-2.7 sccm.

As seen from Figure 7.51 and Figure 7.52 that deposition occured which is understood from color difference. The thickness of coating is 40.9 nm. In fact, the thickness of coating would have been 45 nm, because 15 nm titanium and 30 nm silicon were deposited on the samples. And for the sample is shown in Figure 7.52, the thickness of thin film is 43.7 nm which is close to desired thickness. It can be because of the uniformity of plasma in RF power, while in DC it is not .

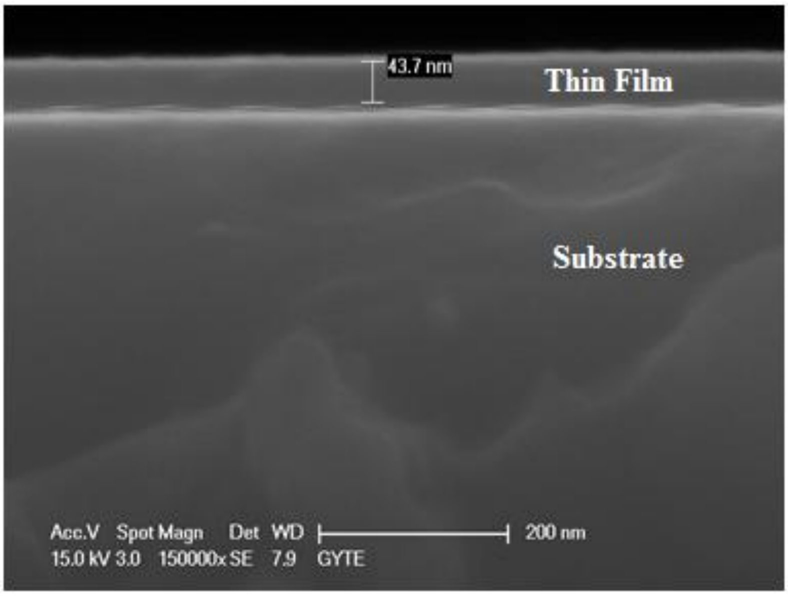

Figure 7.52 : The SEM image of sample which was deposited by RF power and powder target, 150 Watt-2.7 sccm.

8. DISCUSSION

In this study, the growth and characterization of nanocrystalline silicon thin films are concentrated. The main idea is to make feasibility of magnetron sputtering towards photovoltaic applications such as nc-Si:H single junction and multi-junctions with poly or single silicon photovoltaic cells. The hydrogenated nanocrystalline silicon (nc-Si:H) films are subjected only in solar cell applications, they also find wide applications in optoelectronic devices such as flat panel displays, image sensors and printer heads. However, as well known they have complex morphology consisting of a multilayered structure along the growth direction. In this structure, there are small crystalline in an a-Si:H matrix. Of course, this structure is strictly related to growth mechanism and techniques since during growth process, there is possibility to make disordered partial tissues and/or clustered between the different silicon phases instead of well defined and embedded crystallites particles called quantum dots in amorphous silicon environment. Other then techniques, the RF Magnetron Sputtering (RFMS) deposition technique has been used less to synthesis nc-Si:H, but it is proven as a well applicable technique for many industrial areas and as laboratory for basic science researches such as growth of magnetic thin films materials and catalysis surfaces successfully. In this study, the pure amorphous silicon films and amorphous silicon films having embedded crystallites were growth on quartz and naturally oxidized single crystal Si (111) substrates successfully by using Magnetron Sputtering. DC magnetron sputtering technique was also used to grow amorphous silicon films, but it was success limited unlike RF Magnetron Sputtering did. Especially, the power and argon plasma dilution effect distribution and size of crystallites. Less power introduces well defined small size “nanocrystal” in amorphous matrix. AFM pictures show silicon crystallites among amorphous environment with well size distributions. Also, Raman spectroscopy investigations prove the formation of only amorphous films and existence of silicon crystallites in amorphous films. By supporting literature support, the annealing temperature of 800 ^{o}C is successful to make distribution of nanocrystals in amorphous films from pure amorphous phase. Although XRD was used to investigate of nano crystallites formations, the number of crystallites formation was not enough for good investigations. Under these observations, RF Magnetron Sputtering technique is approved successes to synthesis nanocrystalline silicon with homogeneous thicknesses (30 nm) and with well size distributions of nanocrystals.

Near future, some electrical and photoconductivity properties will be investigated on these samples to complete these preliminary work. As it is mentioned before, nanocrystalline silicon thin films will be developed for photovoltaic application. The nanocrystal size and distribution effect directly electronic and optical properties since nanocrystals act like quantum dots (SQD). The morphology of SQD has tune-up effect on light absorption and emission. The introducing hydrogen with argon in the growth chamber will help to control size and distribution of nanocrystals; at the same time the optical and electronic structure will be tune-up. That’s why future work will be with pure argon gas diluted by certain amount hydrogen molecule to produce 30 nm of nc-Sí:H as intrinsic thin film layer towards photovoltaic applications.

9. CONCLUSIONS

In this study, amorphous silicon was deposited by DC and RF power supplies without using hydrogen and nanocrystalline silicon particles can be obtained by annealing samples at 800 ºC for 1 hour. Characterizations were done for every sample. In the light of characterization results, these conclusions are found.

- Magnetron Sputtering can be used for depositing amorphous silicon thin films as well as Plasma Enhanced Chemical Vapor Deposition (PECVD).
- RF power is more suitable for depositing amorphous silicon, because film deposited from RF is more homogeneous and cleaner than deposited by DC power.
- Films deposited by substrate target are cleaner than deposited by powder target. So it can be said that substrate target is more suitable. In addition, the crystalline formation of thin films deposited by substrate target is higher than powder target as it is understood from Raman Spectroscopy analysis.
- When power increases, deposition rate increases, too. But if deposition is slower, quality of thin film becomes much better.
- Increasing of argon flow rate causes increasing of deposition rate.

REFERENCES

[1] Nominanda H., Kuo Y., 2003. Process and Material Properties of PECVD Boron-Doped Amorphous Silicon Film, Applied Physics Letters, 60 p.

[2] Erkovan M., 2010. Ultra İnce Geçiş Metal Filmlerin (PtCo, Py/Cr) Kristalografik Yapıları ve Magnetik Özelliklerinin Belirlenmesi, Gebze Institute of Technology, Graduate School of Science Engineering and Technology, Kocaeli, Turkey.

[3] Palz W., 2011. Photovoltaics: State of the Technology, 2012, *Solar Today*, Vol. 25, p18.

[4] Şişman A., 2012. Istanbul Technical University, Lecture Notes of "Photovoltaic Power Systems".

[5] Akkaya A., 2005. Amorf Silikon Güneş Pillerinde Fototaşıyıcı Rekombinasyon Kinetiği, Master's Thesis, Mersin University Graduate School of Science Engineering and Technology, Mersin.

[6] Zhao W., Deng J., Yang B., Yu Z., Aceves M., Nanocrystalline silicon quantum dots Thin Films Prepared by Magnetron Reaction Sputtering, *Proc. of SPIE*, Vol. 7381 738113-8.

[7] Amrani R., Benlekehal D., Baghdad R., Senouci D., Zeinert A., Zellama K., Chahed L., Sib J.D., Bouizem Y., 2008. Low-temperature growth of nanocrystalline silicon films prepared by Rf magnetron sputtering: Structural and optical studies, *Journal of Non-Crystalline Solids*, 354 (2008) 2291-2295.

[8] Sharma S.N., Debabrata D., Banerjee R., 1997. A simple modification of the magnetron sputtering method for the deposition of boron-doped hydrogenated microcrystalline silicon films with enhanced doping efficiency, *Thin Solid Films*, 298 (1997) 200-210.

[9] Zacharias M., Tsybeskov L., Hirschman K.D., Fauchet P.M., Blasing J., Kohlert P., Veit P., 1998. Nanocrystalline Silicon superlattices: Fabrication and characterization, *Journal of Non-Crystalline Solids,* Volume 227-230 Part 2 (1998) 1132-1136.

[10] Baghdad R., Benlakehal D., Portier X., Zellama K., Charvet S., Sib J.D., Clin M., Chahed L., 2008. Deposition of nanocrystalline Silicon thin films: Effect of total pressure and substrate temperature, *Thin Solid Films*, 516 (2008) 3965-3970.

[11] Bouizem Y., Abbes C., Sib J.D., Benlakehal D., Baghdad R., Chahed L., Zellama K., Charvet S., Ellipsometric and raman spectroscopic study of nanocrystalline silicon thin films prepared by rf magnetron sputtering, *J. Phys.: Condens. Matter*, 20 445221.

[12] **Bouizem Y., Kefif K., Sib J.D., Benlakehal D., Kebab A., Belfedal A., Chaded L.,** 2012. Optical and structural properties of hydrogenated silicon films prepared by Rf-Magnetron sputtering at low temperatures: study ad function of argon gas dilution, *Journal of Non-Crystalline Solids*, 358 (2012) 854-859.

[13] **Tabata A., Nakano J., Mazaki K., Fukaya K.,** 2010. Film thickness dependence of structural and electrical properties of boron-doped hydrogenated microcrystalline silicon prepared by rf-magnetron sputtering, *Journal of Non-Crystalline Solids*, 356 (2010) 1131-1134.

[14] **Gonçalves C., Charvet S., Zeinert A., Clin M., Zellama K.,** 2002. Nanocrystalline Silicon thin films prepared by radiofrequency magnetron sputtering, Thin Solid Films, 403-404 (2002) 91-96.

[15] **Gonçalves C., Zeinert A., Charvet S., Lejeune M., Grosman A., von Bardeleben H.-J., Zellama K.,** 2004. Impurities and related microstructure in nanocrystalline silicon films grown by radiofrequency Magnetron Sputtering, *Thin Solid Films*, 451-452 (2004) 370-374.

[16] **Shuaib A., Levallois C., Gatuhier J.P., Paranthoen C., Durand O., Cornet C., Chevalier N., Le Corre A.,** 2011. Sputtered hydrogenated amorphous silicon thin films for distributed Bragg reflector and long wavelength vertical cavity surface emitting lasers applications, Thin Solid Films, Volume 519, Issue 18 (2011) 6178-6182.

[17] **Paul S., Dutta P., Galipeau D., Bommitsetty V.,** 2009. Microstructure and charge transport in hydrogenated nanocrystalline silicon: Effect of post deposition hydrogen plasma treatment, *Photovoltaic Specialists Conference (PVSC)*, 978-1-4244-2950-9.

[18] **Kim W., Lee J., Ko E.-K., Lyou J.H.,** 2004. Structural changes in nanocrystalline silicon deposited by rf-magnetron sputtering, *Applied Physics A*, 79, 1813-1817 (2004).

[19] **Thaiyalnayaki V., Cerqueira M.F., Ferreira J.A., Tovar J.,** 2008. The influence of electric field on te microstructure of nc-Si:H Films produced by Rf-Magnetron Sputtering, *Vacuum*, 82 (2008) 1433-1436.

[20] **Callister W.D.,** 2001. Fundamentals of Material Science and Engineering, John Wiley & Sons, Fifth Edition.

[21] **Dutta J., Hoffman H.,** 2011. Nanomaterials.

[22] **Umut E.,** 2006. Modulated Photoconductivity Measurements on the Hydrogenated Amorphous Silicon Samples, Master's Thesis, Hacettepe University Graduate School of Science Engineering and Technology, Ankara.

[23] **Kolodziej A.,** 2004. Staebler-Wronski effect in amorphous silicon and its alloys, Opto-Electronics Review, 12(1), 21–32 (2004).

[24] **Solomon A.,** 2012. Growth and Characterization of Thin Film Nanocrystalline Silicon Materials and Solar Cells, Doctoral Thesis, Delpft University of Technology.

[25] Guha S., 2004. Thin film silicon solar cells grown near the edge of amorphous to microcrystalline transition, *Solar Energy*, 77, 887 (2004).

[26] Vetterl O., Finger F., Carius R., Hapke P., Houben L., Kluth O., Lambertz A., Mück A., Rech B. and Wagner H., 2000. Solar Energy Materials and Solar Cells 62, 97 (2000).

[27] Behrisch R., 1981. Sputtering by Particle Bombardment:. Springer, Berlin.

[28] Trani F., 2004. Electronic and Optical Properties of Silicon Nanocrystals: a Tight Binding Study, *Physical Review*, 120 p.

[29] Wank M.A., 2011. Manipulating the Hydrogenated Amorphous Silicon Growing Surface, Chalmers University of Technology, Frankfurt, Germany.

[30] Zhao Z.X., Cui R.Q., Meng F.Y., Zhao B.C., Yu H.C., Zhou Z.B., 2004. Nanocrystalline silicon thin films prepared by RF sputtering at low temperature and heterojunction solar cell, *Materials Letters*, 58 (2004) 3963-3966.

[31] Nesheva D., Nedev N., Curiel M., Bineva I., Valdez B., Manolov E., Silicon Oxide Films Containing Amorphous or Crystalline Silicon Nanodots for Device Applications., Quantum Dots – A Variety of New Applications.

[32] Iqbal Z., Veprek S., 1982. Raman scattering from hydrogenated microcrystalline and amorphous silicon, *J. Phys. C*, 15 (1982), p. 377.

[33] Saha S.C., Ray S., 1995. Development of highly conductive n-type μc-Si:H films at low power for device applications, *J. Appl. Phys.*, 78 (1995), p. 5713.

[34] Ivanda M., Clasen R., Hornfeck M. and Kiefer W., 2003. Waveguide Raman spectroscopy: a non-destructive tool for the characterization of amorphous thin films, *J. Non-Cryst. Solids*, 322 46.

[35] Borowicz P., Latek M., Rzodkiewicz W., Laszcz A., Czerwinski A., Ratajczak J., 2012. Deep-ultraviolet Raman investigation of silicon oxide: thin film on silicon substrate versus bulk substrate, *Adv. Nat. Sci.: Nanosci. Nanotechnol.*, 3 (2012) 045003 (7pp).

[36] http://www.guneshaber.net/haber, Kristal Silisyum Solar Hücreleri.

[37] http://electronics.ege.edu.tr/boztepe/download/ees487lecture4.pdf, Boztepe M., 2009. Ege University, Lecture Notes of “Renewable Energy Sources”.

[38] http://www.eere.energy.gov/basics/renewable_energy/types_silicon.html, U.S. Department of Energy, Energy Efficiency & Renewable Energy.

[39] http://www.nrel.gov/ncpv/

[40] http://zebu.uoregon.edu/~imamura/122/lecture-2/em.html, Electromagnetic Spectrum.

[41] https://web.engr.oregonstate.edu/~yokochia/wiki/uploads/Documents/, CdTe.pdf, Oregon State University**.**

[42] http://www.solarcigsenergy.com/

CURRICULUM VITAE

Name Surname: Elif Ceylan Cengiz

Place and Date of Birth: Fatih / Istanbul, 16.07.1986

Marital Status: Married

Address: Karliktepe District, Soganlik Road, Helenium Sun Building Complex, A-1, Flat: 31, Kartal / Istanbul.

E-Mail: eckinaci86@gmail.com

High School: Besiktas Ataturk Anatolian High School

B.Sc.: Gebze Institute of Technology – Material Science and Engineering

M.Sc. : Istanbul Technical University – Nanoscience and Nanoengineering

Professional Experience and Rewards:

TUBITAK – Intern (for 1 month, 2008)

TPAO – Intern (for 1 month 2009)

Gebze Institute of Technology – Material Science and Engineering (February 2012–continue)